CIRCUMSTELLAR ENVIRONMENTS AROUND THE YOUNGEST PROTOSTARS: INTERFEROMETRIC OBSERVATIONS AND MODELING

BY

HSIN-FANG CHIANG

DISSERTATION

Submitted in partial fulfillment of the requirements
for the degree of Doctor of Philosophy in Astronomy
in the Graduate College of the
University of Illinois at Urbana-Champaign, 2011

Urbana, Illinois

Doctoral Committee:

Associate Professor Leslie W. Looney, Chair, Director of Research
Associate Professor Athol J. Kemball
Professor Charles F. Gammie
Professor Telemachos Ch. Mouschovias

Abstract

This thesis presents observations and modeling of nearby embedded sources in the earliest stage of protostellar evolution, i.e., Class 0 young stellar objects, using interferometric data of the Berkeley-Illinois-Maryland Association array and the Combined Array for Research in Millimeter-wave Astronomy. Protostars form through gravitational collapse inside their natal envelopes, and these circumstellar envelopes contain valuable information about the physical processes of star formation. In this thesis, both molecular lines and dust continuum are utilized to investigate the nature of the collapsing envelopes. In particular, I focus on the isolated edge-on low-mass protostar L1157. While a large-scale ($\sim$20,000 AU) flattened envelope is detected in both the N_2H^+ line and the 8 μm extinction perpendicular to the outflow orientation, the dust continuum shows spherical structures at scales between $\sim 10^2$ and $\sim 10^3$ AU. The N_2H^+ observations not only reveal the outer envelope that is too dim to be detected in dust continuum, but they also unveil the kinematic structures of the flattened envelope. The dust continuum is compared with theoretical collapse models using radiative transfer calculation and Bayesian inference. The modeling techniques, as well as the associated uncertainties, are detailed. The results show that a power-law envelope model with a density index $p \sim 2$ provides a better fit to the observations than the simple Shu model or the commonly-used Terebey-Shu-Cassen model. Furthermore, I discuss the implications of the modeling results on the dust grain properties and the constraints they place on the youngest circumstellar disk embedded inside the envelope.

In memory of my brother

Acknowledgments

Table of Contents

List of Tables

List of Figures

List of Abbreviations

AIC	Akaike Information Criterion
ALMA	Atacama Large Millimeter/Submillimeter Array
BIC	Bayesian Information Criterion
BIMA	Berkeley-Illinois-Maryland Association
CARMA	Combined Array for Research in Millimeter-wave Astronomy
EVLA	Expanded Very Large Array
FHSC	First Hydrostatic Core
IRAM	Institut de Radio Astronomie Millimétrique
MCMC	Markov Chain Monte Carlo
MIRIAD	Multichannel Image Reconstruction, Image Analysis and Display
OVRO	Owens Valley Radio Observatory
SED	Spectral Energy Distribution
SMA	Submillimeter Array
SZA	Sunyaev-Zel'dovich Array
VeLLO	Very Low Luminosity Object
VLA	Very Large Array
WMAP	Wilkinson Microwave Anisotropy Probe
YSO	Young Stellar Object

Chapter 1

Introduction

1.1 A Brief Review of Low-mass Star Formation

Significant progress has been made towards understanding of star formation in the past few decades, and a standard evolutionary scenario for isolated low-mass star formation has been constructed (e.g., see the reviews of Evans, 1999). Dense cores in molecular clouds collapse as gravity dominates over all resisting forces such as thermal pressure, magnetic fields, and turbulence, resulting in the birth of protostars. Protostars are initially surrounded by their natal envelopes while the material in the envelopes continues the gravitational collapse. Angular momentum in the collapsing envelope causes a disk to build up, and most of the material in the envelope falls onto the disk before it gets accreted into the central protostar. Also, jets and outflows are driven in the bipolar region. The envelope dissipates as mass is transported down through the circumstellar disk onto the protostar, or is carried away with the outflow. The system, usually referred as a young stellar object (YSO), is then dominated by the circumstellar disk, which may evolve into a planetary system like our Solar System (Figure 1.1).

Observational quantities, particularly the spectral energy distributions (SEDs), are used to classify YSOs. The most well known classification scheme is that of Lada & Wilking (1984) and Lada (1987), which is based on the infrared spectral index α between 2 and 25 μm: $0 < \alpha \lesssim 0.3$ for Class I, $-2 \lesssim \alpha \leq 0$ for Class II, and $-3 < \alpha \lesssim -2$ for Class III. This classification scheme also represents a temporal sequence and corresponds to the physical evolutionary stages (e.g., Robitaille et al., 2006). Class I sources are obscured by their

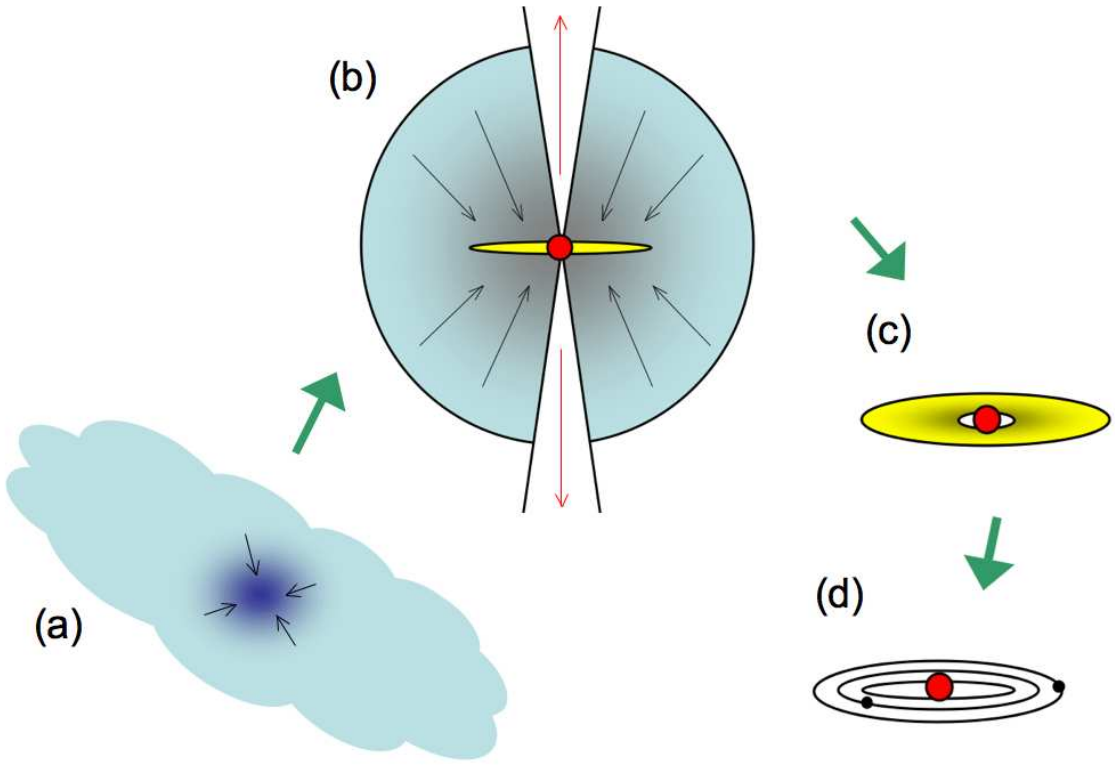

Figure 1.1 A schematic picture illustrating the process of star formation. (a) Gravity overcomes thermal, magnetic, and turbulent pressure in condensations of molecular cloud, forming a protostar. (b) In the early stage, the protostar-disk system is deeply embedded inside its natal envelope, which is undergoing gravitational collapse and forming the earliest circumstellar disk. Bipolar outflow, driven by the protostar-disk system, can take away excess angular momentum. (c) Material in the envelope eventually falls onto the optically thick disk. Disk structures such as gaps appear due to formation of giant proto-planets. (d) As the gas dissipates, a planetary system is formed around the pre-main-sequence star.

surrounding envelopes, and the emission from the dusty envelope causes the SED to rise toward long wavelength. The envelope has dissipated for Class II sources and the SED slope flattens out, but substantial infrared emission is seen from an optically thick circumstellar disk. Class III sources, surrounded by thin disks, show little or no infrared excess and the slope of their SEDs is similar to that of main sequence stars (e.g., α = -3 in the Reyleigh-Jeans limit). Besides α, other observational quantities such as bolometric temperature and luminosity have also been employed in the YSO classification. Consistent evolutionary ages are usually obtained for a variety of evolutionary models (e.g., Chen et al. 1995; Myers et al. 1998; also see more discussions in Evans et al. 2009).

An even younger class, the so-called Class 0 YSOs, was first introduced by Andre et al. (1993) and later better defined in Andre et al. (2000). Class 0 sources enclose internal heating protostars and they are centrally peaked in submillimeter continuum. They also have a higher ratio of submillimeter to bolometric luminosity ($L_{smm}/L_{bol} > 0.005$, where L_{smm} is measured longward of 350 μm) compared to the Class I sources. A YSO transitions from Class 0 to Class I when the mass of the protostar is equal to the mass of the remaining envelope. As the protostar evolves, the system mass is gradually transferred from the envelope to the disk, and finally, to the protostar.

Class 0 YSOs are in their main phase of mass accretion, and are characterized by their dense dusty envelopes. They are nearly invisible at wavelengths shorter than 10 μm due to large extinction by the material in the infalling envelope. The envelope undergoes gravitational collapse until most of the mass is accreted onto the central star-disk system. The mass accretion is likely to occur episodically rather than as a steady process. For example, the calculations by Tassis & Mouschovias (2005a,b) suggest that the mass is accreted through a series of magnetically controlled bursts in the inner envelope. Material may also pile up in the circumstellar disk and accrete in the fashion of outbursts, causing rapid increases of luminosity, which have been observed in the FU Orionis objects (e.g., Vorobyov & Basu, 2005b; Zhu et al., 2009; Reipurth & Aspin, 2010).

Disks are expected to form early on in the protostellar evolution, presumably in the Class 0 stage. While the properties of the early disks remain unknown, planet formation has likely started in these young circumstellar disks. Two major mechanisms have been proposed to describe the planet formation process: disk instability and core accretion. A massive disk would support the first scenario, as it aids the gravitational instability; a tenuous disk favors the second scenario. In the core accretion theory of planet formation, the predecessors of planets form by dust coagulation in the young disk-envelope environment, growing from sub-micron size dust to km-size planetesimals. Dust grains have been observed to be mm-size in many T Tauri disks (e.g., Beckwith & Sargent, 1991, source age $\sim 10^5$-10^6 yrs); however, the dust properties in the earliest circumstellar disks (age $\sim 10^4$-10^5 yrs) are not well constrained. The main difficulty is that Class 0 protostars are surrounded by dusty envelopes which obscure light from the embedded disk and prohibit direct detection. Moreover, as the envelope properties are poorly known, disentangling flux from the envelope and disk components relies on model assumptions, which confuses the data interpretation. Reliable detection of the embedded circumstellar disks requires a good knowledge of the envelopes, especially the inner envelope structure at the scale of $\sim$100AU.

Interferometric observations of Class 0 objects provide the best means to peer inside the bright envelope and potentially reveal the embedded young, compact circumstellar disks. In particular, an interferometer spatially filters emission and measures the structures at multiple scales, allowing comparison of models and data at high resolutions. Dust continuum observations of young protostars are commonly used for probing envelope structures, and it is only dependent on dust opacity, density, and temperature structures. On the other hand, molecular lines are excellent tracers, as different species and transitions probe environments of specific conditions. Molecular line observations reveal kinematic information in envelopes and are essential for identifying Keplerian rotation in disks. However, complex chemistry coexisting with active accretion and outflow processes can make interpretations difficult. To really understand Class 0 YSOs, both dust continuum and molecular emission should be

considered.

The goal of this thesis is to investigate properties of Class 0 YSOs using interferometric data. I aim to understand the early star formation process and how observations and theories align with each other. Both archived and new data from Berkeley Illinois Maryland Association (BIMA) and Combined Array for Research in Millimeter-wave Astronomy (CARMA) are employed. In particular, thermal dust continuum is used to model the envelope structure, and molecular line emission is examined to reveal the envelope kinematics. A modeling procedure combined with radiative transfer calculations is constructed for comparing interferometric data with theoretical models.

1.2 Theoretical Models of Gravitational Collapse

Gravitational collapse has been studied extensively and theoretical models are proposed to describe the circumstellar envelope structures and the effects of physical conditions on the infall process. The simpler collapse models consider self-similar isothermal solutions, which are a continuum of solutions (e.g., Whitworth & Summers, 1985) that range from the "inside-out" collapse solution (Shu, 1977, hereafter the Shu model) to the Larson-Penston solution (Larson, 1969; Penston, 1969; Hunter, 1977, hereafter the LP model). Both of these collapse processes assume isothermality and spherical symmetry. The LP solution is based on an initially uniform density distribution, which evolves to a power-law distribution $\rho \propto r^{-2}$ at large radii, and then collapses to $\rho \propto r^{-3/2}$. The Shu model assumes a singular isothermal sphere $\rho \propto r^{-2}$ as the initial condition. A perturbation in the central region starts the collapse, and the collapse wave propagates outward with the sound speed. The region outside the collapse wave stays unperturbed ($\rho \propto r^{-2}$), while the inner region is undergoing gravitational collapse. Figure 1.2 shows the density profile of the Shu model at different times. The inner region is approximately free-fall infall with steady mass accretion rate and $\rho \propto r^{-3/2}$.

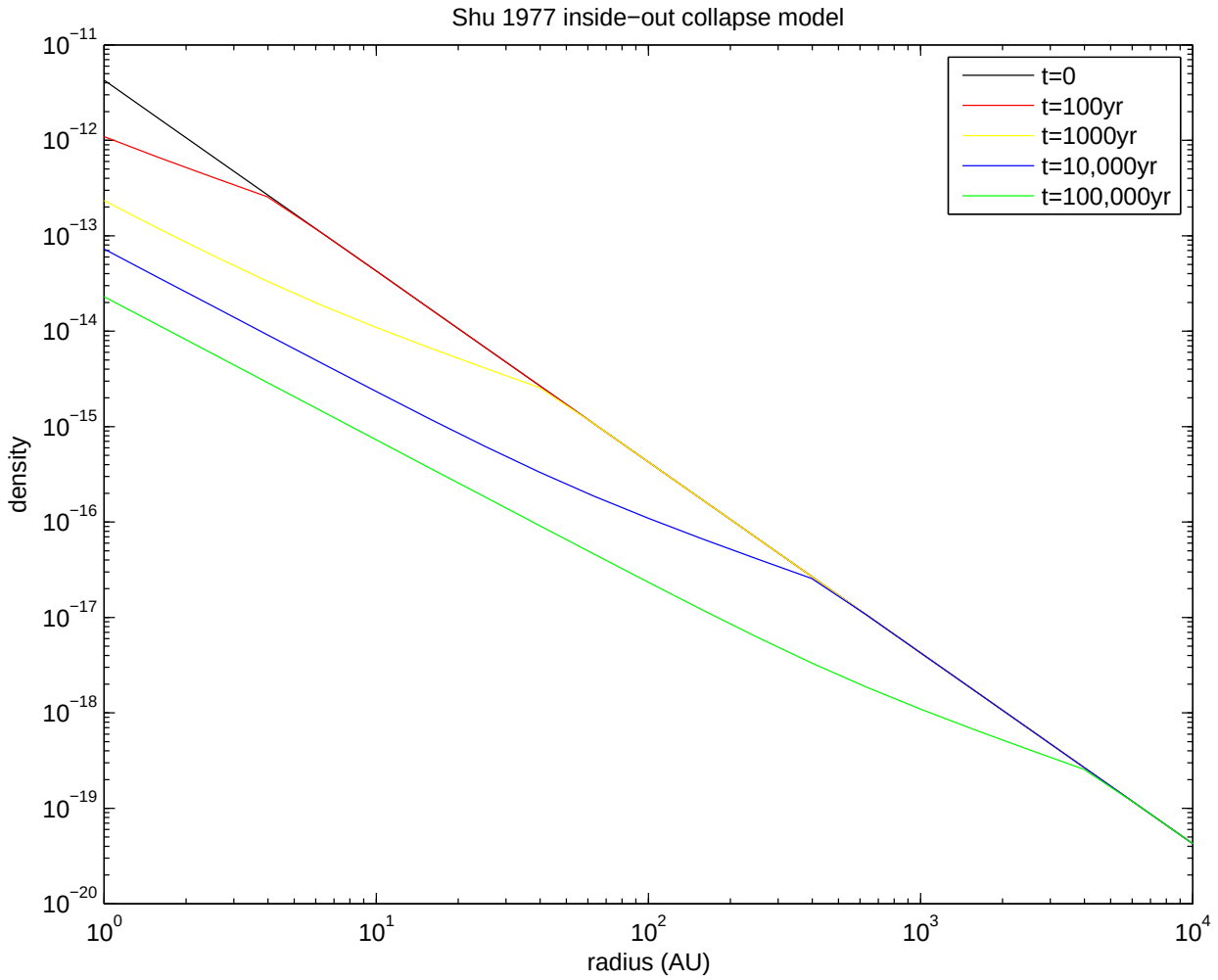

Figure 1.2 Density profile of the Shu model at $t = 0$, 10^2, 10^3, 10^4, 10^5 yrs. The collapse wave propagates inside-out with the sound speed. The region outside the collapse wave stays unperturbed ($\rho \propto r^{-2}$), while the inner region is undergoing gravitational collapse.

Both the LP model and the Shu model generally obtain an inner envelope with a power-law density profile $\rho \propto r^{-3/2}$ that increases in radius with time, surrounded by an outer envelope with $\rho \propto r^{-2}$. The major difference is the mass infall rate. The mass infall rate of the LP solution is much larger than that of the Shu solution. Therefore sometimes they are referred to as the fast and the slow collapse; the actual infall rate is likely somewhere in between.

Rotation can significantly affect the envelope structure and the collapse process. The angular momentum carried by a large cloud does not have enough time to be transferred to the external region while the cloud is collapsing. Conservation of angular momentum makes the material collapse onto a disk instead of a central star (e.g., Ulrich, 1976; Cassen & Moosman, 1981). The collapse process outside the centrifugal radius is similar to the spherically symmetric case, while rotation dominates in the inner region to form a flattened structure. Based on the Shu model, Terebey, Shu, & Cassen (1984, hereafter the TSC model) consider a rotating envelope undergoing gravitational collapse. With the initial solid-body rotation, material falls onto the midplane, defined as the plane perpendicular to the rotation axis, following the streamline equation

$$\frac{r}{r_c} = \frac{\sin^2\theta_0}{1 - \cos\theta/\cos\theta_0}, \tag{1.1}$$

where r_c is the centrifugal radius ($r_c = r_0^4\Omega^2/GM$). The density distribution can be expressed as

$$\rho = \frac{\dot{M}}{4\pi(GMr^3)^{1/2}}(1 + \frac{\cos\theta}{\cos\theta_0})^{-1/2}(\frac{\cos\theta}{\cos\theta_0} + \frac{2\cos^2\theta_0}{r/r_c})^{-1}. \tag{1.2}$$

Figure 1.3 shows the iso-density contours of the TSC model. To practically apply this model density distribution, one needs to solve the stramline equation for each location in the envelope in order to obtain $\cos\theta_0$, then Eq. (1.2) can be used to evaluate the density.

Dense cores are unlikely to be perfectly round and spherically symmetric. In fact, observations have shown that cores and envelopes are usually elongated, or even irregularly

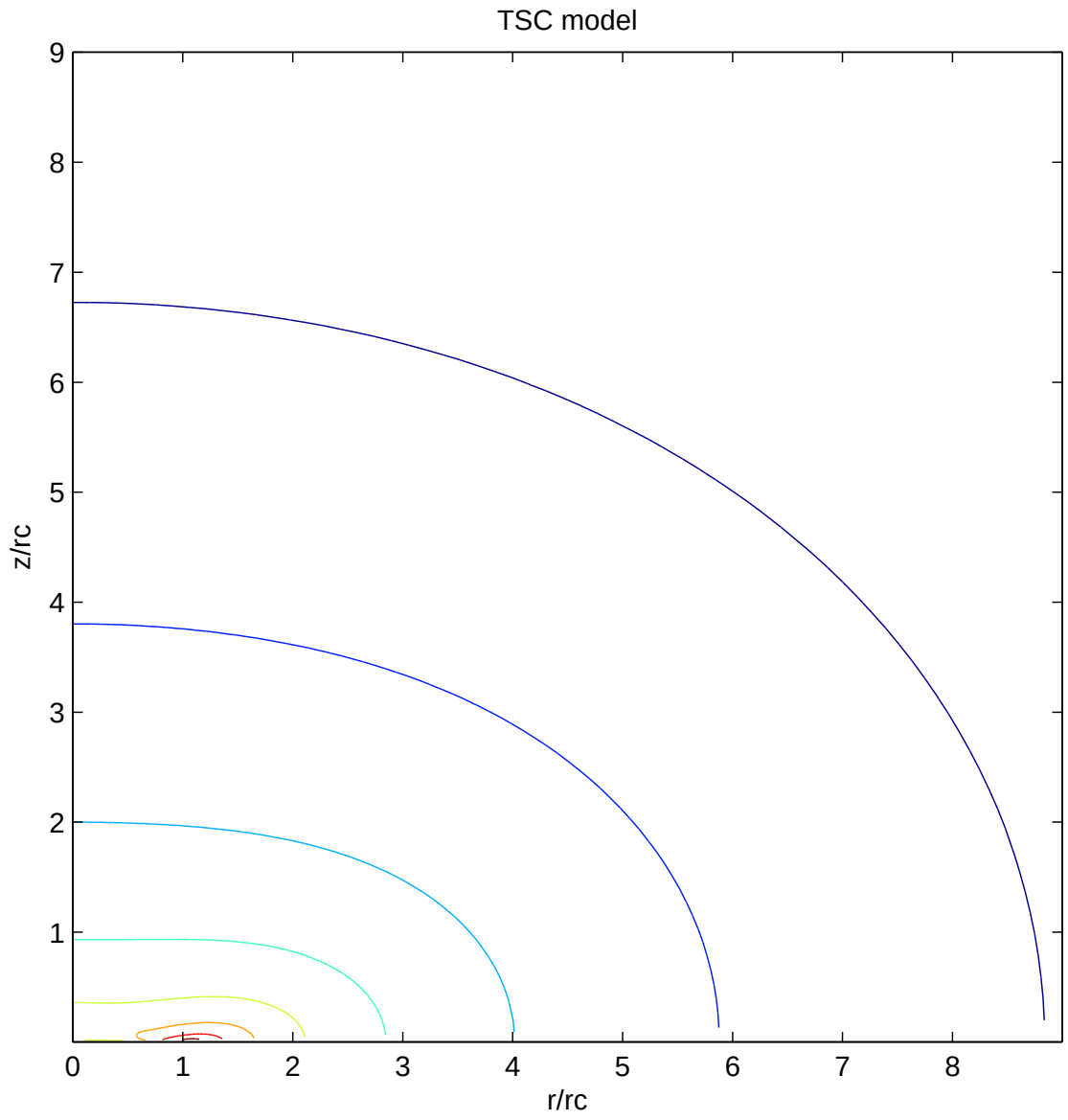

Figure 1.3 Iso-density contours of the TSC model, shown on a logarithmic scale. Size scales are in units of the centrifugal radius r_c. Each subsequent contour represents a factor of two change in density.

shaped (e.g., Myers et al., 1991; Tobin et al., 2010b). The initial geometry of the collapsing cores can play a role in the collapse process as well. In addition to the simplest spherical geometry, filaments, sheet, and flattened shapes have been considered. For example, Hartmann et al. (1994) considered a non-rotating isothermal flat sheet which is initially in hydrostatic equilibrium. Their numerical calculations show an outside-in collapse, in which the infall velocity is the largest in the outer region in the beginning, followed by a process that is similar to the Shu's inside-out collapse once the mass is dominated by the central object. A flattened envelope structure is also expected if the effects of magnetic fields are considered. For example, non-rotating MHD models predict a large disklike structure in cloud cores (Fiedler & Mouschovias, 1993) and the "pseudodisk" that forms after the central protostar forms (Galli & Shu, 1993).

Nonlinear perturbations, or turbulence, provide support against the gravitational collapse and affect the infall process. The effect depends on the velocity of the random motions and the driving mechanism, which are, however, uncertain. Therefore, the role of turbulence in the star formation process is still under debate (e.g., reviews of Mac Low & Klessen, 2004). Gong & Ostriker (2009) considers supersonic converging flows in spherical cores with initially uniform density. The collapse develops outside-in and then the infall expansion wave propagates inside-out. A density profile similar to the LP solution ($\rho \propto r^{-2}, v \propto r^{0}$) is built up through a shocked converging flow, with the region inside the rarefaction wave approaching free-fall infall ($\rho \propto r^{-3/2}, v \propto r^{-1/2}$).

Another controversy in star formation is the effects of magnetic fields, which can significantly regulate the whole star formation process (e.g., Masunaga & Inutsuka, 2000a; Hennebelle & Fromang, 2008). Given a high enough degree of ionization, the material is frozen into the magnetic field lines, and the magnetic flux remains constant throughout the collapse process. In this case, gravitational contraction is permanently prohibited if the initial mass-to-flux ratio is less than a critical value. A magnetically subcritical cloud may become supercritical and allow gravitational collapse if the ion-neutral collisions are insuf-

ficient to couple ions and neutrals together and neutrals are able to move across the field lines. This non-ideal MHD effect is called ambipolar diffusion, and can be important for envelope-disk formation and evolution. The theory of ambipolar-diffusion-initiated star formation predicts the formation of thermally and magnetically supercritical protostellar cores inside magnetically subcritical parent clouds (see reviews of Mouschovias, 1996; Mouschovias & Ciolek, 1999).

In the framework of the ambipolar-diffusion-induced collapse, Tassis & Mouschovias (2005a,b, hereafter TM2005) studied the accretion process after a protostar has formed at the center of the core. TM2005 have constructed a six-fluid MHD simulation to study the accretion process of matter from a molecular cloud core onto a protostellar object in the presence of magnetic fields. In their model, they track the evolution of magnetic flux and six kinds of particles (neutral molecules, atomic and molecular ions, electrons, neutral grains, negatively-charged grains, and positively-charged grains, among which only the electrons are assumed to be attached to the magnetic field lines) in a self-gravitating, accreting molecular cloud core. The simulation starts with a magnetically supported parent cloud. Ambipolar diffusion leads to the formation of a thermally and magnetically supercritical core that begins to contract dynamically. The innermost part forms a hydrostatic protostellar core while the envelope undergoes infall. As time progresses and mass and magnetic flux accrete onto the protostar from the envelope, a region of enhanced magnetic field, called the "magnetic wall," forms and drives an outward-propagating shock. Behind the shock, gravity dominates over the magnetic forces and reaccelerates the neutral particles, which continue to accrete onto the protostar until the next magnetic wall is formed. The magnetic wall forms and disperses in a quasi-periodic manner. Because of the presence of the magnetically controlled bursts, accretion from the envelope onto the protostar is episodic over the first 255 kyr. Figure 1.4 shows the density profiles at different times in a typical magnetic cycle.

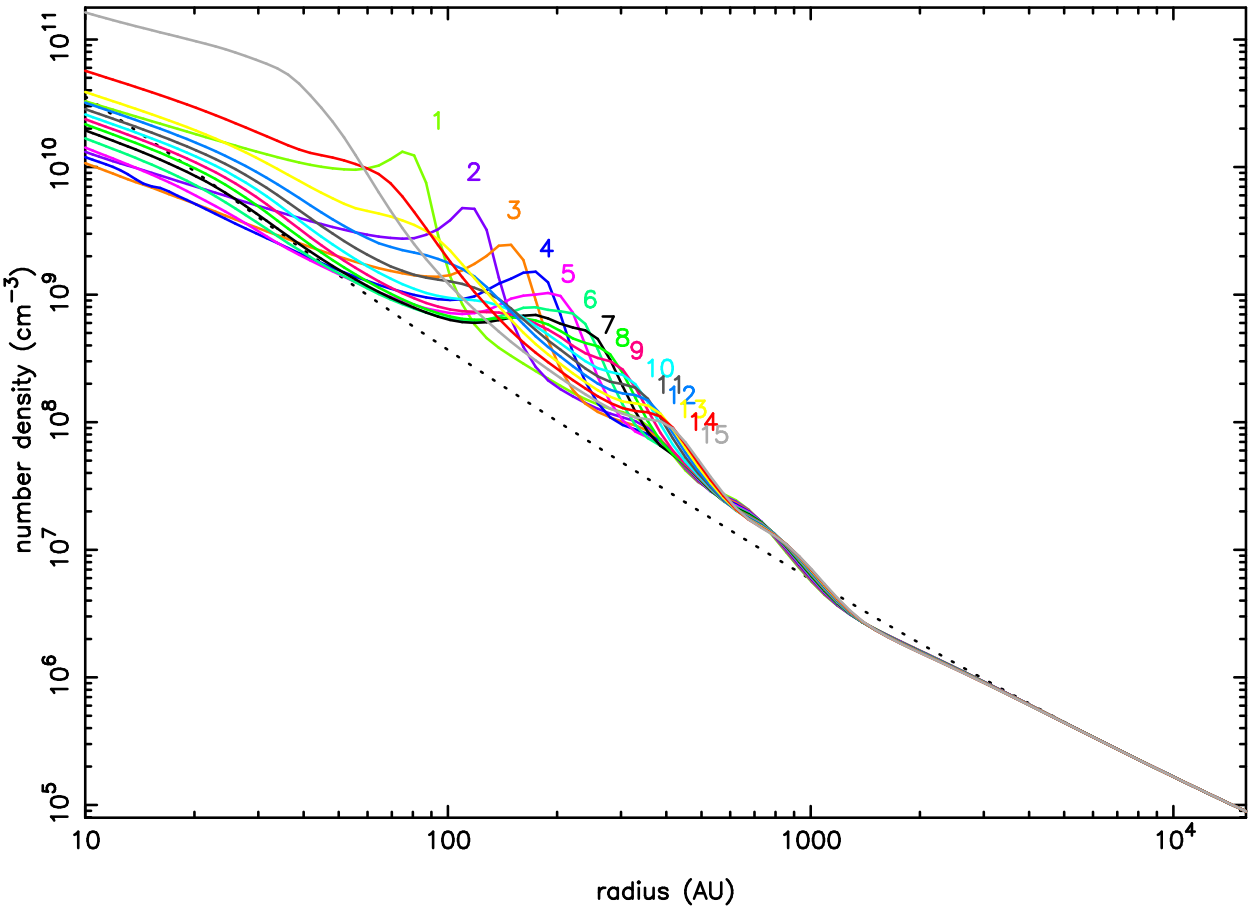

Figure 1.4 Density profiles of the TM2005 model. Dotted curve shows the initial profile when the protostar just forms. Solid curves represent a magnetic cycle and the labels 1–15 correspond to t = 33750, 34000, 34250, 34500, 34750, 35000, 35250, 35500, 35750, 36000, 36250, 36500, 36750, 37000, and 37250 yr after formation of the central protostar. The magnetic wall forms, propagates outward, and disperses throughout a cycle.

1.3 Thesis Outline

This thesis presents interferometric observations of Class 0 YSOs in both molecular lines and dust continuum, focusing on the circumstellar material around the protostars. For comparisons between models and data, radiative transfer modeling is performed and statistical inference is used to constrain the YSO properties.

Chapter 2 highlights the large flattened envelope around the edge-on Class 0 source L1157. The flattened structure, detected at both 8 μm extinction and N_2H^+ line emission, aligns perpendicular to the outflow direction, while a compact spherical dust continuum is observed. Kinematics of the flattened envelope is examined and a simple model is constructed to consistently interpret both gas and dust emission.

Chapter 3 examines the dust continuum of four Class 0 YSOs (NGC 1333 IRAS 4A, NGC 1333 IRAS 4B, NGC 1333 IRAS 2A, and L1448 IRS 3B) using archived BIMA data. While neither the LP model nor the Shu model can fit the observations with reasonable ages, we consider the magnetic model of Tassis & Mouschovias and successfully fit the data in a 1D approximation. Although the simplification of geometric structure may cause confusion, we show that the inner envelope structure is critical to infer any embedded disk component.

Chapter 4 continues the applications of magnetic models and considers an extremely young object predicted by Kunz & Mouschovias. While such a young object at a transient phase is only theoretically predicted so far and is not yet confirmed observationally, we carry out synthetic observations with Combined Array for Research in Millimeter-wave Astronomy (CARMA), Atacama Large Millimeter/Submillimeter Array (ALMA), and the Expanded Very Large Array (EVLA).

Chapter 5 revisits L1157 and presents dual-wavelength multi-configuration CARMA observations of dust continuum from $\sim 10^4$ AU scale down to $\lesssim 10^2$ AU. Full 3D radiative transfer modeling is performed to examine several theoretical envelope models. Bayesian statistics is introduced and details of the modeling procedures are specified. With the mod-

eling results, properties of dust grains and the embedded disk in Class 0 YSOs are discussed. Also, different envelope models are compared.

Chapters 6 concludes this thesis by summarizing the main results and discussing some future directions related to this work.

Chapter 2

Complex Structures around the Youngest Protostars: the Case of L1157

The majority of this chapter is previously published in The Astrophysical Journal as "Probing the Protostellar Envelope around L1157: the Dust and Gas Connection", Chiang, H.-F., Looney, L. W., Tobin, J. J., & Hartmann, L. 2010, ApJ, 709, 470 and is reproduced here with permission of the American Astronomical Society. More details about molecular column density estimation and spectrum fitting are appended in the end of the chapter.

We present observations of the Class 0 protostar L1157-mm using the Combined Array for Research in Millimeter-wave Astronomy (CARMA) in 3 mm dust continuum and N_2H^+ line emission. In the N_2H^+ line, we detect a large-scale envelope extended over a linear size of ∼20,000AU flattened in the direction perpendicular to the outflow. This N_2H^+ feature coincides with the outer envelope seen in the 8 μm extinction by Looney et al. Meanwhile, the dust continuum traces the compact, nearly spherical structure of the inner envelope, where N_2H^+ becomes depleted. This highly flattened N_2H^+ envelope also shows dynamical signatures consistent with gravitational infall in the inner region, but a slow, solid-body rotation at large scales. This flattened structure is not a rotationally supported circumstellar disk; instead, it resembles a prestellar core both morphologically and kinematically, representing the early phase of a Class 0 system. In this paper, we construct a simple model to interpret both the dust continuum and the N_2H^+ emission, and suggest a possible dynamical scenario for the overall properties of the envelope.

2.1 Introduction

Significant progress has been made both theoretically and observationally toward understanding low mass star formation in the last few decades, and an evolutionary sequence has been posited (e.g., Andre et al., 2000; McKee & Ostriker, 2007, Evans et al. 2009). The youngest protostars, the so-called Class 0 sources, form from the preceding stage of a prestellar core and are deeply embedded in their natal collapsing envelope. As a link from prestellar cores to young protostars, these envelopes contain valuable physical clues to the initial conditions of the collapse process. While single-dish telescope observations alone are usually limited by large beamsize, interferometry has allowed high resolution studies of the Class 0 envelope. In particular, interferometric observations combined with dust modeling using theoretically predicted structure can probe the physical properties of the inner envelope (e.g., Looney et al., 2003; Chiang et al., 2008). Unfortunately, dust emission from the outer envelope is usually difficult to detect due to interferometer insensitivity to large-scale structure or the low-surface brightness of the extended emission. Molecular lines, on the other hand, trace specific components of the envelope and can detect regions of lower density. Further, as the line emission is dispersed over many velocity channels, the structures are less extended than the equivalent dust emission so less affected by interferometer resolving-out issues. However, uncertainty in abundances and chemistry in the envelope can make molecular line interpretation difficult.

Since the first detection in Turner (1974) and confirmation in Thaddeus & Turner (1975), N_2H^+ has been a well-known interstellar molecule and an excellent tracer of dense cores (e.g., Caselli et al., 2002; Chen et al., 2007). With a critical density of around 10^5 cm^{-3} (e.g., Daniel et al., 2006), N_2H^+ is sensitive to the outer envelope around Class 0 YSOs. Also, N_2H^+ has a low depletion rate and remains in the gas phase when other molecules such as CO have depleted onto grains (Bergin & Langer, 1997). The reason for this was thought to be the low binding energy of its parent molecule N_2, but recent experiments have shown that the

binding energy of N_2 is not much lower than that of CO (Öberg et al., 2005). In fact, most of the nitrogen is in atomic form, which has a binding energy lower than the molecular form, and therefore making N_2H^+ harder to deplete (Maret et al., 2006). In this paper, we use N_2H^+ as an envelope tracer to reveal the gas in the outer protostellar envelope, as well as pursue a comparison between gas and dust.

While most Class 0 protostellar envelopes have rather complex structures, L1157-mm (also known as L1157-IRS or IRAS 20386+6751) in the Cepheus Flare (e.g., Kun et al., 2008; Kirk et al., 2009) has a highly flattened and relatively symmetric envelope $2'$ across seen by 8 μm absorption (Looney et al., 2007; Tobin et al., 2010b). The protostar is in the Class 0 stage with an estimated age of 8-150 kyrs (Froebrich, 2005, based on bolometric temperature, bolometric luminosity, and submillimeter luminosity). Different components of the dust emission, including a central compact core and an extended envelope, have been observed (e.g., Gueth et al., 1997, 2003; Beltrán et al., 2004). Also, large-scale outflows have been detected by various molecules, suggesting an inclination angle of 80° (Gueth et al., 1996) and a kinematic age of 15 kyrs derived from the oldest pair of outflow clumps (Bachiller et al., 2001; Arce et al., 2008, and reference therein). Furthermore, detection of methanol has suggested active accretion in the embedded circumstellar disk (Goldsmith et al., 1999; Velusamy et al., 2002). With features of a typical Class 0 young stellar object, L1157 seems to be a good example of isolated low mass star formation.

Unfortunately, the distance to L1157 is uncertain. The distance of 440 pc, based on spectroscopy and photometry of the illuminating star HD200775 of NGC 7023, is commonly used (see Kun et al., 2008), while the distance of the neighboring L1147/L1158 complex was determined to be 325 pc by the extinction-distance relationship in Straizys et al. (1992). Later, the Cepheus cloud was found to have three characteristic distances 200 pc, 300 pc, and 450 pc in Kun (1998). Multiple layers of clouds make it difficult to know the exact distance to a specific region. For easier comparison with the study of Looney et al. (2007), we adopt 250 pc in this paper.

We present interferometric observations of L1157-mm using the Combined Array for Research in Millimeter-wave Astronomy (CARMA; Bock et al., 2006) [1]. [2] The dust continuum at 3 mm and the N_2H^+ gas emission are observed and studied. The observational setup and the results are in §2.2 and §2.3. We estimate the column density of the N_2H^+ emission (§2.4.1) and compare it with the previous detection of the flattened envelope at 8 μm absorption (§2.4.2). The N_2H^+ abundance is examined in §2.4.3. We construct a simple model to interpret both the dust continuum and the N_2H^+ gas emission in §2.4.4. In addition, the gas kinematics of the large-scale envelope is discussed in §2.4.5. An overall link between gas and dust at multiple scales in this system is concluded in §2.4.6, followed by a summary in §2.5.

2.2 Observations

The observations were carried out with CARMA in October 2008 in E configuration and March 2009 in D configuration. The system temperature ranged from 150 to 300K (single sideband, SSB) during source observations. D and E configurations are the two most compact configurations of CARMA and give angular resolutions of around 5.5″ and 10″ at 3 mm, respectively. Because of the short antenna separations (8-66 m) in E configuration, antennas can shadow each other when observing targets at low elevations. To minimize shadowing, the elevations were always above 30° throughout the observations. Also we checked and verified that no shadowed data of the source were included in the analysis.

CARMA is composed of nine 6.1m BIMA (Berkeley Illinois Maryland Association) antennas and six 10.4m OVRO (Owens Valley Radio Observatory) antennas [3]. At our observed

[1] http://www.mmarray.org

[2] Support for CARMA construction was derived from the states of Illinois, California, and Maryland, the James S. McDonnell Foundation, the Gordon and Betty Moore Foundation, the Kenneth T. and Eileen L. Norris Foundation, the University of Chicago, the Associates of the California Institute of Technology, and the National Science Foundation. Ongoing CARMA development and operations are supported by the National Science Foundation under a cooperative agreement, and by the CARMA partner universities.

[3] Currently eight 3.5 m antennas from SZA (Sunyaev-Zeldovich Array) are also combined with CARMA

frequency, the FWHM of the primary beams are 122″ and 70″ for the 6m and 10m dishes, corresponding to 30,500AU and 17,500AU, respectively. The sensitivity decreases significantly outside the FWHM. To observe the extended feature of L1157, we performed a 5 pointing mosaic observation across the disk-like structure found in Looney et al. (2007). The phase center of the central pointing is set at the position of the protostar, $\alpha = 20^h39^m06\overset{s}{.}26$ and $\delta = 68°02'15\overset{''}{.}8$, determined by the dust continuum peak from other high resolution CARMA observations (Chapter 5).

The correlator was set so that the N_2H^+ JF_1F=101-012 component at 93.1763 GHz was observed with a 2MHz bandwidth, which provided a velocity resolution of 0.098 km s^{-1}. Dust continuum was observed simultaneously with two 500MHz bands. During the observations, 1927+739 was observed every 18 minutes and used as the phase calibrator. Also, the bandpass calibrators were 3C454.3, 3C84, 3C345, and 1642+689 for different tracks, while the flux calibrators were Uranus and MWC349. The absolute flux uncertainty is around 10%; hereafter we only consider the statistical uncertainty. All observational data were reduced and imaged using the MIRIAD software package (Sault et al., 1995) [4]. For the maps shown in this paper, natural weighting is used for Fourier transforming the visibilities into the image space.

2.3 Results

2.3.1 Dust Continuum

Figure 2.1(a) shows the 3 mm dust continuum map. With a beamsize of 7.3″×6.5″ (1825 AU×1625 AU) in the combined D- and E-array CARMA data, the dust emission is compact and nearly spherical. We used the MIRIAD task imfit to fit the dust emission with a Gaussian, and the results are given in Table 2.1. We detect the spherical protostellar envelope, but the embedded early circumstellar disk is not resolved. The dust continuum seen by

[4] http://carma.astro.umd.edu/miriad

Table 2.1. Summary of 3 mm Dust Continuum

parameter	value
Peak flux density (mJy beam^{-1})	30.3
noise level σ (mJy beam^{-1})	1.0
Total flux density (mJy)	48.3 ± 0.7
Gaussian fit	
Major axis (arcsec):	9.4 ± 0.9
Minor axis (arcsec):	8.1 ± 0.4
Position angle (degree)	-68 ± 18
Deconvolved Size	
Major axis (arcsec)	6.1 ± 2.3
Minor axis (arcsec)	4.4 ± 0.8
Position angle (degree)	-54 ± 21

Note. — The results of Gaussian fit with the dust continuum done by the MIRIAD task imfit.

CARMA is more compact than that seen by single-dish observations (e.g., 850 μm and 1.3 mm maps in Shirley et al., 2000; Gueth et al., 2003), implying that the large-scale extended emission is resolved out by the interferometer. A more careful modeling of the dust envelope is done in §2.4.4.

2.3.2 N_2H^+ Gas

Figure 2.1(b) and Figure 2.2 show the integrated intensity (zeroth moment map) and the velocity channel maps of the N_2H^+ isolated hyperfine component JF_1F=101-012. The star marks the position of the central protostar. We detect large-scale N_2H^+ emission across an elongated region perpendicular to the outflow direction (see the greyscale image in Figure 2.3(a) for the outflow orientation). The disk-like structure extends over 80″, which corresponds to a linear size of ∼20,000 AU assuming a distance of 250 pc. Due to the large size,

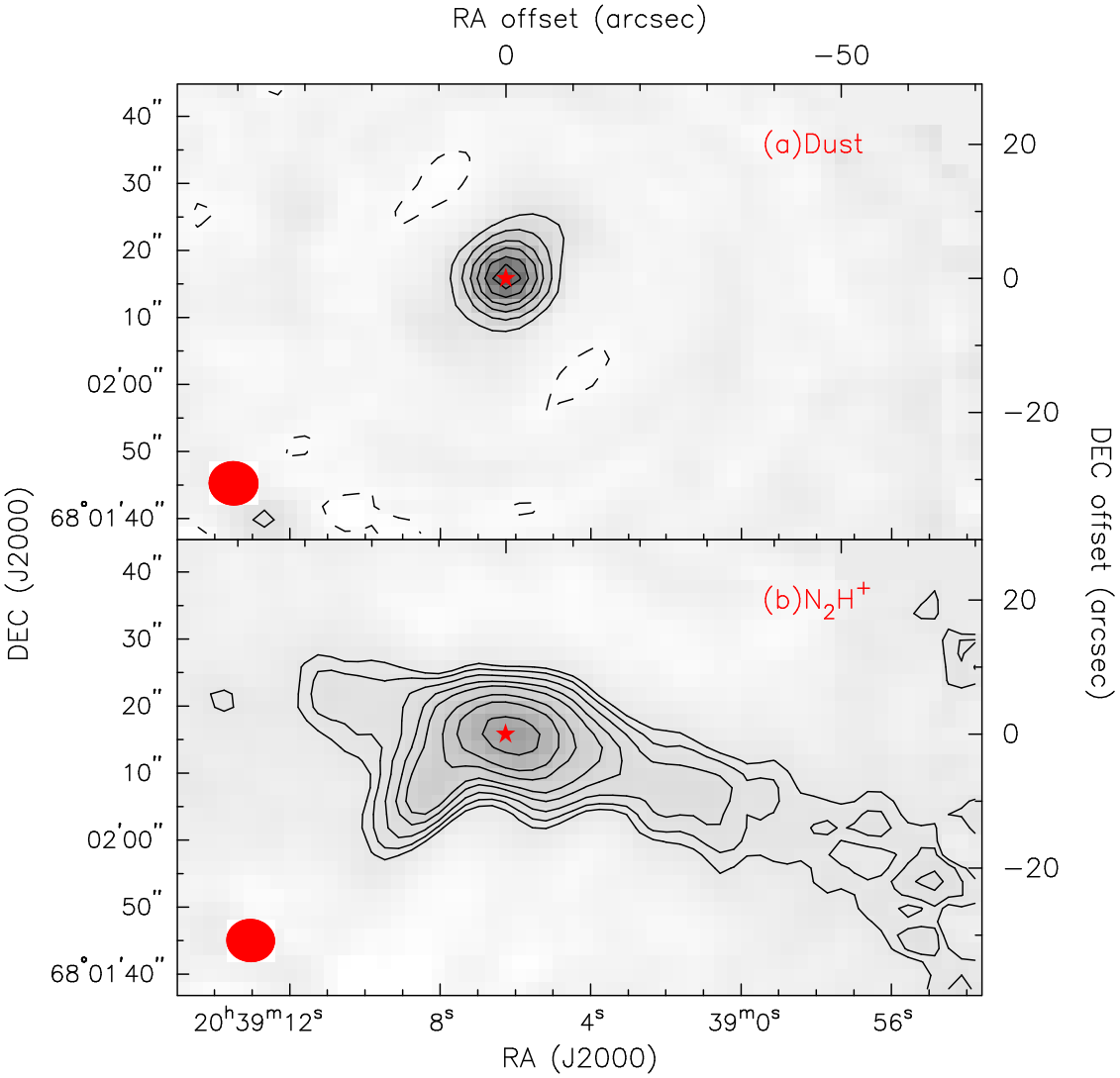

Figure 2.1 (a) The 3 mm dust continuum of L1157 (*contours and greyscale*). The contour levels are [-2, 3, 6, 10, 14, 20, 26]$\times\sigma$, where σ=1 mJy beam^{-1} is the noise level, and the beamsize is 7.3″×6.5″ at a position angle of 86.1°. (b) The integrated intensity of N_2H^+ over the isolated hyperfine component JF_1F=101-012 (2.21-3.58 km s^{-1}, *contours and greyscale*). The star marks the position of the central protostar. The contour levels are [3, 6, 10, 15, 20, 30, 40, 60, 80]$\times\sigma$, where σ=0.01 Jy beam^{-1} km s^{-1}, and the beamsize is 7.1″×6.3″ at a position angle of 86.6°. Although negative contours exist due to the filtered-out large-scale structures, they are not plotted for simplicity.

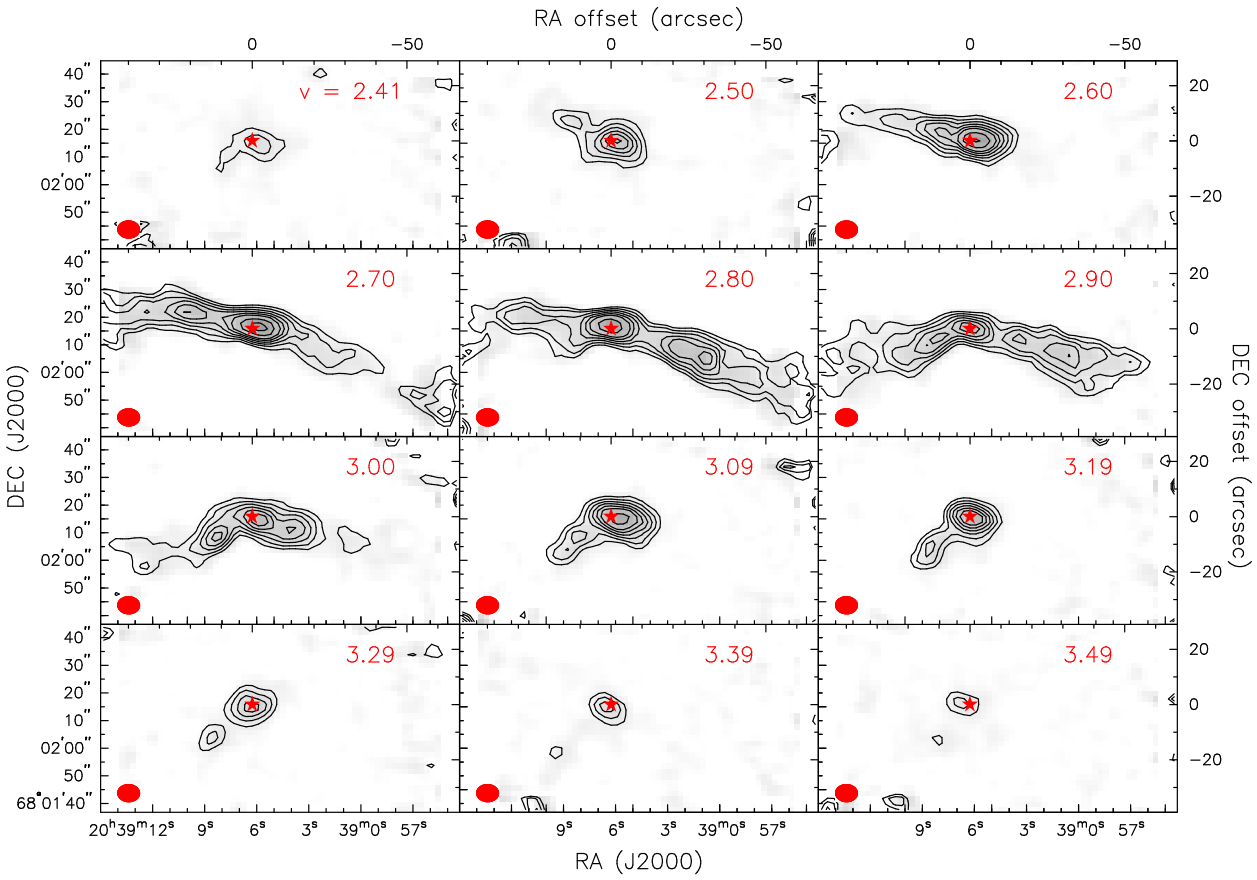

Figure 2.2 The channel maps of L1157 for the N_2H^+ JF_1F=101-012 transition (*contours and greyscale*). The numbers in the upper-right corner are the LSR velocity for each channel. The star marks the position of the central protostar. The contour levels are [2, 3, 4, 5, 6, 7, 9, 11]$\times\sigma$, where σ =0.08 Jy beam^{-1}, and the beamsize is 7.1″×6.3″ at a position angle of 86.6°. Negative contours are not plotted for simplicity.

it is unlikely to be a rotationally supported disk (see §2.4.5.2). Hence, we call it a flattened envelope in this paper.

The N_2H^+ gas shows interesting dynamics of the flattened envelope in Figure 2.2. Systematically, the east wing has lower velocity than the west wing, suggesting rotation or bulk motion. The dynamics of the system will be discussed more in later sections. The spatial distribution is clumpy. In particular, the extended emission toward the east-south roughly follows the interface of the envelope and outflow cavity, suggesting dynamical or chemical interaction between outflow and envelope. The effects of outflows on the morphology of N_2H^+ emission are also seen in other YSOs (e.g., Chen et al., 2008). In addition, the emission

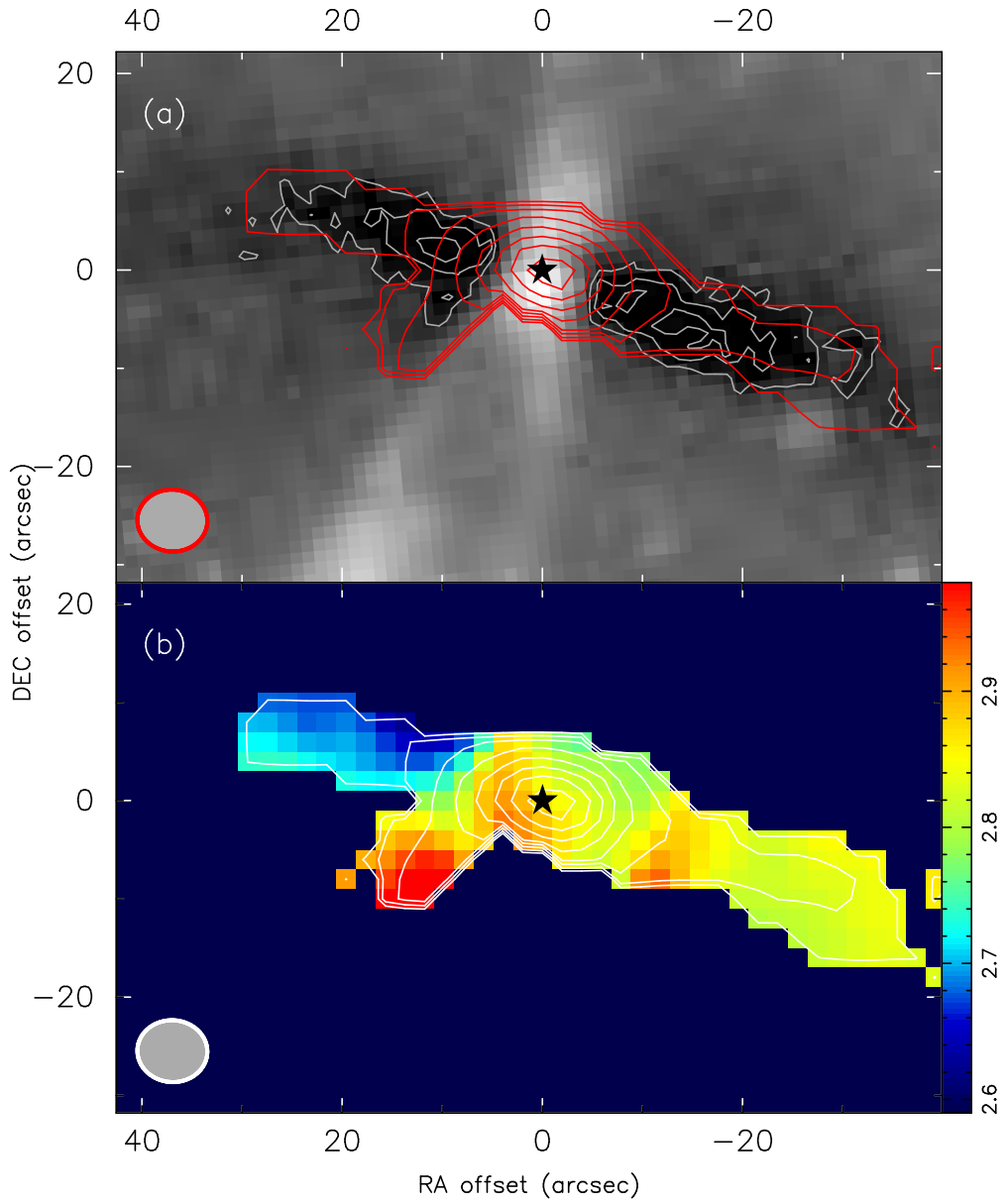

Figure 2.3 (a) IRAC 8 μm image of L1157 (Looney et al., 2007, *grayscale and gray contours)* overlaid with N_2H^+ column density (*black/red contours*) derived from the CARMA observations. The star marks the position of the protostar. The (*black/red*) contour levels for the N_2H^+ column density are [0.1, 0.5, 1.0, 1.5, 2.0, 2.5, 3.0, 3.5]$\times 10^{13}$cm^{-2} (see text for discussion of uncertainty); and the (*gray*) contours showing the absorption features are [7, 8, 9, 10]$\times$ σ, where $\sigma = 0.042$ MJy^{-1}sr^{-1} is the noise level. The circle at the lower-left corner shows the beamsize of the CARMA observations. (b) Velocity map (v_{LSR}) overlaid by the column density contours from (a), both derived from the CARMA observations of the N_2H^+ flattened envelope.

extends to the very west of the observational field of view and becomes blended with noise. In this study we do not consider the western clumps (see Figure 2.1(b)); instead, we focus on the main part of the flattened envelope.

2.4 Analysis and Discussion

2.4.1 The Column Density of the N_2H^+ Feature

The N_2H^+ molecule (diazenylium) has 15 J=1-0 rotational transitions; spectroscopically, 7 sets of hyperfine components are observed because the lower state energy levels J=0 are degenerate within 10^{-6} Hz (e.g., Daniel et al., 2006). The relative rest frequencies of the components were determined by Caselli et al. (1995). The so-called isolated component, the JF_1F=101-012 component together with JF_1F=101-010 and 101-011 at 93.176258 GHz (Lee et al., 2001), is not blended with the other sets of hyperfine components and is ideal for studying dynamics. We perform spectrum fitting for pixels with more than 3 S/N detection of N_2H^+ on the integrated intensity map, except the very west region close to the edge of the field of view, where the spectrum fitting fails to be reliable. For simplicity, we assume a uniform excitation temperature T_{ex} = 10 K with the LTE approximation for the level populations. Also, Gaussian lines with the same linewidth are used (cf. GILDAS CLASS HFS procedure [5] and Shirley et al. 2005). The isolated component accounts for a ratio of 3/27 of the total N_2H^+ emission (Daniel et al., 2006), with which we convert our observed data to total emission accordingly. Then we calculated the best fit values of opacity $\langle\tau\rangle$ (average τ among seven hyperfine sets, see Shirley et al., 2005), FWHM of velocity dispersion Δv, and v_{LSR} for each pixel using the MATLAB function *nlinfit* [6]. A summary of the spectrum fitting as well as the uncertainty of fitting is in Table 2.2. In the optically thin limit and with the LTE assumption, the column density can be estimated with (Miao et al., 1995; Goldsmith

[5] http://www.iram.fr/IRAMFR/GILDAS/
[6] http://www.mathworks.com/

Table 2.2. Summary of N_2H^+ Spectrum Fitting

parameter	central pixel	mean value	mean σ
v_{LSR} (km s^{-1})	2.85	2.82	0.02
Δv(km s^{-1})	0.80	0.44	0.03
$< \tau >$	0.63	0.31	0.03
Derived values :			
Column Density(10^{12} cm^{-2})	38.3	9.7	3.2

& Langer, 1999)

$$\mathcal{N}_{tot} = 2.04 \frac{Q(T_{ex})\, e^{\frac{E_u}{kT_{ex}}}}{\theta_a \theta_b \nu^3 \mu^2 S} \left[\frac{B_\nu(T_{ex})}{B_\nu(T_{ex}) - B_\nu(T_{bg})} \right] C_\tau \int I_v \, \mathrm{d}v \times 10^{20} \mathrm{cm}^{-2} \quad , \tag{2.1}$$

where θ_a and θ_b are observational beamsize in arcsec, ν is the frequency in GHz, μ is the dipole moment in debye, S is the line strength, E_u is the upper state energy level, $B_\nu(T)$ is the Planck function at temperature T, I_v is the specific intensity in Jy beam^{-1}, v is velocity in km s^{-1}, C_τ is the opacity correction factor

$$C_\tau = \frac{\tau}{1 - e^{-\tau}} \quad , \tag{2.2}$$

$Q(T_{ex})$ is the rotational partition function

$$Q_{rot}(T_{ex}) = \sum_{J=0}^{\infty} (2J+1) e^{-\frac{E_J}{kT_{ex}}} \approx \frac{kT_{ex}}{hB} \tag{2.3}$$

(Goldsmith & Langer, 1999), $E_J = J(J+1)hB$ is the energy level for the rotational transition, and B is the rotational constant. For linear molecule N_2H^+, μ is 3.40 debye and B is 46586.867 MHz (JPL catalog: Pickett et al., 1998; Green et al., 1974). Since the emission is more extended than the beam size, the beam filling factor is assumed to be 1 across the map. Also, the background temperature T_{bg} is assumed to be constant 2.73K.

Altogether, the estimated N_2H^+ column density is shown by the dark contours in Figure 2.3, with the velocity map shown in colormap in Figure 2.3(b). The average column density is $\sim 1.0\times10^{13}$cm^{-2} with a peak of $\sim 3.8\times10^{13}$cm^{-2} close to the protostar. The uncertainty varies across the map and has a mean value of $\sim 3\times10^{12}$cm^{-2}.

The uncertainties of the column density estimation are dominated by the assumptions of spectrum fitting. First, the largest error source for the derived column density is the uncertainty of the excitation temperature T_{ex}. Typically, the excitation temperature in dense cores and protostars is around 4-15K, depending on the source properties (e.g., Benson et al., 1998; Shirley et al., 2005; Kirk et al., 2007; Chen et al., 2007). In previous single-dish observations, the N_2H^+ excitation temperature of L1157 was determined to be 8.9K by Emprechtinger et al. (2009), in general agreement with the rotational temperature of 13K obtained in Bachiller et al. (1993) using NH_3 emission. In this study we assume a constant excitation temperature of 10K, and impose an uncertainty of 3K that is propagated with the other parameters. We used additional CARMA data that contain all hyperfine components in a lower spectral resolution for spectrum fitting with the CLASS package, and confirmed that the excitation temperature is around 10K near the protostar.

Second, we assume that the N_2H^+ lines are optically thin. In fact, the average opacity from our spectrum fitting is 0.31, consistent with the assumption of optically thin. Nonetheless, the correction factor helps mitigate the errors propagated to column density. In addition, any self-absorption effect is neglected given the optically thin assumption. However, the optically thin approximation becomes worse toward the center, where $\tau=0.63\pm0.03$.

LTE is assumed for the level populations of the rotational transitions. A constant proportionality between the hyperfine components is also adopted. The variation of the relative strengths between the hyperfine components as discussed in the appendix of Shirley et al. (2005) is ignored in this study.

For simplicity, we assume only one velocity component for the spectrum fitting, although this is not true in the inner envelope. We use a single Gaussian to fit the spectra over the

map to estimate the N_2H^+ column density. The simplification is insufficient for the more complex velocity structures near the center, but the resulting difference is smaller than the uncertainty caused by the excitation temperature assumption. For the kinematics of the envelope, see later sections for further discussion.

Unlike most N_2H^+ studies, we fit the N_2H^+ spectrum using only the isolated component instead of all 7 sets of transitions. The 2MHz bandwidth in our observations cannot cover all 7 sets simultaneously, so the excitation temperature distribution cannot be derived based on the relative strength between hyperfine components; therefore we assume a uniform excitation temperature. However, the difference should not be significant; it has been suggested that the two approaches give results consistent within frequency resolution (e.g., Mardones et al., 1997; Emprechtinger et al., 2009).

Indeed, our derived N_2H^+ column density of L1157 is comparable to other studies. For example, the column density was reported to be 1.7×10^{13}cm^{-2} in Bachiller & Perez Gutierrez (1997) and 1.1×10^{13}cm^{-2} in Emprechtinger et al. (2009), both using the IRAM 30m telescope with HPBW of $27''$ with different assumptions of excitation temperature. Our average column density (1.0×10^{13}cm^{-2}) is slightly lower, as expected due to the interferometer resolving out large-scale emission.

2.4.2 Correlation between N_2H^+ and 8 μm Absorption

The extended feature of N_2H^+ emission coincides with the flattened absorption structure found in Looney et al. (2007). Figure 2.3 shows the absorption feature at 8μm overlaid with the contours of N_2H^+ column density. At 8 μm, the PAH emission provides a bright background, against which the dust extinction is detected. Note that the spatial resolution of *Spitzer* IRAC (the diffraction limit is $1.8''$) is better than our N_2H^+ observations (beamsize is $7.1''\times6.3''$). In general, the morphology of the absorbing dust is consistent with the N_2H^+ gas, except the central region where the bipolar outflow feature dominates. From the 8 μm map, the observed opacity is obtained given the assumption of a constant background

estimated off-source. In Looney et al. (2007), a simple model of the flattened envelope was constructed; however, the power-law index of the density profile could not be constrained.

The observed opacities were converted into total column density and mass in Looney et al. (2007) with the assumption of a mass absorption coefficient of dust plus gas $\kappa_{8.0\mu m}$=5.912 cm^2g^{-1} from Li & Draine (2001). The total absorbing mass was estimated to be 0.19 $M_\odot$ in Looney et al. (2007). For a comparison, the mass of the same extended region is $\sim$0.76 $M_\odot$ based on the derived N_2H^+ column density and a hypothetical constant N_2H^+ abundance $n(N_2H^+)/n(H_2)$ of 3.0×10^{-10}. The central part of the flattened envelope is excluded here. Although most concentrated, the central region is dominated by the outflow activities at 8 μm; therefore the method of optical depth determination in Looney et al. (2007) is not applicable for regions within $\sim$8.4$''$ of the protostar. Also, the chemistry can become more complicated near the center so that the real N_2H^+ distribution is not trivial. Furthermore, this comparison should not be overemphasized because of the following complexities: (1) an uncertain assumption of the N_2H^+ abundance, (2) interferometric filtering, (3) the uncertainty of $\kappa_{8.0\mu m}$, and (4) ignorance of foreground emission when estimating mass using 8 μm absorption (Tobin et al., 2010b).

Nevertheless, the total column density, including gas and dust estimated from the 8.0μm extinction in Looney et al. (2007), can be compared with the N_2H^+ column density derived from our spectrum fitting in this study. To facilitate the comparison for the flattened structure, we plot the profiles along the major axis of the flattened structure in Figure 4. Figure 2.4(a) shows the N_2H^+ and estimated total column density, derived respectively from CARMA and *Spitzer* IRAC observations, for a cut of position angle 75° from north to east. The circles with error bars are the total column density from the absorption feature in Looney et al. (2007), and the thick curves with shades is the N_2H^+ column density from this study.

As mentioned in the last section, the dominating uncertainty of the N_2H^+ column density comes from the assumption of the excitation temperature T_{ex}. In our spectrum fitting, a constant T_{ex} of 10K is assumed. We estimate the uncertainty by imposing an uncertainty

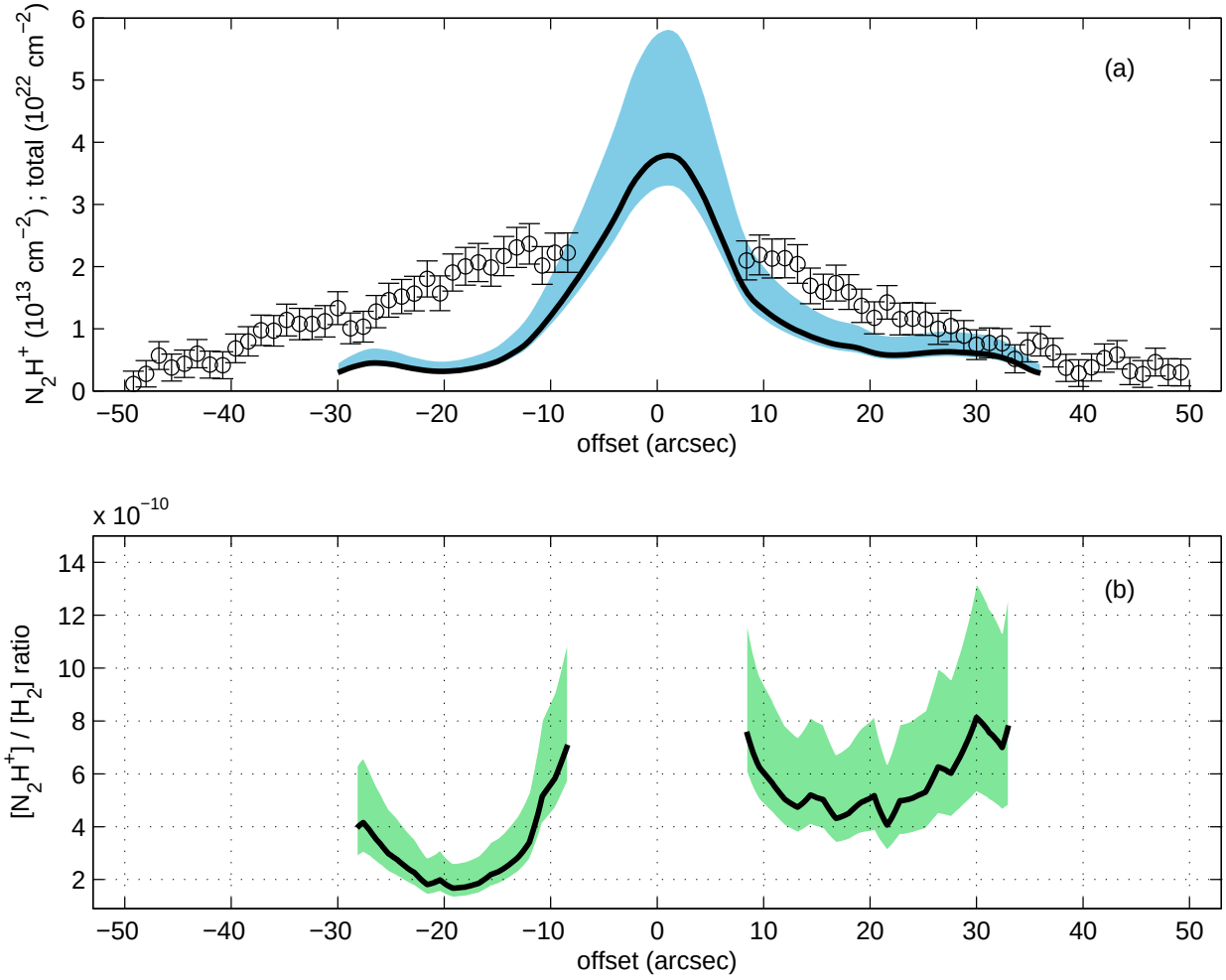

Figure 2.4 (a) Column density of N_2H^+ (from our CARMA observation, *curve with shading*) and total gas plus dust (from *Spitzer* observation, *circles with error bars*) along the major axis of the extended envelope. (b) N_2H^+ abundance profile by taking the ratio of [N_2H^+] and [H_2] from the CARMA observations and 8 μm absorption feature. The shaded region shows the uncertainty.

of excitation temperature ΔT_{ex}=3K and the propagated error is shown as a color shaded region in Figure 2.4. Because the column density is monotonically increasing with T_{ex} (from Eq. (2.1) and Eq. (2.3), $\mathcal{N}_{tot} \propto Q(T_{ex})e^{\frac{E_1}{kT_{ex}}} \propto T_{ex}e^{\frac{E_1}{kT_{ex}}}$), the upper and lower bounds of the shaded region correspond to T_{ex}=13K and 7K, respectively.

2.4.3 N_2H^+ Abundance

We estimate the N_2H^+ abundance by taking the ratio of $[N_2H^+]$, from our CARMA observations, and $[H_2]$, derived in Looney et al. (2007), along a cut of the extended envelope. In Figure 2.4(b), the ratio of $[N_2H^+]$ to $[H_2]$ as a function of offset is plotted. Only the region away from the central outflow-dominating zone and with more than 3 S/N of N_2H^+ detection is considered here. While the radial profile of the 8 μm absorption shows a good symmetry between east and west wings, the profile of N_2H^+ does not. The N_2H^+ column density drops in the west wing faster than the east. The average N_2H^+ abundance is 3.0×10^{-10} in the east wing, lower than the average abundance 5.7×10^{-10} in the west wing. Our estimate of N_2H^+ abundance is smaller than the value derived in Bachiller & Perez Gutierrez (1997, 3.8×10^{-9}), while the difference can come from a different estimate of H_2 column density and interferometric filtering. Nonetheless, the overall N_2H^+ abundance is consistent with most chemical models. The typical N_2H^+ abundance $[N_2H^+]/[H_2]$ for prestellar cores and Class 0 YSOs varies from 10^{-11} to 10^{-9} (e.g., Aikawa et al., 2005; Maret et al., 2007; Tsamis et al., 2008), and likely changes with YSO evolution (e.g., Bergin & Langer, 1997).

Enhancement of N_2H^+ abundance close to the center is seen in the east wing (Figure 2.4(b)). This trend is also expected by chemical models. While the preceeding objects, starless cores, have been shown to have constant N_2H^+ abundance (Tafalla et al., 2002), the abundance profile evolves as a function of radius in the collapsing cores (e.g., the numerical chemical models: Lee et al., 2004; Aikawa et al., 2005; Tsamis et al., 2008). In particular, the formation and destruction of N_2H^+ is closely related to other species by the chemical reactions with N_2 and CO (Womack et al., 1992; Jørgensen et al., 2004b). The dominant

route to form N_2H^+ is through

$$H_3^+ + N_2 \rightarrow N_2H^+ + H_2, \tag{2.4}$$

while it is destroyed by dissociative electron recombination at high temperature

$$N_2H^+ + e^- \rightarrow N_2 + H, \tag{2.5}$$

and CO destroys N_2H^+ in the gas phase by the reaction

$$N_2H^+ + CO \rightarrow N_2 + HCO^+. \tag{2.6}$$

Therefore, when CO starts to deplete onto dust grains at densities around 2-6 $\times 10^4$ cm^{-3} (e.g., Tafalla et al., 2002) in the inner envelope, the abundance of N_2H^+, as well as other N-bearing molecules, increases.

On the other hand, depletion of N_2H^+ is also expected in the inner envelope. The depletion density is around 10^6 cm^{-3} to 3×10^7 cm^{-3}, above which the gaseous N_2H^+ start to deplete (Bergin & Langer, 1997; Aikawa et al., 2003). However, whether depletion is seen in our observations is not clear due to the fact that the region with density higher than the depletion density is not well resolved with the observational beamsize. Also, information of extinction and total column density is missed owing to the bright outflow activity at 8 μm, making us unable to obtain the N_2H^+ abundance near the center. Furthermore, the CO molecules, existing in the outflows or evaporated from the dust grains in the very inner envelope due to the heating from the central protostar, can destroy the N_2H^+ molecules (Lee et al., 2004); the CO outflow and evaporation effects can look similar to the depletion effect from the observational point of view. Eventually, a more careful study for L1157, such as Evans et al. (2005) for B335, a similar protostar at the same evolutionary stage as L1157, will be needed to consider multiple species and understand the system more thoroughly.

2.4.4 Simple Dust Modeling

While a large scale flattened envelope is detected by N_2H^+ emission, the dust emission at 3 mm is compact and round; the goal in this section is to construct a model that can interpret both. To do so, we begin with fitting the dust continuum. We constructed a model that has a flattened geometry similar to the N_2H^+ feature and predicts an observed spherical dust continuum.

We have developed a radiative transfer code that considers density and temperature structures in 3 dimensions to do the dust continuum modeling, and compare with visibilities from interferometric observations. First, a map of flux density is obtained with high numerical resolution given a model envelope. For each pixel on the plane of sky, the flux is calculated by integrating the dust emission along the line of sight (e.g., Adams, 1991). The specific intensity can be expressed as

$$I_\nu = \int_{los} B_\nu(T)\, e^{-\tau_\nu}\, \mathrm{d}\tau_\nu = \int_{los} B_\nu(T(\vec{r}))\, e^{-\tau_\nu(\vec{r})}\, \rho(\vec{r})\, \kappa_\nu\, \mathrm{d}\vec{r}, \tag{2.7}$$

where $B_\nu(T)$ is the Planck function at dust temperature T, τ_ν is the optical depth from the position $\vec{r}$ along the line of sight to the observer, ρ is the envelope density, and $\vec{r}$ denotes the position. T, ρ, and τ_ν are all functions of $\vec{r}$. In this study, the opacity of dust grains κ_ν is assumed to be uniform throughout the envelope. We simulated all observational effects from the interferometric observations. The image is corrected by the primary beam effect according to the antenna size, and Fourier transformed into visibilities with the observational u-v sampling. In the case of CARMA, the 6m BIMA dishes and 10m OVRO dishes give 3 different primary beams. Therefore we constructed separate primary-beam-corrected images for each kind of baseline, and sampled them with corresponding u-v spacings from real observations. However, the mosaic pattern was not considered in the dust modeling, although a 5-pointing mosaic was used in the observations. The dust continuum is very compact with size much smaller than the FWHM of the primary beam, hence the effect is insignificant.

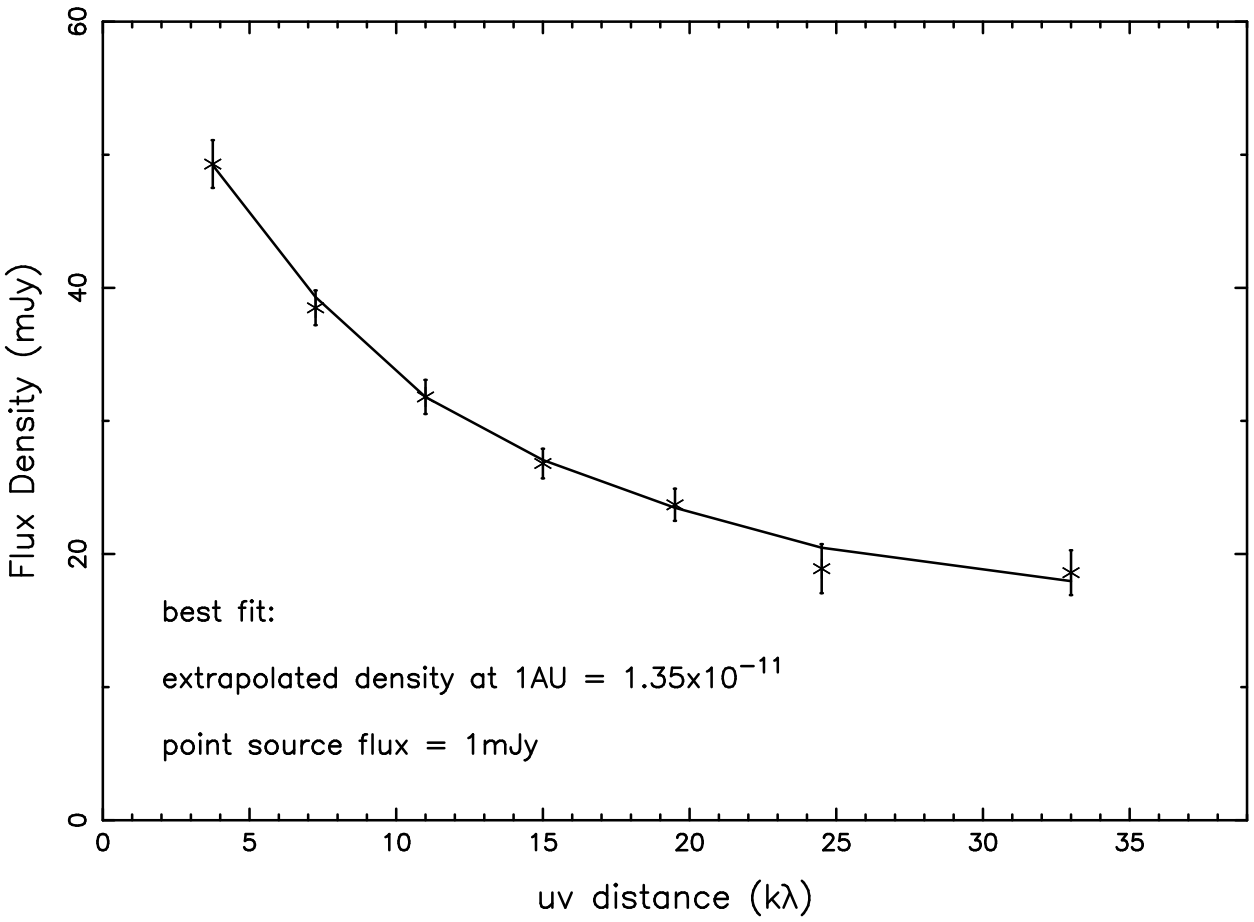

Figure 2.5 The annuli-averaged flux density for the 3mm dust continuum of L1157 (*crosses with error bars*). The curve show the best fit model binned in the same fashion. The dust model has a power-law density profile with index = -2 tapered by a vertical Gaussian with a scale height of 2000AU. The extrapolated density at 1AU is 1.35×10^{-11} g cm^{-3} and an unresolved point source flux of 1mJy is added. The inner radius of the envelope is 5AU, and the outer radius is 15000 AU. The reduced χ^2_r is 0.225 for this best fit model.

Finally, the modeled visibilities are binned into *u-v* annuli around the source center and averaged vectorially. The flux density for each bin is compared with the observations, which are binned in the same way using the MIRIAD task uvamp, as shown in Figure 2.5 by crosses with error bars. A χ^2_r value is calculated to quantify the goodness of a fit. The comparison is done in visibility space so uncertainty from imaging processes such as the CLEAN algorithm is avoided.

The code has been tested for accuracy and convergency. The results of spherically symmetric cases were checked by comparing with those obtained by previous codes used in

Looney et al. (2003) and Chiang et al. (2008). Because of the nature of higher density and higher derivatives in the inner envelope, smaller stepsizes are required for the inner region. On the other hand, stepsize is not as sensitive for the outer region, so computing time is saved by using coarser steps. In the current code, three refinements of stepsizes are used with extra fine steps taken for the very central region to achieve accuracy better than observational uncertainties. Also, cases of different numerical resolutions have been run to check convergency. In this study, the numerical resolution is 37.5AU, corresponding to $0.15''$ for L1157. Higher numerical resolution gives consistent flux density within a difference smaller than 0.05 mJy. In addition, the code itself does not assume any symmetry. In other words, the model of envelope density and temperature can be arbitrary in three dimensions.

With the observed flattened structure in mind, we construct a model envelope of similar morphology. For simplicity, we adopted a power-law density and temperature profile. To impose the flattened geometry, we use a spherically symmetric distribution and taper the density profile with a Gaussian mask diminishing along the minor axis of the disk orientation. In our model, the vertical scale height of the Gaussian is fixed to be 2000 AU for an ellipticity close to the observed flattened feature. We orientate the flattened envelope as the observed N_2H^+ feature, that is, with a position angle of 75°. We also adopt an inclination angle of 80°, as determined from outflow observations (Gueth et al., 1996). However, the temperature distribution remains spherically symmetric.

Note that this model is not physically motivated, but it interprets the observations with statistical significance. We adopt a power-law index of -2 for the density structure, similar to a singular isothermal sphere in the extreme case of a Bonnor-Ebert sphere (Shu, 1977). The dust temperature profile is a power law of index $-2/(4+\beta)$, where β is the spectral index of opacity, from the spherically symmetric approximation assuming the heating is dominated by the central source (Adams, 1991). We set the extrapolated temperature at 1AU to be 300K and a lower limit of 5K representing the external heating from cosmic ray or interstellar radiation.

For the dust grain properties, a fiducial value of the mass opacity coefficient κ_{3mm}=0.0056 cm^2g^{-1} is adopted, based on κ_{1mm}=0.01 cm^2g^{-1} (e.g., Natta et al., 2004) and $\beta = 0.5$ (Kwon et al., 2009). The exact value of κ is uncertain and can vary by an order of magnitude dependent on the grain properties (e.g., the interstellar MRN grains in Draine & Lee 1984 and the coagulated grains in Ossenkopf & Henning 1994). Nevertheless, κ_ν is expected to follow a power law with frequency ν at long wavelengths, that is, $\kappa \propto \nu^\beta$. The extrapolation at millimeter wavelengths is determined by the spectral index β, which is dependent on grain size, grain geometry, chemical composition, etc (Draine, 2006). For a young object like L1157, grain growth may have already started in the inner region. For simplicity, the dust grain properties is assumed to be uniform across the envelope and not dependent on the radius. The possible radial gradient of grain properties, which was recently reported by Kwon et al. (2009), is neglected in this study.

We have explored two parameters: point source flux (F_p), representing the flux contribution from the embedded circumstellar disk system inside the inner radius of the model envelope, and the extrapolated density at 1AU (d_1), scaling with the total mass. A grid of model parameters is run with F_p from 0 to 30 mJy in steps of 1 mJy, and d_1 from 4×10^{-12} to 20×10^{-12}g cm^{-3} in steps of 0.5×10^{-12}g cm^{-3}. The inner and outer radius of the envelope are fixed to be 5AU and 15000AU, respectively. Varying the outer radius of the envelope does not make a big difference because little flux is emitted from the low density region compared to the denser region. Also, the interferometer resolves out some of the large-scale emission. The inner radius is correlated to the point source flux and can be chosen as long as it is much smaller than the observational spatial resolution, while physically the dust destruction radius is of the order of 0.1AU, inside which the temperature is too high for dust to exist. A summary of the χ^2_r model fitting is shown in Figure 2.6. The filled circle marks the best fit and the contours show the parameter ranges with different confidence levels. The two parameters are correlated and cannot be clearly distinguished, because either a big density scaling factor d_1 or a high point source flux F_p can result in a high peak of flux density.

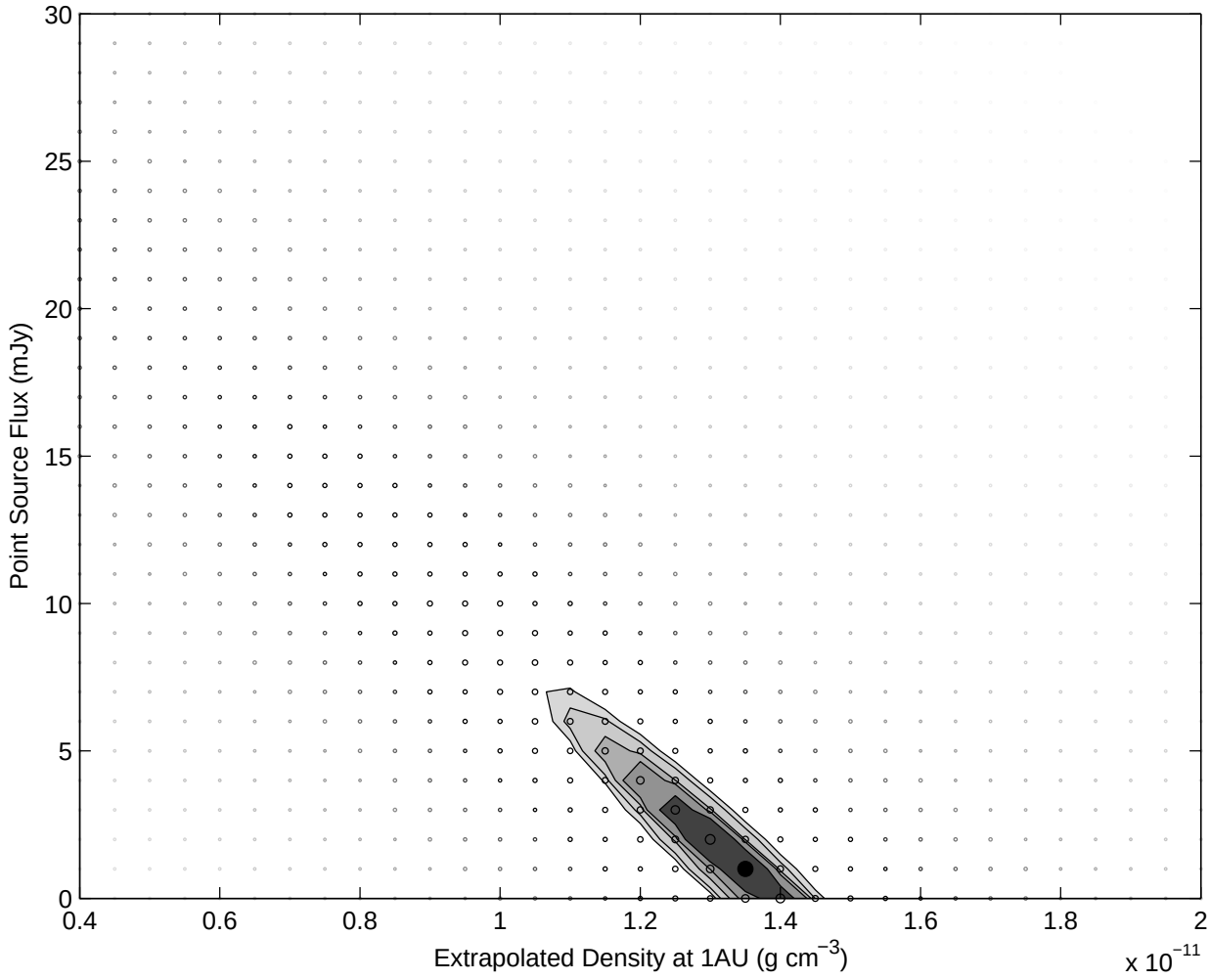

Figure 2.6 Summary of the dust continuum fits. Circles show the grid of models with sizes and shades representing the goodness of fits. Contours are confidence levels of 99%, 95%, 90%, 80%, and 50%. The filled circle at 1.35×10^{-11}g cm^{-3} and 1 mJy is the best fit.

The best fit model has a point source flux $F_p = 1$ mJy and extrapolated density at 1AU $d_1 = 1.35\times10^{-11}$g cm^{-3}. A total envelope mass of 1.5 $M_\odot$ is then implied in our model; this mass is generally consistent with other mass estimates (e.g., Shirley et al., 2000; Gueth et al., 2003; Froebrich, 2005). The modeled flux density of the best fits as a function of u-v distance is shown by the curve in Figure 2.5.

We estimate the corresponding N_2H^+ column density of the best fit model obtained from the dust continuum fitting. To do the conversion, the dust-to-gas ratio is assumed to be uniformly 1:100, as the typical value in the interstellar medium, and the N_2H^+ abundance is

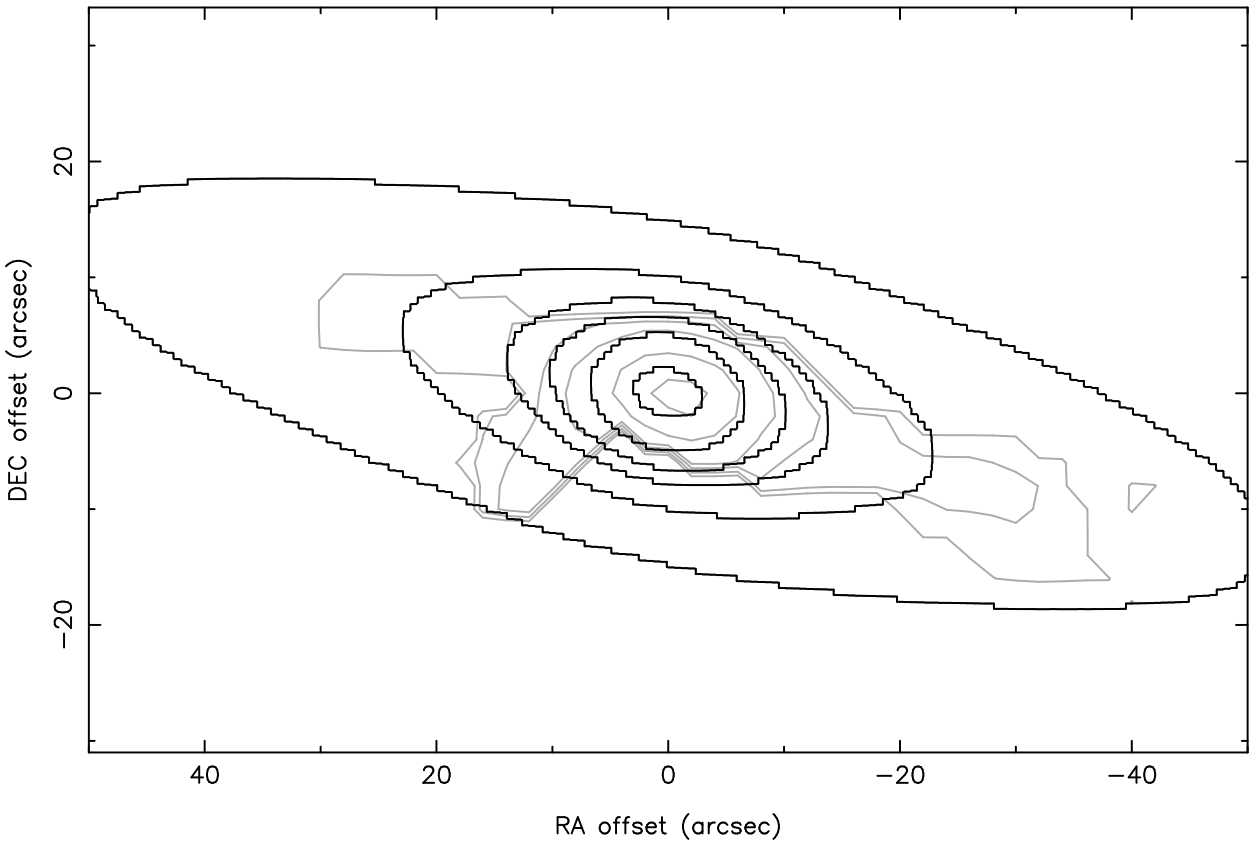

Figure 2.7 N_2H^+ column density of the best fit model by dust continuum modeling (*black contours*) and observations (*grey contours*). The contour levels (for both) are [0.1, 0.5, 1.0, 1.5, 2.5, 3.5]$\times 10^{13}$cm^{-2}. The depletion effect is taken into account at the central region where the density is above 1.5×10^{6}cm^{-3}.

assumed to be uniformly 3.0×10^{-10}. Further, we simulate the depletion effect by introducing a threshold depletion density, above which the N_2H^+ density does not increase with H_2 density. We adopt a depletion density of 1.5×10^{6}cm^{-3}. To compare with observations, N_2H^+ volume density is integrated along the line of sight to calculate the column density across the map. The model N_2H^+ column density and the detected N_2H^+ emission are shown in Figure 2.7.

As seen in Figure 2.7, our best fit dust model gives a consistent map of N_2H^+ column density. This simple model illustrates how we do not observe extended dust continuum while the N_2H^+ emission is detected to be extended more than 80″ across. The dust emission, which depends on both density and temperature, in the outer region of the flattened envelope is

too weak to be detectable by these observations.

2.4.5 Gas Kinematics

The complex N_2H^+ spectral information reveals a composite system of multiple dynamic components (Figure 2.3(b)). To understand the detailed kinematics, we perform a simple analysis using the position-velocity diagram. Figure 2.8(b) shows the position-velocity diagram for the N_2H^+ JF_1F=101-012 component along the major axis of the flattened envelope at position angle 75° from north to east. This transition is isolated so no confusion is caused due to blending with other hyperfine lines.

We construct a simple model to simulate the position-velocity diagram assuming various velocity structures of the envelope. Note that the kinematics modeling is independent of the dust modeling, except that the best-fit density structure from the previous section is used. We adopt the procedure as discussed in Ohashi et al. (1997a) and consider a spatially thin cut along the major axis of the envelope. Both the inclination and opacity effects are ignored. The column density in each velocity channel as a function of offset is estimated by integrating density along the line of sight and sorting into observational spectral bins by the projected velocity. The depletion effect is simulated by assuming constant N_2H^+ density for the central region where H_2 gas density is higher than $1.5\times10^6 \mathrm{cm}^{-3}$, the same depletion density as adopted in the previous section. With the depletion effect, the actual density structure of the inner envelope does not play a large role. The spatial distribution is then convolved with the observational beam. However, unlike the dust modeling, the interferometric filtering effects are not taken into account for the kinematics study. Nonetheless the large scale emission from background clouds is not included; this is similar to interferometry resolving out large scale emission. Lastly, the modeled results are shown by contours in position-velocity diagrams and compared with observations.

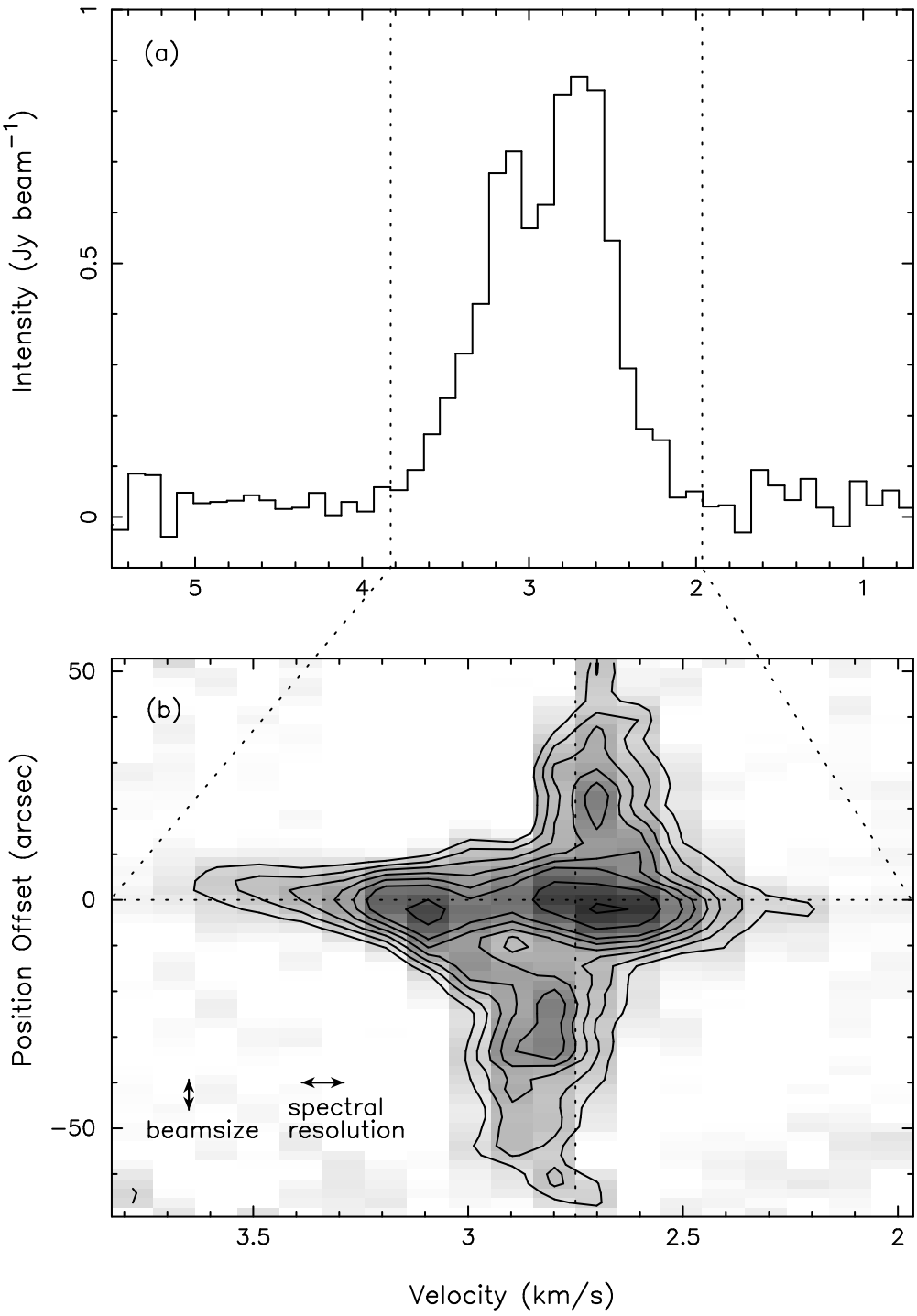

Figure 2.8 (a) Spectrum of the N_2H^+ JF_1F=101-012 line at the location of the protostar. (b) Position-velocity diagram of the N_2H^+ JF_1F=101-012 line along the major axis of the flattened envelope feature, a slice with position angle of 75°. The contour levels are [2, 3, 4, 5, 6, 7, 9, 11]$\times\sigma$, where σ =0.08 Jy beam^{-1}. The angular and spectral resolutions of observations are shown, and the pixel size of the grayscale is the interferometric imaging cell size.

2.4.5.1 Spectroscopic Signatures of Infall Motion

The double peaked feature seen in the central region indicates multiple velocity components in the protostellar envelope (Figure 2.8(a)). The red-shifted and blue-shifted peaks have a velocity difference of $\sim$0.4 km s^{-1}, inferring a relative motion between two parts of the envelope. One interpretation for this is the infall motion of the inner envelope, which can also be the cause of the high-velocity wings. Gravitational collapse takes place in the early stage of star formation (e.g., theoretical studies in Shu, 1977; Hunter, 1977; Tassis & Mouschovias, 2005a). However, the predicted infall velocity structures are very different from model to model, especially in the inner envelope. Detailed comparison of various theoretical models with observations is beyond the scope of this paper and may be studied with observations of higher spatial and spectral resolutions in the future. Nevertheless, infall is expected in the inner envelope of L1157. Previously, L1157 has been identified as an infall candidate by single dish (Gregersen et al., 1997; Mardones et al., 1997) and interferometric observations (Gueth et al., 1997; Beltrán et al., 2004). In addition, detection of methanol from the accretion shocks on the small scale also supports the picture of envelope material infalling onto the forming protostellar disk (Velusamy et al., 2002).

Figure 2.9(a) shows the modeled position-velocity contours for a pure infall motion. A simple velocity profile $v \sim r^{-1/2}$, representing ideal free-fall, is used. The simple infall model shows a double-peaked feature toward the center of the envelope, as obtained by Ohashi et al. (1997a). However, the model cannot explain the asymmetry of the peaks. A more sophisticated model that considers full geometry, radiative transfer, and different theoretical profiles such as Momose et al. (1998) may be necessary.

We exclude this double peaked feature as arising from self-absorption, commonly used as an indicator of infall motion in the prestellar cores (e.g., Evans, 1999). In such an approach of identifying infall candidates, a stronger blue-shifted peak and a weaker red-shifted peak are expected for infalling sources observed by an opaque line, because the front half of the cloud

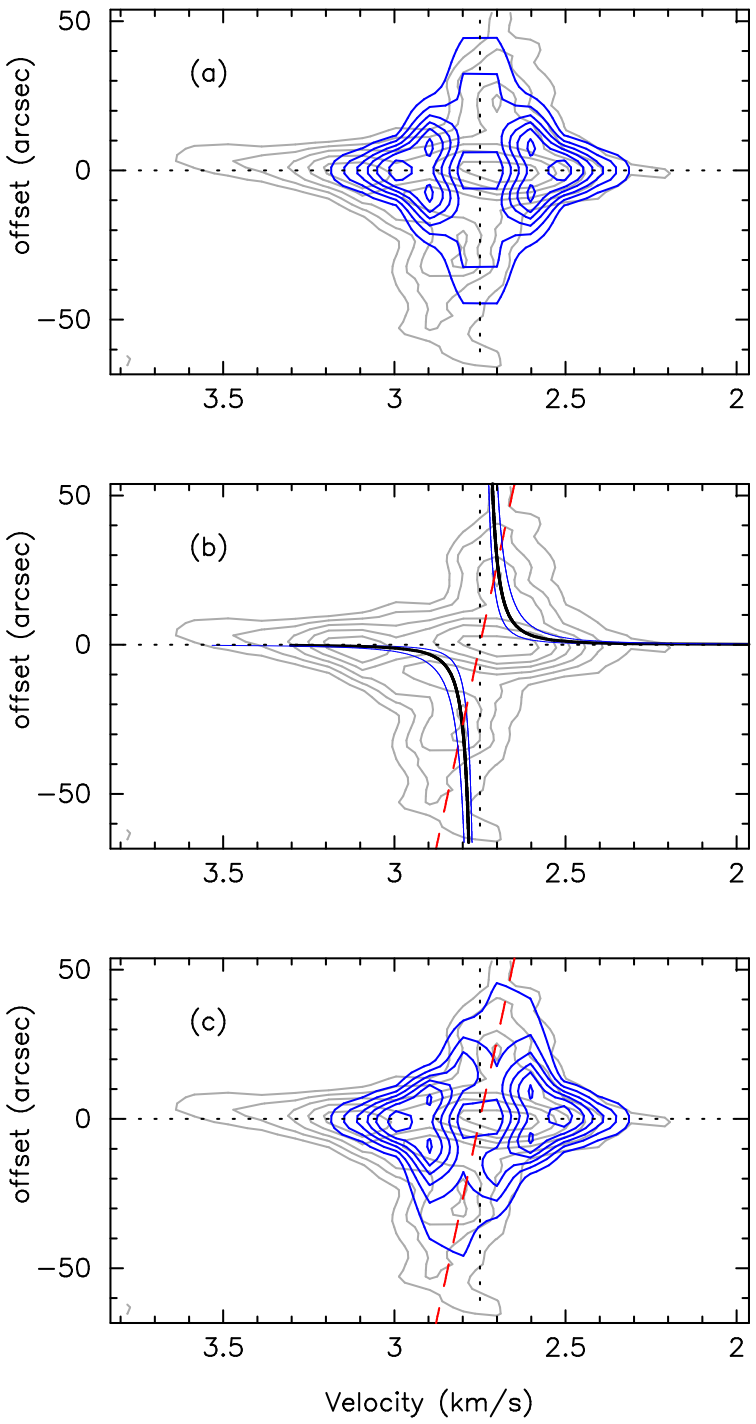

Figure 2.9 Observed (*grey contours*) and model (*black/blue contours*) position-velocity diagrams for the flattened envelope of L1157: (a) pure infall motion, (b) solid curves show the point mass Keplerian rotation for $M_\star$=0.01, 0.02, and 0.04 $M_\odot$, dashed line shows solid-body rotation with angular velocity of 1.5 km s^{-1} pc^{-1} , and (c) combined model of infall plus solid-body rotation.

causes a red-shifted absorption dip (e.g., Myers et al., 1996; Masunaga & Inutsuka, 2000b); while an optically thin line should be observed within two velocity peaks. In this specific case, since the N_2H^+ lines are moderately optically thin, this scenario of self-absorption is ruled out although a similar profile is observed. However, the spectrum is sensitive to the detailed envelope model such as optical depth, turbulent velocity dispersion, spatial structures of velocity, density, and excitation temperature, etc (e.g., Zhou, 1992; Ward-Thompson & Buckley, 2001). The complexity makes it difficult to justify the real physical properties causing the observed spectra. In addition, the interferometry selectively observes the small scale emission, leaving out the large scale static cloud in the outer envelope and resulting in spectrum with a deeper zero-velocity dip (Choi, 2002).

While a double peaked profile of N_2H^+ is seen in our interferometric observations, Mardones et al. (1997) observed the same line using IRAM 30m telescope, and found it to be single-peaked and used it as the optically thin reference to compare with other optically thick lines for studying infall. The same source was observed again by the IRAM 30m telescope in Emprechtinger et al. (2009) and similar results were obtained. These support our spectrum fitting results that the N_2H^+ J=1-0 lines are optically thin. The major differences of our observation are a smaller beamsize and the aperture synthesis. Therefore the cause of discrepancy is deduced to be (1) a beam-smearing effect and/or (2) interferometric filtering. While the overall spectrum is dominated by the inner envelope, the small scale structures are not distinguishable by the single dish observations. However, observations of higher resolutions with interferometers reveal other complexities. For example, the degree of profile asymmetry can be enhanced if observed with a higher angular resolution (Choi, 2002). Also, we test our modeling routine by convolving the spectrum with different beam sizes, and confirm the beam-smearing effect. A double-peaked feature can look like a single Gaussian if the observational beamsize is not able to resolve the infall radius.

Second and more importantly, interferometric observations reveal only the targeted protostellar envelope at the expense of missing flux from large-scale structures, arguably domi-

nated by the static foreground and background clouds. Choi (2002) has shown that missing short spacing flux can affect the self-absorption dip for optically thick lines. It can cause similar effects for optically thin lines too. In particular, large scale background material is mostly static compared to the infalling inner envelope and contributes more flux at the LSR velocity. Nonetheless, the material at the large scale cloud does not participate in star formation as actively as the inner envelope. For comparison with the spectrum of IRAM 30m single-dish observations (Mardones et al., 1997; Bachiller & Perez Gutierrez, 1997; Emprechtinger et al., 2009), we smooth our images with a 27″ Gaussian beam (the beamsize of IRAM 30m observations) and found that ∼20% of the total flux is filtered out by CARMA, also causing a dip around the LSR velocity.

A large linewidth of N_2H^+ J=1-0 is found by the single dish observations. The fitted linewidths of the single-peaked spectra are 0.71 and 0.65 km s^{-1} for the IRAM 30m observations in Mardones et al. (1997) and Emprechtinger et al. (2009), respectively. We compare the single-dish observations with our smoothed spectrum. If we fit our double-peaked spectrum with a single Gaussian, the FWHM is 0.88±0.05 km s^{-1}. But if we fit the spectrum with two Gaussians of the same width, the FWHM is 0.44 ±0.02 km s^{-1}, comparable to the sonic linewidth ∼0.45 km s^{-1} and smaller than the thermal linewidth ∼0.13 km s^{-1} with the assumed temperature of 10K. The dynamics at small scales can be obscured in single dish observations but can be revealed by high resolution interferometric observations. If this phenomenon is common to other sources, it may be why the average linewidth of Class 0 YSOs is large (∼0.61 km s^{-1}, Emprechtinger et al., 2009) compared to that of starless cores (0.2-0.4 km s^{-1}, Lee et al., 2001).

We cannot exclude the possibility that the double-peaked feature is caused by factors other than infall motion in the inner envelope. For example, outflows contaminate the molecular tracers of envelope material. A similar case of the Class 0 protostar B335 was studied by Wilner et al. (2000). While the single-dish observation matched well with the inside-out infall model (Zhou et al., 1993), the interferometric observation brought up a

more realistic scenario. The optically thin CS J=5-4 line is shown to be dominated by small scale outflow clumps in high resolution observations (Wilner et al., 2000). A single-peaked spectrum seen in low resolution observations can contain two velocity components and hence a double-peaked feature is shown with interferometric filtering. However, some molecular lines do not trace outflows as closely as other species. It has been suggested that N_2H^+ lines trace the quiescent cores but not the shocked outflow gas (Bachiller, 1996). The CO molecules in the outflows can destroy the N_2H^+ molecules (Eq. (2.6)). Indeed, while the abundance of some species is enhanced by the outflow shocks, N_2H^+ is not detected at the shock regions (Bachiller & Perez Gutierrez, 1997). In other words, the outflow contamination is minimized for this species, although some outflow effects are unavoidable (for example, see the outflow-envelope interface at the southeast extension in Figure 2.1(b)).

The double-peaked spectrum can also be caused by unrelated dense clumps that happen to be in the same line of sight. This is less likely because channel maps do not show traits of unrelated components. If clumps exist in the foreground or background, they are more likely to show up individually at a peculiar velocity. In contrast, the morphology of the envelope at different velocities are systematically consistent in our observations. Also, N_2H^+ does not pick up other velocity components as easily as CO because it requires high densities to form. Infall motion, not necessarily gravitational infall, is suggested.

2.4.5.2 Rotation

While axisymmetric infall cannot explain the velocity difference between the east and west extensions of the envelope, the differential velocity may come from rotation of the envelope. In this section, we test some simple rotation curves.

First we test Keplerian rotation. If the dynamics of the envelope is dominated by Keplerian rotation around a central point mass much larger than the cumulative envelope mass, the central mass has to be smaller than 0.1 $M_\odot$ to explain the observed velocity differential of the envelope. In Figure 2.9(b), the pure Keplerian curves for a point mass of 0.01, 0.02, and

0.04 are shown. Apparently, the deduced central mass is around or even smaller than the mass of the envelope, which means that the cumulative envelope mass cannot be neglected. This is expected because for Class 0 YSOs, mass is mostly distributed in the envelope rather than the central protostar (e.g., Andre et al., 1993). Next, we consider complete Keplerian rotation with cumulative envelope mass. The velocity is $(GM_R/R)^{1/2}$ where M_R is the mass contained within the radius R. An envelope with $\rho \propto r^{-2}$ gives a flat rotation curve. The best fit density obtained in the previous dust continuum fitting gives a roughly constant rotation velocity 0.5 km s^{-1}, much larger than the observed value. These exercises show that Keplerian rotation is ruled out for the large-scale envelope.

In fact, the system is too young to construct large-scale Keplerian rotation. For example, the period of rotation with velocity 0.2 km/s at 1,000 AU is $\sim$1.5$\times$10^5 yr, larger than the typical age of Class 0 protostars. As seen in the position-velocity diagram, the sizescale of rotation is around 10,000AU and requires even longer dynamical timescale. Again, the dynamical time estimation suggests the unsuitability of pure Keplerian rotation for this system.

Another possible scenario is that there exists solid-body rotation in L1157. This has been seen in other Class 0 YSOs such as HH212 (Wiseman et al., 2001). The solid-body rotation is probably inherited from the initial conditions of the large-scale clouds or filaments. Angular momentum plays an important role in the protostar evolution (e.g., Bodenheimer, 1995). In particular, the initial condition of rotation is closely related to the core morphology and fragmentation (e.g., Saigo et al., 2008). The extended envelope of L1157 has a velocity gradient of around 1.5 km s^{-1} pc^{-1} assuming solid-body rotation (shown by the dashed line in Figure 2.9(b) and (c)). The velocity gradient is much smaller than what was found in the survey of Class 0 protostars ($\sim$ 7 km s^{-1} pc^{-1}, Chen et al., 2007); instead, it resembles the typical velocity gradient found in the dense clouds (1-2 km s^{-1} pc^{-1}, Goodman et al., 1993; Caselli et al., 2002). Moreover, the rotating N_2H^+ envelope of L1157 has a size scale much larger than the typical size scale of collapsing envelopes. Both the large size and the slow

bulk rotation imply properties more similar to prestellar cores than collapsing envelopes. After the protostar has formed in the central densest region, the kinematics of the envelope can still be dominated by the remnant rotation of the parent dense cloud at large scales, while the infall motion takes over at small scales. The good alignment of the rotation with other features such as flattened geometry and outflow direction also suggest a consistent picture.

Considering the envelope with radius of 10,000AU and the fitted solid-body rotation, the specific angular momentum is around 4×10^{-3} km s^{-1} pc. We can locate it at a specific angular momentum - rotation radius plot to compare with the other dense cores and protostars (e.g., Ohashi et al., 1997b; Belloche et al., 2002; Chen et al., 2007). Although as an infalling envelope at small scales, the large scale properties of the L1157 flattened envelope resemble those of prestellar cores more than those of more evolved protostars. Additionally, the fitted angular velocity implies that if the large-scale envelope collapses to form a circumstellar disk, the envelope material would fall onto the midplane within a centrifugal radius of $r_c = R^4\Omega^2/GM \approx 500$ AU. This radius is much larger than the observed T-Tauri disks. All above implies that the large-scale flattened envelope is probably not involved in the dynamical infall activity.

The interpretation of solid-body rotation is well suited from many theoretical points of view. For example, magnetic braking can induce solid-body rotation (Basu & Mouschovias, 1994). A turbulent core can also yield velocity gradient similar to uniform rotation (Burkert & Bodenheimer, 2000). Here we calculated the β_{rot} parameter, defined as the ratio of rotational kinetic energy to gravitational energy $\beta_{rot} = \frac{\frac{1}{2}I\Omega^2}{qGM^2/R} = \frac{p\Omega^2R^3}{2qGM}$, at different radii of the flattened envelope. (Note that this β_{rot} is different from the opacity spectral index mentioned in the previous sections.) For L1157, β_{rot} is smaller than 2% throughout the envelope, suggesting that the flattened structure is not supported by rotation.

The combined best-fit model of simple infall and solid-body rotation is shown by the black contours in Figure 2.9(c). Both the double-peaked feature and the large-scale velocity

gradient can be explained by this model. However, the asymmetric features are impossible to model with an axisymmetric model in the optically thin case. Local clumpiness can be the cause of asymmetry. Without further observations with higher spatial and spectral resolutions it is hard to justify the detailed properties.

2.4.6 Overall Gas-dust Comparison and Global Picture of L1157

By considering the dust and gas information of Class 0 YSO L1157 altogether, we are able to construct an overall physical picture of the system. The dust absorption at 8 μm from *Spitzer* shows a large-scale extended dense cloud that is flattened perpendicular to the outflow direction, while the 3 mm dust emission from CARMA D- and E-array shows a compact spherical structure. These two observations of dust detect different components of the envelope. The extended envelope detected by 8 μm absorption is likely part of the parent cloud, while the very inner region seen by our dust continuum is the collapsing envelope. The flattened geometry may result from physical processes of core formation. In the meantime, the N_2H^+ emission provides a consistent view both morphologically and kinematically. The N_2H^+ feature coincides with the extended dust absorption seen at 8 μm, implying that the same cloud component is observed. A slow solid-body rotation at large scales is seen along the major axis of elongation, but the flattened structure is not supported by rotation. This parent cloud resembles the physical properties of a prestellar core, while the innermost region is decoupled and undergoes (gravitational) collapse.

A similar dynamical scenario has also been suggested for another Class 0 object, IRAM 04191+1522 (Belloche et al., 2002). They have obtained a decoupling radius of $\sim$3500AU, which divides the envelope into a rapidly rotating inner region with free-fall motion and a transition region connected to the ambient slowly rotating cloud. Their estimated angular velocity at large scales ($\sim$1.9 km s^{-1} pc^{-1} at 7000 AU and $\lesssim$0.5-1 km s^{-1} pc^{-1} at 11000 AU) are comparable to what we find for L1157. More recent interferometric observations revealed faster rotation at smaller scales, but resolved out the large-scale structures (Belloche

& André, 2004; Lee et al., 2005).

We construct an edge-on disk-like envelope model that fits our L1157 data. Given the estimated column density and assumptions of envelope geometry, the volume density averaged along the line of sight can be estimated. With the assumption of an outer radius of 15,000AU and a constant N_2H^+ abundance of 3.0×10^{-10}, as used in our dust modeling, the average gas volume density ranges from $\sim2\times10^4$ to $\sim3\times10^5 cm^{-3}$. This volume density is consistent with the detectable density of N_2H^+, that is, it is close to the critical density $10^5 cm^{-3}$. On the other hand, the average density should not be higher than the depletion density ($\sim10^6$-10^7 cm^{-3}); this can give a constraint on the thickness of the cloud.

The geometric structures of L1157 at different sizescales are shown at various observations (Figure 2.10). At small scales, L1157 shows a nearly spherical morphology, as commonly seen in other YSOs (e.g., Looney et al., 2000; Shirley et al., 2000); detailed comparisons between observations and theories of collapsing envelopes are usually done assuming spherical symmetry (e.g., Looney et al., 2003). In particular, high resolution observations done by interferometry only show the contributions from the inner envelope while the large scale structures are mostly resolved out. Deviation from spherical symmetry can be significant, especially at large scales. At a younger stage of evolution, large scale dense cores are commonly observed to be elongated (e.g., Myers et al., 1991). Although the underlying dynamical processes of the flattened cores are controversial (e.g., Gammie et al., 2003; Tassis, 2007; Offner & Krumholz, 2009), non-spherical structure in the initial condition can play an important role for their evolution (e.g., Galli & Shu, 1993; Hartmann et al., 1996). For L1157, both the N_2H^+ feature and 8 μm absorption reveal the flattened structure at the size scale of $\sim$0.1 pc, comparable to a typical prestellar core. At a larger scale, the morphology becomes even more irregular. For example, the DSS (Digitized Sky Survey) [7] optical image of L1157 shows

[7]The Digitized Sky Survey was produced at the Space Telescope Science Institute under U.S. Government grant NAG W-2166. The images of these surveys are based on photographic data obtained using the Oschin Schmidt Telescope on Palomar Mountain and the UK Schmidt Telescope. The plates were processed into the present compressed digital form with the permission of these institutions.

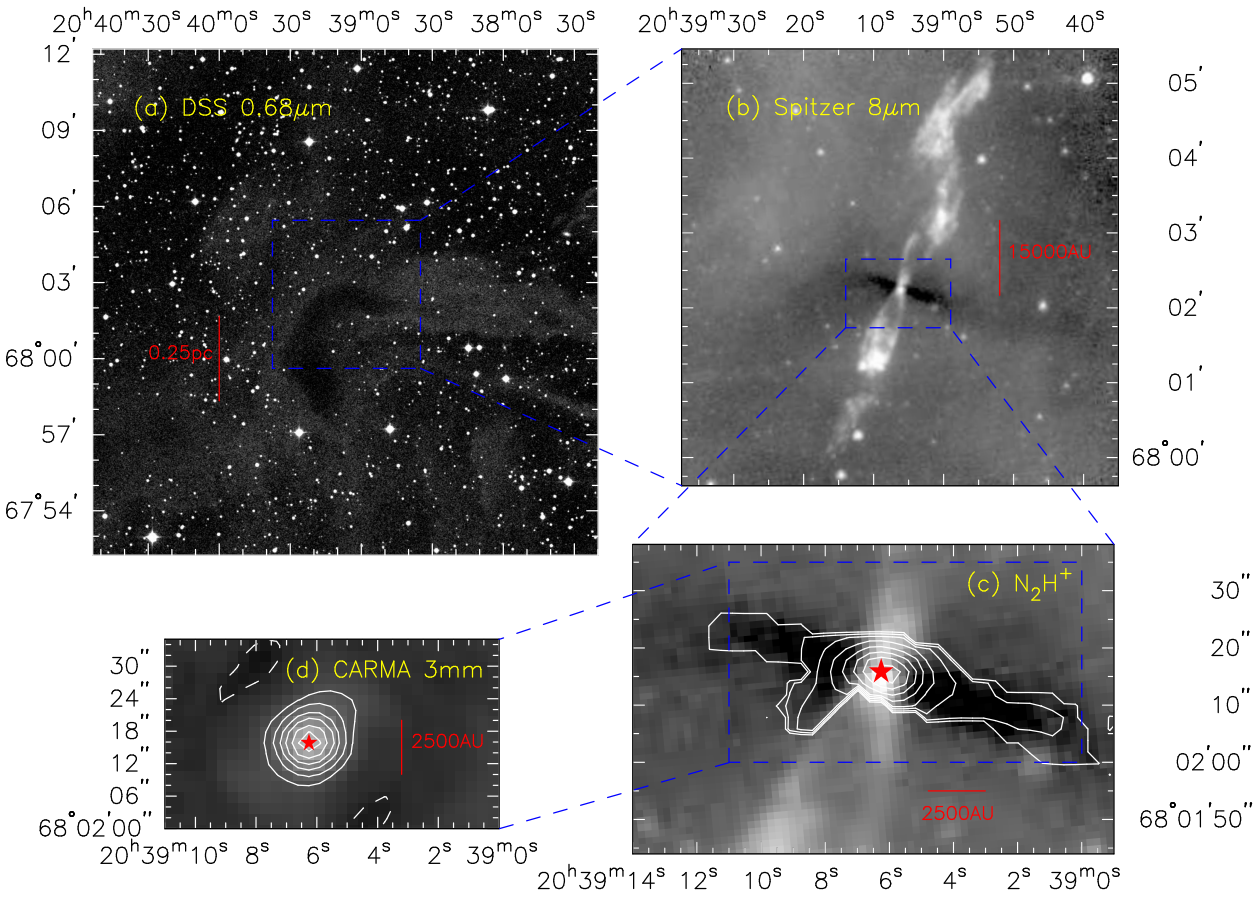

Figure 2.10 L1157 at different scales seen by various observations: (a) DSS optical image (b) *Spitzer* IRAC 8 μm image (c) zoomed-in 8 μm image overlaid with the N_2H^+ column density map (d) 3 mm dust continuum observed by CARMA. Different geometric characteristics are shown. The cloud is irregular at scale of $\sim$0.5 pc, flattened perpendicular to the outflows at scale of $\sim$15,000 AU, and nearly spherical at size scales smaller than $\sim$5,000 AU.

a large scale structure of irregular shape. This is more like the initial condition but not the consequence of star formation. The cloud is filament-like and irregular at very large scale, while a nearly spherical inner envelope is embedded in the intermediate-size, flattened outer envelope extended perpendicular to the outflows.

L1157 is an interesting and relatively simple case for early star formation. While many Class 0 YSOs are associated with large-scale non-axisymmetric outer envelopes, the geometry of L1157 is highly flattened and symmetric (Tobin et al., 2010b). L1157 is a perfect site for observational experiments, presenting a typical Class 0 YSO with less complexity. The properties of L1157 may be generalized to other Class 0 YSOs. For example, the Class 0

collapsing envelope with its embedded protostar is surrounded by the outer envelope left by its parent core that may or may not gravitationally collapse at a later time. In the case of L1157, we are able to detect this outer envelope in a flattened structure at both 8 μm and N_2H^+ emission, revealing a phase that shows both properties of the preceding prestellar core stage at large scale and properties of the current Class 0 stage at small scale. In other cases, the outer envelope can become more complicated that a non-axisymmetric model will be needed to interpret the observations.

2.5 Summary

1. We observed the dust continuum and N_2H^+ gas emission at 3 mm toward the Class 0 YSO L1157 IRS with an angular resolution of $\sim 7''$ using CARMA at D- and E-array. Spectra of the N_2H^+ isolated component JF_1F=101-012 were obtained with resolution of $\sim$0.1 km s^{-1}. While the 3 mm dust continuum detects the inner envelope, which is compact and nearly spherical, the N_2H^+ emission shows a huge flattened structure with a linear size of $\sim$20,000AU, coinciding with the disk-like feature found by the 8 μm absorption in Looney et al. (2007).

2. By fitting the spectra, we estimated the gas column density across the flattened envelope and compared with the dust column density deduced from the 8 μm absorption feature. We derived the N_2H^+ abundance and found results consistent with what is expected from chemical models. Further, we examined the radial profile of N_2H^+ abundance along the major axis of the flattened envelope, and showed the asymmetry between the east and west extention.

3. We constructed a simple flattened envelope model that fits the compact dust continuum; further, the model-expected gas column density is consistent with the extended N_2H^+ emission. It follows that the deviation from spherical symmetry can be impor-

tant at large scales for protostellar envelopes. However, this model is not motivated by a theoretical model.

4. We did Position-Velocity contour modeling and studied the kinematics of the N_2H^+ feature. The spectrum of the central part of the system shows a double peaked feature, implying infall. The large-scale component can be described by slow solid-body rotation comparable to the properties of a typical prestellar core. This large-scale filament may arguably result from the dynamical processes in the early core formation, while only the very inner part is actively involved in the protostar formation.

2.6 Supplement: Molecular Column Density Estimation

This appendix summarizes the derivation of the equations used to estimate the molecular column density with interferometric data. With the Planck's function

$$B_\nu = \frac{2h\nu^3}{c^2}\frac{1}{e^{\frac{h\nu}{kT}}-1} \tag{2.8}$$

and assuming the level population is in the local thermodynamic equilibrium (LTE) limit with the Boltzmann distribution, the absorption coefficient κ_ν can be written as

$$\kappa_\nu = \frac{c^2 A_{ul}}{8\pi\nu^2} N_u \left(e^{\frac{E_{ul}}{kT_{ex}}}-1\right)\phi(\nu), \tag{2.9}$$

where A_{ul} is the Einstein A coefficient, N_u is the number density in the upper state, E_{ul} is the energy of the transition, T_{ex} is the excitation temperature characterizing the population between the states, and $\phi(\nu)$ is the line profile that satisfies $\int \phi(\nu)d\nu = 1$. In the LTE limit,

the relation between N_u and the total number density is

$$\frac{N_u}{N_{tot}} = \frac{g_u}{Q(T_{ex})} e^{-\frac{E_u}{kT_{ex}}}. \tag{2.10}$$

Considering a transition between level u and level l with energy difference of $h\nu_0$, the absorption coefficient can be written as

$$\kappa_\nu = \frac{h\nu_0}{c} N_l B_{lu} \left(1 - \frac{g_l N_u}{g_u N_l}\right) \phi(\nu), \tag{2.11}$$

where N_u and N_l are the number density of the states, g_u and g_l are the statistical weights of the states, $\phi(\nu)$ is the line profile, and B_{lu} is the Einstein B coefficient. Replacing the Einstein B coefficient by the Einstein A coefficient with the relationship

$$B_{lu} = \frac{g_u}{g_l} A_{ul} \frac{c^3}{8\pi h\nu^3}, \tag{2.12}$$

where the Einstein A coefficient can be expressed as

$$A_{ul} = \frac{64\pi^4 \nu^3 \mu^2}{3hc^3} \frac{g_l}{g_u}, \tag{2.13}$$

(μ is the dipole moment) and also using Boltzmann distribution for the energy level population

$$\frac{N_u}{N_l} = \frac{g_u}{g_l} e^{-\frac{h\nu_0}{kT_{ex}}} \tag{2.14}$$

based on the assumption of LTE, Eq. (2.11) becomes

$$\kappa_\nu = \frac{c^2 A_{ul}}{8\pi\nu^2} \frac{g_u}{g_l} N_l \left(1 - e^{-\frac{h\nu_0}{kT}}\right) \phi(\nu) = \frac{c^2 A_{ul}}{8\pi\nu^2} N_u \left(e^{\frac{h\nu_0}{kT}} - 1\right) \phi(\nu), \tag{2.15}$$

where T_{ex} is the excitation temperature characterizing the population between the states.

Integrating over frequency space with $\int \phi(\nu)d\nu = 1$, we get

$$N_u = \frac{8\pi\nu^2}{c^2 A_{ul}} \frac{1}{\left(e^{\frac{h\nu_0}{kT}} - 1\right)} \int \kappa_\nu d\nu \tag{2.16}$$

With Eq. (2.10) based on the LTE assumption, we obtain the total number density

$$N_{tot} = \frac{8\pi\nu^2}{c^2 A_{ul}} \frac{Q(T_{ex})}{g_u} \frac{1}{\left(1 - e^{-\frac{h\nu_0}{kT}}\right)} \int \kappa_\nu d\nu. \tag{2.17}$$

By integrating the total number density along a line of sight ($\tau = \kappa ds$), the column density is

$$\mathcal{N}_{tot} = \frac{8\pi\nu^2}{c^2 A_{ul}} \frac{Q(T_{ex})}{g_u} \frac{1}{\left(1 - e^{-\frac{h\nu_0}{kT}}\right)} \int \tau_\nu d\nu, \tag{2.18}$$

where $Q(T_{ex})$ is the partition function

$$Q_{rot}(T_{ex}) = \sum_{J=0}^{\infty} (2J+1) e^{-\frac{E_J}{kT}}. \tag{2.19}$$

For linear molecules, the energy is

$$E_J = J(J+1)hB, \tag{2.20}$$

where J is the rotational quantum number and B is the rotational constant. In the limit that $hB \ll kT$, the partition function for a linear molecule becomes

$$Q_{linear}(T_{ex}) = \sum_{J=0}^{\infty} (2J+1) e^{-J(J+1)\frac{hB}{kT}} \overset{u \equiv J(J+1); du = (2J+1)dJ}{\longrightarrow} \int_0^{\infty} e^{-\frac{hB}{kT}u} du \approx \frac{kT}{hB} \tag{2.21}$$

$$Q_{linear}(T_{ex}) \approx \frac{kT}{hB} \tag{2.22}$$

For symmetric top or asymmetric top molecules, the partition function is

$$Q_{(a)sym}(T_{ex}) \approx \sqrt{\frac{\pi}{ABC}\left(\frac{kT}{h}\right)^3}, \tag{2.23}$$

where A, B, and C are rotational constants along different axes.

With the radiative transfer equation,

$$I_\nu = (B_\nu(T) - I_\nu(T_{bg}))(1 - e^{-\tau_\nu}), \tag{2.24}$$

we obtain

$$\frac{c^2}{2k\nu^2} I_\nu = T_B(\nu) = \frac{h\nu}{k}\left(\frac{1}{e^{\frac{h\nu}{kT_{ex}}} - 1} - \frac{1}{e^{\frac{h\nu}{kT_{bg}}} - 1}\right)(1 - e^{-\tau_\nu}) = (J(T_{ex}) - J(T_{bg}))(1 - e^{-\tau_\nu}), \tag{2.25}$$

where the equivalent Rayleight-Jeans temperature is given by

$$J(T) \equiv \frac{h\nu}{k}\frac{1}{e^{\frac{h\nu}{kT}} - 1}, \tag{2.26}$$

By rearranging Eq. (2.25), we obtain

$$\tau = -ln\left(1 - \frac{T_B}{J(T_{ex}) - J(T_{bg})}\right). \tag{2.27}$$

In the optically thin limit,

$$\tau_\nu = \frac{I_\nu}{(B_\nu(T) - I_{bg})} C_\tau, \tag{2.28}$$

where C_τ is the opacity correction factor

$$C_\tau = \frac{\tau}{1 - e^{-\tau}}. \tag{2.29}$$

Integrating both sides of Eq. (2.28), we obtain

$$\int \tau_\nu d\nu \approx \frac{1}{(B_\nu(T) - I_{bg})} C_\tau \int I_\nu d\nu. \tag{2.30}$$

And the column density from Eq. (2.18) becomes

$$\mathcal{N}_{tot} = \frac{8\pi\nu^2}{c^2 A_{ul}} \frac{Q(T_{ex})}{g_u} \frac{1}{\left(1 - e^{-\frac{E_u}{kT}}\right)} \frac{1}{(B_\nu(T) - I_{bg})} C_\tau \int I_\nu d\nu \tag{2.31}$$

Using Eq. (2.8), Eq. (2.13) and $d\nu = \frac{\nu}{c} dv$, we rewrite the column density

$$\mathcal{N}_{tot} = \frac{3c^2}{16\pi^3} \frac{Q(T_{ex}) e^{\frac{E_u}{kT}}}{\nu^3 \mu^2 g_l} \frac{B_\nu(T_{ex})}{B_\nu(T) - I_{bg}} C_\tau \int I_v dv. \tag{2.32}$$

By plugging in unit conversion between cgs and conventional units of interferometric observations, it becomes

$$\mathcal{N}_{tot}(cm^{-2}) = 2.04 \times 10^{20} \frac{1}{\theta_a \theta_b} \frac{Q(T_{ex}) e^{\frac{E_u}{kT}}}{\nu(GHz)^3 \mu(debye)^2 g_l} \frac{B_\nu(T_{ex})}{B_\nu(T) - I_{bg}} C_\tau \int I_v(Jy/beam) dv(km/s), \tag{2.33}$$

where g_l is also known as the line strength S, θ_a and θ_b are observational beamsizes, and a background intensity correction with $T_{bg} = 2.73$K is usually used. The excitation temperature T_{ex} and opacity τ can be estimated by fitting observational spectrum, which will be discussed in the next section.

2.7 Supplement: Hyperfine Spectrum Fitting

Spectrum fitting of N_2H^+ is performed for pixels with more than 3 S/N detection on the integrated intensity map and a MATLAB routine is constructed to fit hyperfine lines with Gaussians. Assumptions include:

- Same excitation temperature T_{ex} for all hyperfine components

- The opacity of the components are Gaussians in frequency space

- A constant proportionality for each hyperfine comoponent

- All components have the same linewidth

There are 4 parameters in the spectrum fitting:

- $\mathbb{P}1 = B(T_{ex})$,

- $\mathbb{P}2 = v_{LSR}$,

- $\mathbb{P}3 = \Delta v$ (FWHM of the velocity dispersion), and

- $\mathbb{P}4 = \tau_{tot} = \sum_{i=1}^{7} \tau_i$.

In cases of insufficient signal-to-noise, $\mathbb{P}1$ and $\mathbb{P}4$ can be somewhat dependent. Alternatively, $\mathbb{P}1$ can be dropped and the number of parameters is reduced to three with the assumption of a constant T_{ex}. The opacity can be expressed as

$$\tau(\nu) = \sum_{i=1}^{7} \tau_i \exp\left(-4ln2(\frac{v - v_{0,i} - v_{LSR}}{\Delta v})^2\right) \tag{2.34}$$

or

$$\tau(\nu) = \mathbb{P}4 \sum_{i=1}^{7} r_i \exp\left(-4ln2(\frac{v - v_{0,i} - \mathbb{P}2}{\mathbb{P}3})^2\right), \tag{2.35}$$

where r_i is the relative strength of each hyperfine component satisfying $\tau_i = r_i \tau_{tot}$ and $\sum_{i=1}^{7} r_i = 1$.

From Eq. (2.24),

$$I_\nu = \mathbb{P}1(1 - e^{-\tau_\nu}), \tag{2.36}$$

and using the Planck function Eq. (2.8) and Eq. (2.24),

$$\mathbb{P}1 = I_\nu = \frac{2k\nu^2}{c^2}(J(T_{ex}) - J(T_{bg})) = \frac{2h\nu^3}{c^2}\left(\frac{1}{e^{\frac{h\nu}{kT_{ex}}} - 1} - \frac{1}{e^{\frac{h\nu}{kT_{bg}}} - 1}\right). \tag{2.37}$$

The excitation temperature is

$$T_{ex} = \frac{h\nu}{k} \frac{1}{ln\left(1 + \frac{1}{\frac{\mathbb{P}1c^2}{2h\nu^3} + \frac{1}{e^{\frac{h\nu}{kT_{bg}}} - 1}}\right)} \tag{2.38}$$

which can be simplified as

$$T_{ex} - T_{bg} \approx \frac{h\nu}{k} \frac{1}{ln(1 + \frac{2h\nu^3}{\mathbb{P}1c^2})} \tag{2.39}$$

given the assumption that the T_{MB} is well suited, that is, in the Rayleigh Jeans regime.

The MATLAB nonlinear least-squares regression function *nlinfit* is used to compute the best fit and uncertainty of the fits are reported.

Chapter 3

Constraining the Earliest Circumstellar Disks and their Envelopes: I. 1D Approximation

This chapter is previously published in The Astrophysical Journal as "Constraining the Earliest Circumstellar Disks and their Envelopes", Chiang, H.-F., Looney, L. W., Tassis, K., Mundy, L. G., & Mouschovias, T. Ch. 2008, ApJ, 680, 474 and is reproduced here with permission of the American Astronomical Society.

Using interferometric data from BIMA observations, combined with detailed modeling in Fourier space of the physical structures predicted by models, we constrain the circumstellar envelope parameters for four Class 0 young stellar objects, as well as their embedded circumstellar disks. The envelopes of these objects are still undergoing collapse, and theoretical collapse models can be compared to the observations. Since it has been suggested in a previous study that both the Larson-Penston and Shu similarity solutions underestimate the age of the system, we adopt Tassis & Mouschovias' model of the collapse process, which includes all relevant magnetic fields effects. The results of the model fitting show a good consistency between theory and data; furthermore, no age problem exists since the Tassis & Mouschovias' model is age independent for the first 255 kyr. Although the majority of the continuum dust emission arises from the circumstellar envelopes, these objects have well known outflows, which suggest the presence of circumstellar disks. At the highest resolution, most of the large-scale envelope emission is resolved out by interferometry, but the small-scale residual emission remains, making it difficult to observe only the compact disk component. By modeling the emission of the envelope and subtracting it from the total emission, we constrain the disk masses in our four systems to be comparable to or smaller than the typical disk masses for T Tauri systems.

3.1 Introduction

The standard scenario of low-mass star formation starts at the collapse of prestellar cores and the formation of central protostellar objects. These young stellar objects (YSOs) evolve through the so-called Class 0, I, II, and III stages, which are thought to be a temporal sequence (e.g., Lada & Wilking, 1984; Adams et al., 1987; Andre et al., 1993, 2000). In the earliest stage, i.e. Class 0 stage, when the central YSO is just forming inside the surrounding envelope (of mass $\approx$ a few solar masses, e.g., Looney et al., 2000), the envelope is still undergoing gravitational collapse onto the circumstellar disk. The YSO powers the bipolar outflows, which carve away the polar region of the envelope by entraining envelope material and widening their opening angles (e.g., Bachiller, 1996; Arce & Sargent, 2006; Seale & Looney, 2008). At this early time, the envelope mass is >85% of the system mass (Looney et al., 2003). As the system evolves, the envelope loses mass as material is transported down through the circumstellar disk onto the protostars or carried away with the outflows. Eventually, the YSO circumstellar structure is dominated by the disk (a hundredth of a solar mass, e.g., Andrews & Williams 2005). The circumstellar disk evolves, presumably becoming a planetary system like the Solar System.

The initial collapse process of low-mass protostars is often described by self-similar isothermal solutions, which are a continuum of solutions (e.g., Whitworth & Summers, 1985) that range from the "inside-out" collapse solution (Shu, 1977, hereafter the Shu solution) to the Larson-Penston solution (Larson, 1969; Penston, 1969; Hunter, 1977, hereafter the LP solution). These models generally obtain an inner core with a power law density profile $\rho \propto r^{-3/2}$ that increases in radius with time, surrounded by a $\rho \propto r^{-2}$ envelope. The theoretical density profiles from these solutions have been compared to observations of the dust continuum emission (Looney et al., 2003; Harvey et al., 2003; Jørgensen et al., 2005), but the models cannot fit the observations with reasonable physical parameters (required age is too low; see Looney et al. 2003), which consequently hints at the need for more sophisti-

cated theoretical models that include more of the essential physical processes of the collapse mechanisms, for example, turbulence and/or magnetic fields.

The theory of turbulence-induced star formation postulates that turbulence causes overdensities and is thus responsible for the core formation in molecular clouds, while magnetic fields are not dynamically important and do not have a significant impact on this process (see reviews of Mac Low & Klessen, 2004; Elmegreen & Scalo, 2004). At this time, there are no predictions of the density of a protostellar object that is produced by turbulence-induced collapse. Moreover, the non-thermal contribution of the observed linewidths is small in evolved, collapsing molecular cloud cores (e.g., Benson & Myers, 1989; Barranco & Goodman, 1998; Kirk et al., 2007). Whether turbulence plays an important role in the formation and evolution of protostellar fragments (or cores) is still under debate. On the other hand, the theory of ambipolar-diffusion-initiated star formation predicts the formation of thermally and magnetically supercritical protostellar cores inside magnetically subcritical parent clouds (see reviews of Mouschovias, 1996; Mouschovias & Ciolek, 1999). In the framework of the ambipolar-diffusion-induced collapse, there are extensive studies of the dynamics of the prestellar phase (e.g., Tassis & Mouschovias, 2007a,b,c) and the accretion process after a protostar has formed at the center of the core (Tassis & Mouschovias, 2005a,b, hereafter TM2005), which can be compared to observations.

TM2005 have constructed a six-fluid MHD simulation to study the accretion process of matter from a molecular cloud core onto a protostellar object in the presence of magnetic fields. In their model, they track the evolution of magnetic flux and six kinds of particles (neutral molecules, atomic and molecular ions, electrons, neutral grains, negatively-charged grains, and positively-charged grains, among which only the electrons are assumed to be attached to the magnetic field lines) in a self-gravitating, accreting molecular cloud core. The simulation starts with a magnetically supported parent cloud. Ambipolar diffusion leads to the formation of a thermally and magnetically supercritical core that begins to contract dynamically. Its innermost part reaches nearly hydrostatic equilibrium while its

outer part still undergoes infall. At the moment when the hydrostatic protostellar core has just formed at the center (called $t = 0$), the inner core region including the protostar is replaced by a central sink to facilitate the calculation. As time progresses and mass and magnetic flux accrete onto the protostar from the envelope, a region of enhanced magnetic field, called the "magnetic wall", forms and drives an outward-propagating shock. Behind the shock, gravity dominates over the magnetic forces and reaccelerates the neutral particles, which continue to accrete onto the protostar until the next magnetic wall is formed. The magnetic wall forms and disperses in a quasi-periodic manner. Because of the presence of the magnetically controlled bursts, accretion from the envelope onto the protostar is episodic over the first 255 kyr.

Interferometric data of Class 0 objects provide the best means to test these theories. One of the features of an interferometer is the ability to spatially filter emission. Indeed, dust continuum observations of young protostars have been often used to peer inside the bright envelope to reveal the young, compact circumstellar disk (e.g., Keene & Masson, 1990). Dust continuum emission is often used, but molecular lines can also be excellent tracers of specific conditions. However, using molecular lines to trace the disks do have some difficulties in the case of the youngest stars: (1) active accretion and outflow processes at multiple scales, (2) chemistry effects and evolution, and (3) shocks in the outflow, the disk, and the disk/envelope interface region. All of these contaminate the preferred disk-only tracers and make it difficult to disentangle any molecular result without a good understanding of the envelope structure derived from the dust continuum modeling (e.g., Brinch et al., 2007).

Regardless of the tracers used, more intricate theoretical models than the "inside-out" collapse can be tested observationally. In this paper, we build on the observational data of Looney et al. (2000): $\lambda = 2.7$ mm dust continuum images of 24 young stellar sources with sensitivity to spatial scales from $0\farcs5$ to $50''$. A discussion of the data acquisition and images can be found in that paper. We follow the work of Looney et al. (2003), which presented modeling of the envelope emission of Class 0 objects, and use the 4 sources from that work

with the highest signal-to-noise ratio (NGC 1333 IRAS 4A, NGC 1333 IRAS 4B, NGC 1333 IRAS 2A, and L1448 IRS 3B). We compare the predicted density profiles from TM2005 to these data and comment on the results with respect to those found in Looney et al. (2003).

3.2 Sources

All 4 sources modeled in this study are in the Perseus molecular cloud, a low mass star forming region probably in the vicinity of the massive star forming region Per OB2 association. Dense cores and YSO candidates at all evolutionary stages have been found in Perseus via radio and infrared observations. IC 348 and NGC 1333 are the two main dense clusters and other smaller groups like L1448, L1455, Barnard 1, and Barnard 5 are also associated with many low mass protostars (e.g. Enoch et al., 2006; Jørgensen et al., 2006). The exact distance to the Perseus molecular cloud is still uncertain and ranges from 220 to 350 pc. The smaller value is based on the distance-interstellar extinction relation using photometry (Cernis, 1990); the distance may be the larger value if the Perseus molecular cloud is physically related to the Per OB2 association, Hipparcos parallax distance of 318 $\pm$ 27 pc (de Zeeuw et al., 1999). Since Perseus is composed of a long chain of dense clouds with a total length of about 30 pc, there may be a distance gradient or it may be composed of several layers of clouds. Cernis (1993) showed a distance difference from the eastern part ($\sim$260 pc) to the western part ($\sim$220 pc). In this study, we adopt a distance of 350 pc for NGC 1333 and 300 pc for L1448 as in Looney et al. (2003) to facilitate comparison. Since we are using roughly the upper limit of the distance, this assumption may lead to overestimates of the envelope and disk masses and underestimates of the source size.

3.2.1 NGC 1333 IRAS 4

NGC 1333 is a reflection nebula with mainly two embedded protostellar clusters in the L1450 dark nebula in the Perseus molecular cloud. The age of the young cluster is about 1

Myr, estimated by the fraction of infrared excess sources and a K-band luminosity function comparison (Lada et al., 1996), consistent with the age estimated by brown dwarf studies (e.g. Wilking et al., 2004). The plentiful jet and outflow activities driven by YSOs in this region also imply that it is an active star forming region at an early stage of evolution (e.g., Bally et al., 1996; Knee & Sandell, 2000).

The multiple system NGC 1333 IRAS 4 (hereafter IRAS 4) contains mainly three groups of sources designated as 4A, 4B, and 4C (Sandell & Knee, 2001). The brightest Class 0 component IRAS 4A has been detected as a binary system separated by 1.8″ with a common circumbinary envelope (Lay et al., 1995; Looney et al., 2000). A highly collimated N-S molecular outflow driven by IRAS 4A2 has been observed with estimated dynamical age of about 6000 yr (Blake et al., 1995; Choi, 2005). A dimmer southern outflow probably driven by 4A1 has been mapped in HCN and SiO, but no northern counterpart has been detected (Choi, 2001, 2005). SMA polarimetric observations have shown the magnetic field geometry of IRAS 4A and supported the magnetic theory of star formation (Girart et al., 2006).

IRAS 4B is a binary system with a separation of ∼10″ between 4BW and 4BE (Sandell & Knee, 2001); 4BE is also named as 4B', 4BII, or 4C in different references. Note that 4C is mostly used as the name of another millimeter object ∼50″ northeast of 4A. A compact collimated outflow driven by IRAS 4BW has been observed (e.g., Choi, 2001; Di Francesco et al., 2001) and shown a short dynamical timescale.

3.2.2 NGC 1333 IRAS 2A

NGC 1333 IRAS 2 (hereafter IRAS 2) has been resolved into 3 sources (Sandell & Knee, 2001) including two Class 0 protostars, IRAS 2A and IRAS 2B, and a starless core IRAS 2C (Jørgensen et al., 2004a). Two CO outflows have been mapped: one in the NNE-SSW direction and the other in the E-W direction (e.g., Knee & Sandell, 2000). Since these two outflows are orthogonal to each other and have quite different properties, they may have different driving sources. The E-W outflow may be driven by IRAS 2A, while the NNE-SSW

outflow may be driven by IRAS 2C (Knee & Sandell, 2000). It's also possible that both are driven by IRAS 2A which may be an unresolved binary. IRAS 2B may drive the third outflow in this region but only the blue-shifted lobe has been identified (Knee & Sandell, 2000).

3.2.3 L1448 IRS 3B

The star forming region L1448 is located $\sim 1^\circ$ southwest of NGC 1333 in Perseus and contains many YSOs: Class I source L1448 IRS 1, Class 0 sources L1448 IRS 2, L1448 IRS 3 (also known as L1448 N), and L1448-mm (also know as L1448 C) are the most well-known (e.g. Jørgensen et al., 2006; O'Linger et al., 2006). Many of these YSOs have been resolved into binary systems; for example, L1448 IRS 3 and L1448-mm are both binary systems. Multiple outflows have been found in this region. The huge molecular outflows emanating from L1448-mm and L1448 IRS 2 are almost parallel to each other, and some of them even have multiple overlapping components (e.g. Wolf-Chase et al., 2000; Kwon et al., 2006; Tobin et al., 2007).

L1448 IRS 3 is composed of 3 sources, among which IRS 3A (L1448 N:A) and IRS 3B (L1448 N:B) are separated by $7''$ and have a common envelope in a protobinary system, and IRS 3C (L1448 NW) is $20''$ northwest of them (Looney et al. 2000). All of them are Class 0 objects, except that IRS 3A is slightly closer to the transition between Class 0 and Class I (O'Linger et al., 2006). Two interacting outflows driven by IRS 3A and IRS 3B, respectively, have been studied by Kwon et al. (2006).

3.3 Modeling

To compare the theoretical models of TM2005 and the observations in Looney et al. (2000), we characterize the observed dust continuum emission, which depends on the dust density, grain properties, and temperature.

3.3.1 Density Profiles

In the theoretical TM2005 model, the physical parameters of the envelope are shown to have a quasi-periodic variation beginning at the time of about 15 kyr after the formation of a hydrostatic protostellar core. The density goes through a cycle profile that is largely invariant with time from 15 to 255 kyr. This implies that, unlike the LP or Shu models, we cannot estimate the age of the source based on its density profile alone.

In this study, we adopt a typical set of density profiles, averaged along the characteristic scale height, from one of the magnetic cycles predicted by the TM2005 model. The density structure repeatedly goes through phase $\phi = 1$ to 15 in an evolution cycle, as shown by the solid curves in Figure 3.1. Here we only plot the more representative phases. The dotted curve in Figure 3.1 shows the initial density profile at the time hydrostatic equilibrium is established in the central region of the core ($t = 0$), which nearly follows a power-law relation of index -1.7. We can choose density profiles of any cycle for this study, as they are all similar. In other words, different cycles have the same predicted density profiles and quantitatively similar phases. The age of the chosen magnetic cycle is from $t = 33{,}750$ to 37,250 yr after the formation of the central hydrostatic core. By this time, the series of magnetic cycles has been well established.

The model cloud in TM2005 has an equatorial radius of 4.23 pc. However, the thermally and magnetically supercritical fragment extends to approximately 9000 AU and contains $\sim$9 $M_\odot$. Outside this region, hardly any evolution takes place (see Figure 3.1). In order to compare with observations, we truncate the density profiles at an outer radius within which the dynamical infall takes place. This is the "envelope", at the center of which the protostar is forming. By scaling the density profiles, the theoretical TM2005 model is applied to observed objects of different masses. (This kind of scaling of the density profiles implies a corresponding scaling of the magnetic field profiles, but, since no information on the magnetic field is available from observations, we do not discuss this implication further in this paper.)

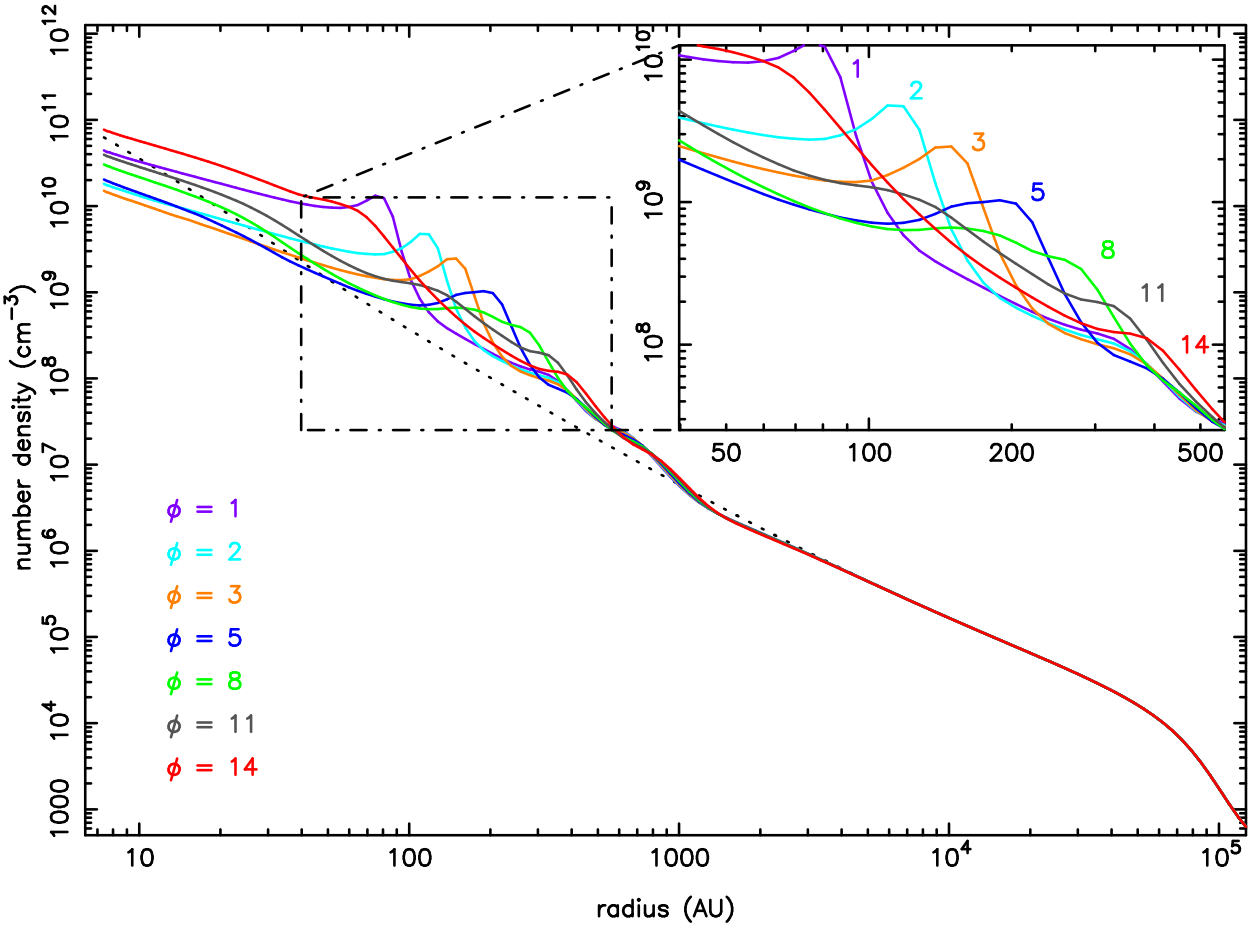

Figure 3.1 The number density profiles of neutral particles in a typical magnetic cycle at different phases from the TM2005 model. These curves show phase 1, 2, 3, 5, 8, 11, and 14, which correspond to t = 33750, 34000, 34250, 34750, 35500, 36250, and 37000 yr after formation of the central protostar. The shock driven by the "magnetic wall" forms, propagates outward, and disperses throughout a cycle. Although this is a particular cycle, no obvious differences are found between cycles, that is, every magnetic cycle goes through similar phases, except that the period of the cycle varies as the system evolves (see TM2005a,b for more details).

Although the TM2005 model has a flattened morphology (Fiedler & Mouschovias, 1993), we only use a spherical density profile in this study. The flattened molecular cloud has a radius of several pc, which is much larger than the scale studied here. Looney et al. (2003) has tested geometric effects by elongating the envelope, and shown that flattening the envelope will artificially make a steeper flux density profile in u-v space. However, the analysis normalized the maximum flux density, which is different than the effect studied here. To better compare the effect a flattened envelope has on our modeling, we modified our spherical envelope model by multiplying the predicted image with a flat-shaped mask with exponentially-decayed edges similar to a flattened envelope. The half-thickness of the "disk" is one-fifth of the radius, which gives a similar flattening ratio to that in the TM2005 model. In this case, the observed flux density is less steep at small u-v distances, but is unchanged beyond u-v distances of 10 $k\lambda$. This is because fewer large-scale components, or small u-v distance components, contribute in the flattened structure compared to a spherical model. We fit the simulated data of a flattened envelope with our spherical model and found that the spherical model fits the data very well with the same density profile, but that the mass is overestimated. In addition, the density profile from TM2005 has been averaged along the characteristic scale height, which also helps mitigate the effect of a flattened envelope. On the other hand, the vertical density profile needs to be better modeled (see the observed flattened envelope in Looney et al., 2007), which is beyond the scope of this paper. Finally, a circumstellar disk may exist inside the envelope and its emission is also taken into account in the model; this is described in more detail in § 3.4 and § 4 .

3.3.2 Grain Properties and Temperature Profiles

Properties of dust grains such as composition and size determine their extinction and emission, as well as the temperature structure and the observable dust emission of the envelope. Here we adopt the grain model of Wolfire & Cassinelli (1986), in which the material mixture and size distributions of the Mathis-Rumpl-Nordsieck model (Mathis, Rumpl, & Nordsieck,

1977, hereafter called the MRN model) and optical constants of grains in Draine & Lee (1984) are used. The grain model consists a mixture of uncoated graphite and silicate with particle sizes ranging from 0.005 μm to 0.25 μm and a power law size distribution of index -3.5. It is important to note that the grains in TM2005 are spherical and uniform in size with a different chemical composition from MRN. However, these grain differences are not significant in the theoretical model evolution (Desch & Mouschovias, 2001).

The mass opacity coefficient κ_ν of the grain is frequency dependent and typically follows a power law relation $\kappa_\nu \propto \nu^\beta$. The index β varies with environment and is related to grain properties. At submillimeter wavelengths, the unevolved grains of the ISM have $\beta \approx 2$. However, in disks and dense cores β decreases to 1 mainly due to grain growth (e.g. Beckwith & Sargent, 1991; Natta et al., 2007). Although our observations are only at a single wavelength, κ_ν of a wider range of frequency is still needed for computing a self-consistent temperature profile since radiation of all frequencies contributes to the total luminosity. Our model uses the MRN grain model $\beta = 2$ at optical and infrared wavelengths but assumes $\beta = 1$ at long wavelengths, and adopts $\kappa_\nu = 0.009\ cm^2\ g^{-1}$ at $\lambda = 2.7$ mm. The model also assumes the dust grain properties are uniform and do not change with radius in the envelope.

Temperature profiles are then considered based on the model grain properties. The temperature profile can be simplified as a power law with radius if the dust envelope is optically thin and the dust opacity has a power-law frequency dependence ($\kappa_\nu \propto \nu^\beta$): temperature $T \propto r^{-2/(4+\beta)}$ assuming the central protostar is the only heating source. In the case of $\beta = 1$, the temperature is $T \propto r^{-0.4}$. But in our model, the inner part becomes optically thick as the density increases near the center (Looney et al. 2003), so we calculate a self-consistent temperature profile for each fitting using the code of Wolfire & Cassinelli (1986). The code takes the luminosity of the central object and solves the radiative transfer equation including the effects of both emission and extinction by the dust grains in the envelope. At each shell of the envelope, the luminosity is conserved.

The self-consistent temperature profiles are important for calculating the emission, but they contradict the isothermal assumptions in theoretical models. However, until non-isothermal theoretical models are developed, this is the best compromise (also see Looney et al. 2003).

3.3.3 Interferometric Filtering

Although we use the power of the interferometer to resolve out the large-scale features of the envelope, it is important to point out that there is remnant envelope emission even with high resolution configurations (e.g., Looney et al. 2000). There are a few reasons for this. First, the envelope emission is power-law like (e.g., Looney et al. 2003), so the expected interferometric response from a Gaussian (Wilner & Welch, 1994) is not applicable. Second, the inner edge cutoff is abrupt, especially with the steep density profile. The abruptness causes ripples in u-v space that create power at long baselines. The important point here is that the ability to detect a disk in the presence of an envelope is not set by the formal noise level or Fourier components, but by the intrinsic ability to model the complexity of the envelope (inner cutoff, asymmetric structure, etc.) and the resolution of the observations compared to the disk size and the inner cutoff of the envelope. In other words, it is difficult to separate the youngest circumstellar disk from the inner circumstellar envelope; revealing the embedded circumstellar disk still requires an understanding of the inner envelope.

Only interferometric data are used in this study. Single dish data can give an upper limit at zero-spacings, but should not be included in the fitting. Single dish observations detect not only the emission from the inner envelope, but also that from the outer part of a cloud that is not actively involved in the protostar forming process. Using interferometry, only structures of size scale similar or smaller than the collapsing envelope are detected and modeled. Hence the mass and radius we are inferring in this paper are not the total mass or the overall size of the prestellar cores, but that of the inner envelope undergoing the collapse, observed at $\lambda = 2.7$ mm.

3.3.4 Modeling Details

The observational data we use are from Looney et al. (2000). To compare the observations and the theoretical model, we analyze the data in u-v space where the data are not affected by the CLEAN algorithm or u-v sampling. The interferometric data are binned in u-v annuli around the source locations from Looney et al. (2000) and averaged vectorially. The resulting u-v amplitudes for each bin are shown by asterisks in Figure 3.2. The displayed error bars are statistical error bars based on the standard deviation of the mean of the data points in the bin with a minimum of 10%, reflecting the uncertainty in the overall calibration. In the cases where the binary systems were separated by more than $10''$, the companion sources were subtracted out of the u-v data using the large-scale images of Looney et al. (2000). The new u-v data were remapped to confirm that the large-scale emission from the companion sources was not detected. Although there may exist some residual of small-scale emission from the companion envelope in the u-v data, vector averaging in u-v annuli will minimize its contribution.

The observational data shown in Figure 3.2 show the brightness distribution plotted at various antennas, or u-v, spacings, which is the Fourier transform of the sky brightness distribution. In other words, power at small u-v distance represents large-scale structures and power at large u-v distance represents small-scale structures, i.e., a point source would be a constant at all antenna separations. The brightness distribution is determined by the circumstellar material surrounding the source depending on density, temperature and grain properties.

We model the circumstellar envelope emission as arising from a spherically symmetric dust envelope with TM2005 radial density and self-consistent temperature profiles and an embedded circumstellar disk represented by an envelope-attenuated point source. The observed emission of most sources shows a circular symmetry and lack of significant internal structures (see images of the sources in Looney et al. 2000). The combined radiative transfer

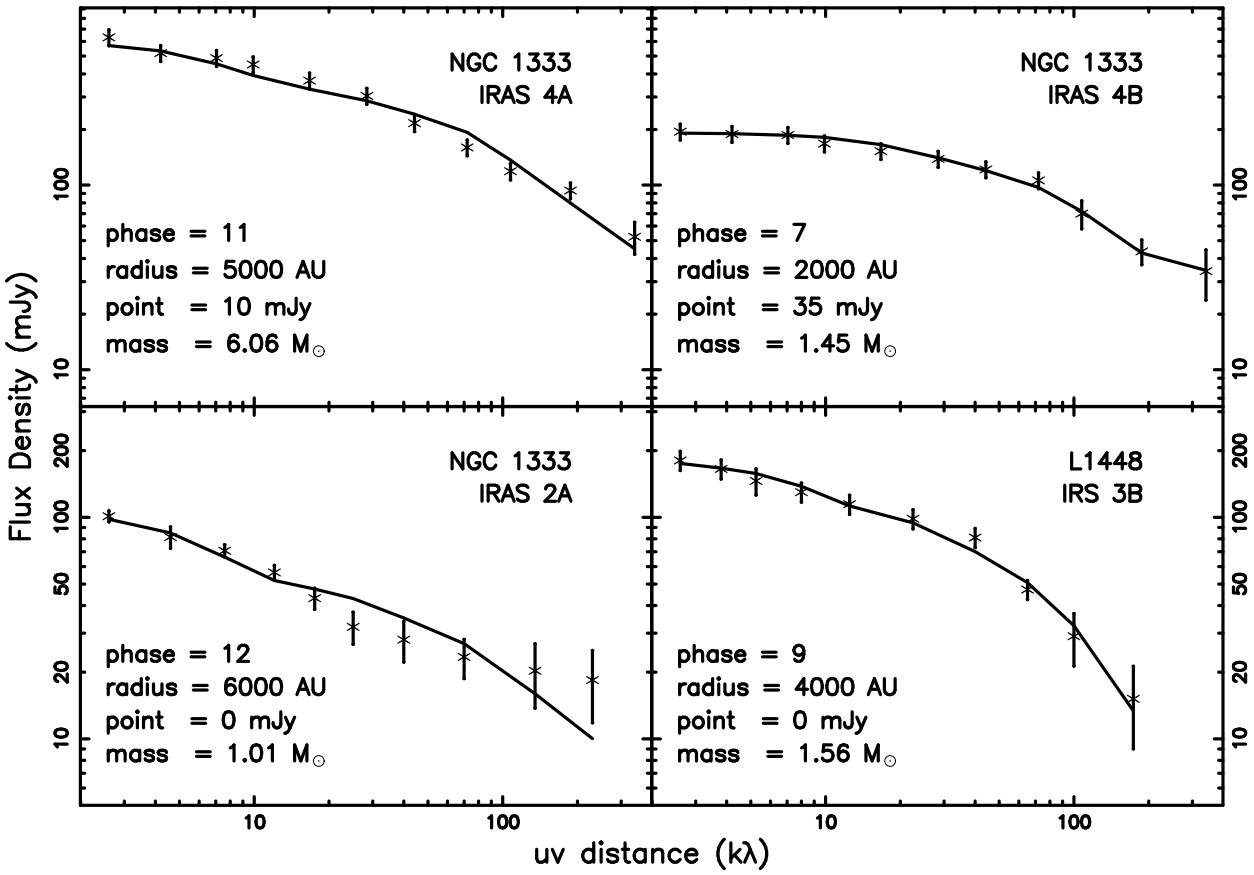

Figure 3.2 The flux density of the observational data and the best fit for each source with best fit parameters listed. The χ^2 values are 1.49, 0.22, 1.30, and 0.41 for NGC 1333 IRAS 4A, IRAS 4B, IRAS 2A, and L1448 IRS 3B, respectively.

code allows the calculation of the expected flux as a function of radius in the image plane or as a function of *u-v* distance in the Fourier plane. This provides the best way to trace emission structure to very small length scales, effectively the density and temperature profiles in the inner circumstellar envelope.

For each object, we did a parameter fitting of the model to the observational data with four degrees of freedom: evolutionary phase (density profiles) in the TM2005 magnetic cycle, outer cutoff radius of the envelope, central point source flux, and envelope mass. The inner cutoff radius is fixed to be 10 AU to be consistent with the central sink approximation used in TM2005 and also the inner envelope is truncated by the central disk physically. In Figure 3.3 we show the evolutionary phases in *u-v* space with all other parameters fixed for an example case of outer radius 5000 AU, envelope mass 5 $M_{\odot}$, no point source flux, and a fixed power-law temperature profile of index -0.4 and 500 K at 1 AU as an optically thin case (*the solid curves*). The difference between the phases in *u-v* space is mainly at large *u-v* spacings, corresponding to the shock propagation in the density profiles. On the other hand, adding a point source is like adding a constant in *u-v* space, which effects the slope in logarithmic plots; increasing the envelope mass increases amplitude in all *u-v* spacings, especially in short *u-v* spacings; changing the outer radius alters the overall level and also the distribution of *u-v* amplitudes. The effects from varying each single parameter intertwine together and degeneracy makes it difficult to point out which parameter is the key to each good fit; moreover, the self-consistent temperature profile considers the increase of optical depth near the center of the envelope and influences the predicted emission.

Model images of the envelope are computed with consideration of the envelope emission and the central point source attenuated by the dust envelope. The self-consistent temperature profiles are calculated from the assumed luminosity, which was derived from the far-infrared flux density (see Looney et al. 2003) and listed in column 2 in Table 3.1. The model images are multiplied by the observational primary beam, Fourier transformed into visibilities, and sampled with the same *u-v* coverage as the observations. Both model and

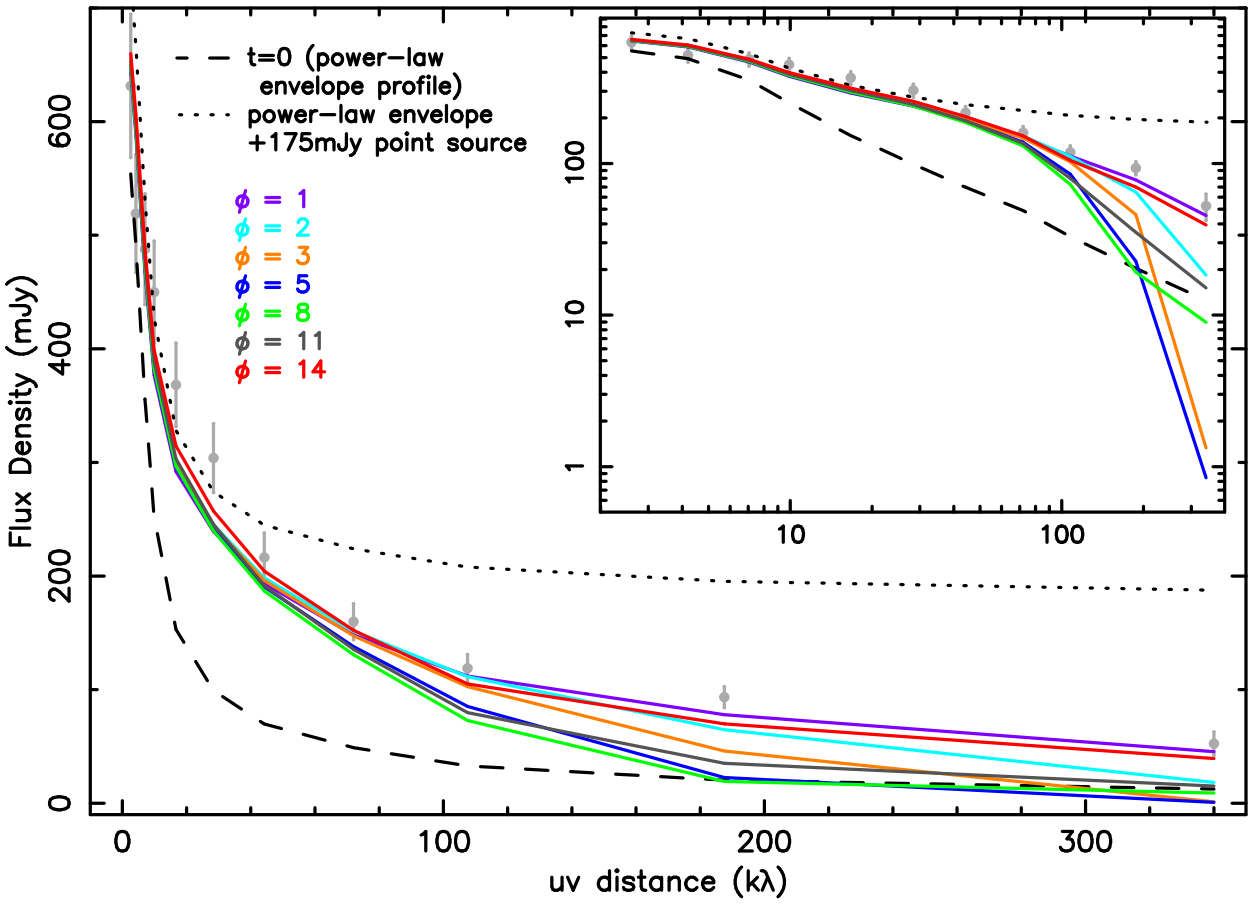

Figure 3.3 The solid curves show the example u-v visibilities from an optically thin envelope with outer radius 5000 AU, mass 5 $M_{\odot}$, and various evolutionary phases (no point source flux is added, and observational parameters such as the distance and u-v samplings are assumed to be the same as NGC 1333 IRAS 4A). Different colors correspond to different phases in the TM2005 model, as the density profiles of these phases are plotted in Figure 3.1. The dashed curve is the flux density of the same case but with the initial density profile of TM2005, which is a nearly power-law profile with index -1.7. The dotted curve is the same nearly power-law envelope emission plus a constant 175 mJy (a point source flux) representing an unresolved disk. The same visibilities are also plotted in a logarithmic scale in the inset panel. The observational data points of NGC 1333 IRAS 4A are shown for comparison. The power-law envelope itself (*the dashed curve*) is not a good fit; also, just adding a point source flux to the power-law density profile cannot fit the data (*the dotted curve*). This is similar to the results from Jørgensen et al. (2005). However, the predicted envelope emission from the TM2005 model is very different and a better fit to the data.

observational data are binned and averaged in u-v annuli, shown as the flux density as a function of u-v spacing, and compared to each other. A reduced χ_r^2 is computed to determine the goodness of a fit. Among the four degrees of freedom, the total envelope mass is adjusted to minimize χ_r^2 while the other three parameters are fixed. This nonlinear minimization is done for any combination of these three parameters with outer radius ranging from 2000 to 9000 AU and point source flux as the ranges given in the parentheses in Table 3.1, and for each set of parameters a total envelope mass was obtained with local minimal χ_r^2. Collecting the results of sets of parameters, the best fit, with global minimal χ_r^2 is found.

3.4 Results and Discussion

In Figure 3.2, data are binned, averaged, and shown by asterisks with associated error bars, and the curves show the best fit for each source as a function of u-v distance with the best fit parameters given on the plot. The best fit parameters do not need to be the same as those in Looney et al. (2003) since a different theoretical model is used here. Figure 3.4 shows the corresponding density and temperature profiles for these best fits. The straight dashed lines in the temperature plots are lines with slope -0.4, which would be the temperature profiles if the envelopes are optically thin ($T \propto r^{-0.4}$). We can see that the outer part of the envelopes is nearly optically thin, and becomes hotter and optically thicker at smaller radii.

We refer to a fit with more than 90% confidence level as an acceptable fit, and a summary of acceptable fits is given in Table 3.1. Fitting with density profiles at different phases implies that the systems may be at different phases of a magnetic cycle. Presumably, if we had data of more objects we might catch systems at all phases. The acceptable fits spread over a range of parameters depending on the signal-to-noise ratio of the observations. One important aspect of the modeling is the clear need for high signal-to-noise data. The χ^2 value is the evaluation quantity of the goodness of a set of parameters, and is smaller when the observational uncertainties are larger; low signal-to-noise ratio data make acceptable fits

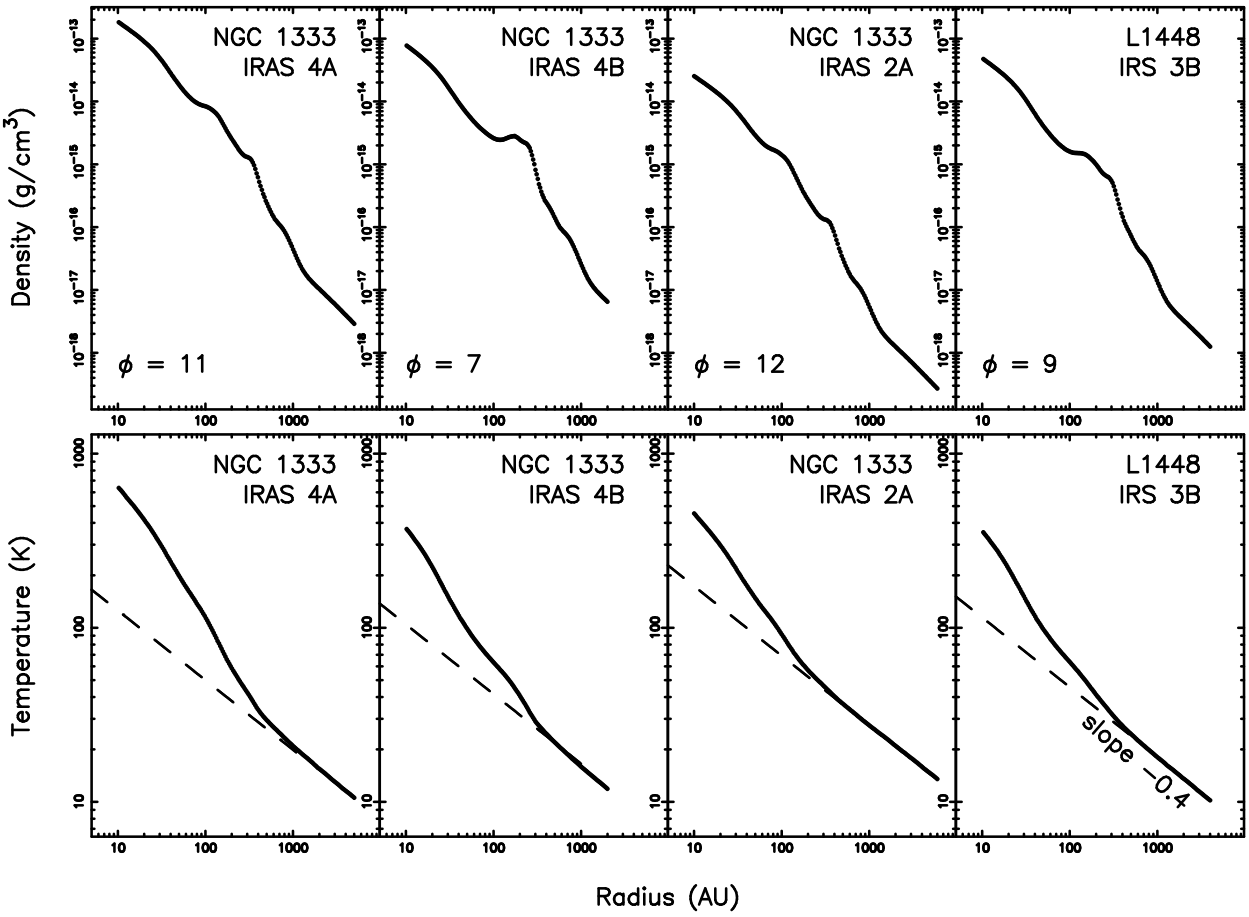

Figure 3.4 The density and temperature profiles of the best fit for each source. The straight dashed lines in the temperature plots show the optically thin case.

Table 3.1. Acceptable Fits

Source Name	Luminosity ($L_\odot$) [a]	Density Profiles (Phase) [b]	Outer Radius (AU)	Point Source Flux (mJy) [c]	Envelope Mass ($M_\odot$)	Good Fits [d]
NGC 1333 IRAS 4A	16	9-11	4000-5000	0-50 (0-50)	4.88-6.23	15/720
NGC 1333 IRAS 4B	5.2	1-14	2000-6000	0-56 (0-56)	1.45-4.02	302/1215
NGC 1333 IRAS 2A	30	2-13	5000-8000	0-7 (0-21)	0.76-1.37	49/480
L1448 IRS 3B	6.8	3-12	2000-9000	0-18 (0-18)	0.75-4.37	223/480

Note. — A set of parameters gives a good fit (a so-called acceptable fit) if the reduced χ^2 is within the 90% confidence level. For each parameter the range of acceptable fits is given.

[a] All sources here are binary system and flux of single component is assumed based on the ratio of fluxes at $\lambda = 2.7$ mm (see Looney et al. 2003).

[b] The number corresponds to a specific phase in the cycle for which the density profile of the TM2005 model provides an acceptable fit (see Figure 3.1).

[c] The parameter search ranges fitting are listed in the parentheses.

[d] The numbers of good fits and the total number of combinations while fitting.

easier. When the signal-to-noise ratio is too low, the fitting becomes meaningless, which is why we apply the analysis only to four sources from Looney et al. (2000). This argument is consistent with our results that the best constraints of model parameters is provided by the highest signal-to-noise observation IRAS 4A among all four sources. Given better signal-to-noise ratio data at more wavelengths in the future we may be able to constrain the model better not only for more sources but also for better-constrained parameters.

Nonetheless, the most important result of this study is that with the TM2005 theoretical model, we can easily fit the observations of these sources without conflicts of ages, unlike the fits using the LP or Shu models (Looney et al. 2003), although the exact source age is not determinable by comparison with the TM2005 model. Due to the episodic nature of the theoretical model, we are not fitting nor implying a specific age for the source, but the range of age is 15 to 255 kyr. Parsec-scale jets and outflows have been found in these regions and can be used to estimate the ages of central sources that drive the outflows. For example, the timescale of the outflows in NGC 1333 is of order 10^5 yr (Bally et al., 1996), which is consistent with the age range of the TM2005 model.

We use the phases of a typical magnetic cycle for the fitting. TM2005b Figure 5 shows

the beginning evolution after the central sink is introduced and the system has the first magnetic cycle at about $t = 15$ kyr; then it repeats the magnetic cycles as in TM2005b Figure 8 and Figure 9 until $t = 255$ kyr when the sink mass reaches 1 $M_\odot$ and the simulation stops. Once the cycling behavior has been well established, all physical quantities show high similarity of variation from cycle to cycle. Only the period of a cycle, which is about several thousand years, decreases with time, controlled by the ambipolar-diffusion timescale at the position of the magnetic wall; other than that, there is no obvious difference between cycles. So given a fit to a density profile, the system may be at a specific phase of any cycle during this epoch. However, the age range suggested by the theoretical model is consistent with the age estimated by the outflows' scale, which implies that the observational data are consistent with the TM2005 picture of early star formation.

One of the most important differences between the TM2005 and the Shu or LP models is that the steep power-law-like density profiles of TM2005 are actually not in equilibrium, while $\rho \propto r^{-2}$ in the other models corresponding to the singular isothermal sphere is a critical equilibrium situation. In the Shu or LP models, the collapse is induced by an outward-moving rarefaction wave and the density changes dramatically after being affected by the wave; in TM2005, the system is collapsing and mass keeps accreting onto the central protostar dynamically without making an abrupt change, except for the relatively small bump generated by the magnetic wall. Periodic creation and dispersion of the magnetic wall dominate the variation of density profiles and also the accretion, so the whole collapse process is regulated by magnetic forces. Accounting for magnetic fields in the theoretical models, the density profiles at later times of the evolution are very different from those of the Shu or LP models, and are better matched with the observations and estimated ages from outflows.

Can we constrain the earliest disks? Table 3.1 shows that in all cases, we can fit our sources without a circumstellar disk component at the 90% confidence level. On the other hand, a disk is expected early on in the collapse process due to the rotation and/or magnetic

fields in the initial cloud. As material accretes, the disk receives more mass from the envelope. The mass is processed in the disk, which regulates mass flow through the disk and onto the protostar. The magnetic fields within the disk and star give rise to an outflow (e.g., Shang et al., 2007; Pudritz et al., 2007) that is typically seen even in very young sources, suggesting that a disk is established nearly concurrently with the protostar's growth in luminosity as it collapses to stellar size. In fact, simple theoretical arguments suggest that the disk evolves early and grows quickly with time as $\sim t^2$ or $\sim t^3$ (e.g., Stahler & Palla, 2005), which depends crucially on the mass accretion rate.

Although not a statistical requirement, we do expect these sources to have some sort of deeply embedded circumstellar disks in the center of the infalling envelopes. We can use HL Tau, which was modeled in Mundy et al. (1996), as a standard candle to estimate the mass of the disks in our modeled systems. Also using BIMA $\lambda = 2.7$ mm dust continuum observations, the total flux from HL Tau was ∼100 mJy, and the derived disk mass from modeling was ∼0.05 $M_\odot$. Based on the assumption of equal flux to disk mass ratio corrected by the distance, the value 0.010 Jy in the best fit point source flux for NGC 1333 IRAS 4A corresponds to a disk of mass 0.03 $M_\odot$, and 0.035 Jy for IRAS 4B corresponds to a 0.11 $M_\odot$ disk. A distance to NGC 1333 of 350 pc has been assumed here. If we use a distance of 250 pc instead, the estimated mass of embedded disks for the best fits would be 0.016 $M_\odot$ and 0.056 $M_\odot$ for IRAS 4A and IRAS 4B, respectively. The acceptable fits with maximum disk components give disk mass of 0.16 $M_\odot$, 0.18 $M_\odot$, 0.065 $M_\odot$, and 0.041 $M_\odot$ for NGC 1333 IRAS 4A, IRAS 4B, IRAS 2A, and L1448 IRS 3B, respectively. It gives an upper limit of disk mass to IRAS 2A since model parameters with higher point source flux cannot fit anymore.

Unlike Jørgensen et al. (2005), a disk component is not crucially necessary in our modeling. The major reason is that different envelope models are used. TM2005 predict a very different visibility amplitude profile from what is expected by a power-law density profile. For example, in Figure 3.3, the dashed curve is the predicted u-v amplitude of a nearly

power-law density profile of index -1.7 (the initial density profile in the TM2005 simulation), and the dotted curve is generated with the same density profile, but with a point source flux representing an unresolved circumstellar disk. As can be seen, the envelope emission from a power-law density profile shows a very different shape than those predicted by the phases of the magnetic cycle. TM2005 density profiles are able to fit the data well without adding a Gaussian disk (cf. Jørgensen et al., 2005). Again this shows the importance of understanding the collapsing envelope in order to understand the embedded disk.

3.5 Summary

1. Although interferometry is a powerful tool in resolving out the large-scale emission of the envelope, the ability to detect a disk in the presence of an envelope is not set by the formal noise level or Fourier components, but by the intrinsic ability to model the complexity of the envelope (inner cutoff, asymmetric structure, etc.) and by the resolution of the observations compared to the disk size and the inner cutoff of the envelope. In other words, reliable detection of the embedded circumstellar disk requires a knowledge of the physical parameters of the inner envelope.

2. Our observational data are consistent with the theoretical predictions of Tassis & Mouschovias (2005) concerning the density profiles. Moreover, there is no discrepancy in age based on the size of the outflows, unlike the fitting results of the simpler Shu or LP solutions to the isothermal sphere (e.g., Looney et al. 2003). It is important to note that the exact age cannot be determined by comparison between the interferometric data and the model of Tassis & Mouschovias (2005) due to its periodic nature. Regardless of the collapse initiation, the magnetic fields may play an important role early on in the collapse process. To expand this comparison, we will continue to observe Class 0 objects at higher sensitivity and multiple wavelengths, better incorporating the theoretical models into our comparisons (see Chapter 5).

3. Although our initial results do not require the existence of circumstellar disks (acceptable fits of 0.0 to 0.11 $M_{\odot}$), we can place upper limits on the disk masses. In general, the disks are less massive than $\sim$0.1 $M_{\odot}$. The youngest circumstellar disk mass is not overly massive compared to other well known Class II or III circumstellar disks. The fact that a disk component is not statistically necessary in this modeling is different from the similar work at sub-millimeter wavelengths by Jørgensen et al. (2005). The main reason is that we use the density profile predicted by Tassis & Mouschovias (2005) instead of a simple power-law profile of the envelope.

Chapter 4

Synthetic Interferometric Observations of a Class –I Object

4.1 Motivation

Understanding the role of magnetic fields in the process of star formation has always been an observational challenge. Recently, Kunz & Mouschovias (2009, 2010, hereafter KM2010) have developed a new numerical model, studying YSO evolution from pc-scale molecular cloud to AU-scale hydrostatic core. This is the first theoretical magnetic model that considers a non-isothermal axisymmetric self-gravitating core with effects of grain chemistry, radiation, and magnetic fields, including ambipolar diffusion and Ohmic dissipation. At large scales, an oblate geometry, due to the presence of magnetic fields, is predicted; while at small scales, thermal pressure dominates and a spherical core is constructed. The suggested geometry of the KM2010 model is contrary to that of the non-magnetic TSC model (Terebey et al., 1984), which expects a disk structure inside spherical envelope due to initial angular momentum. Figure 4.1 shows the density and temperature distributions of the KM2010 model.

The KM2010 model describes the very early stage of protostellar collapse, equivalently the class –I stage or the first hydrostatic cores (FHSC, Boss & Yorke, 1995; Masunaga & Inutsuka, 2000a). This is in addition to the commonly used classification scheme from Class 0, I, II, to III (Lada, 1987; Andre et al., 2000) to distinguish the group younger than Class 0 sources but more evolved than starless and prestellar cores (Boss & Yorke, 1995). At this very early stage of protostellar collapse, transient between prestellar cores and class 0 stage, a molecular hydrostatic core has formed, but the central density and temperature have not yet reached high enough ($\sim$ 2000 K) to dissociate the molecular hydrogen. It is followed by

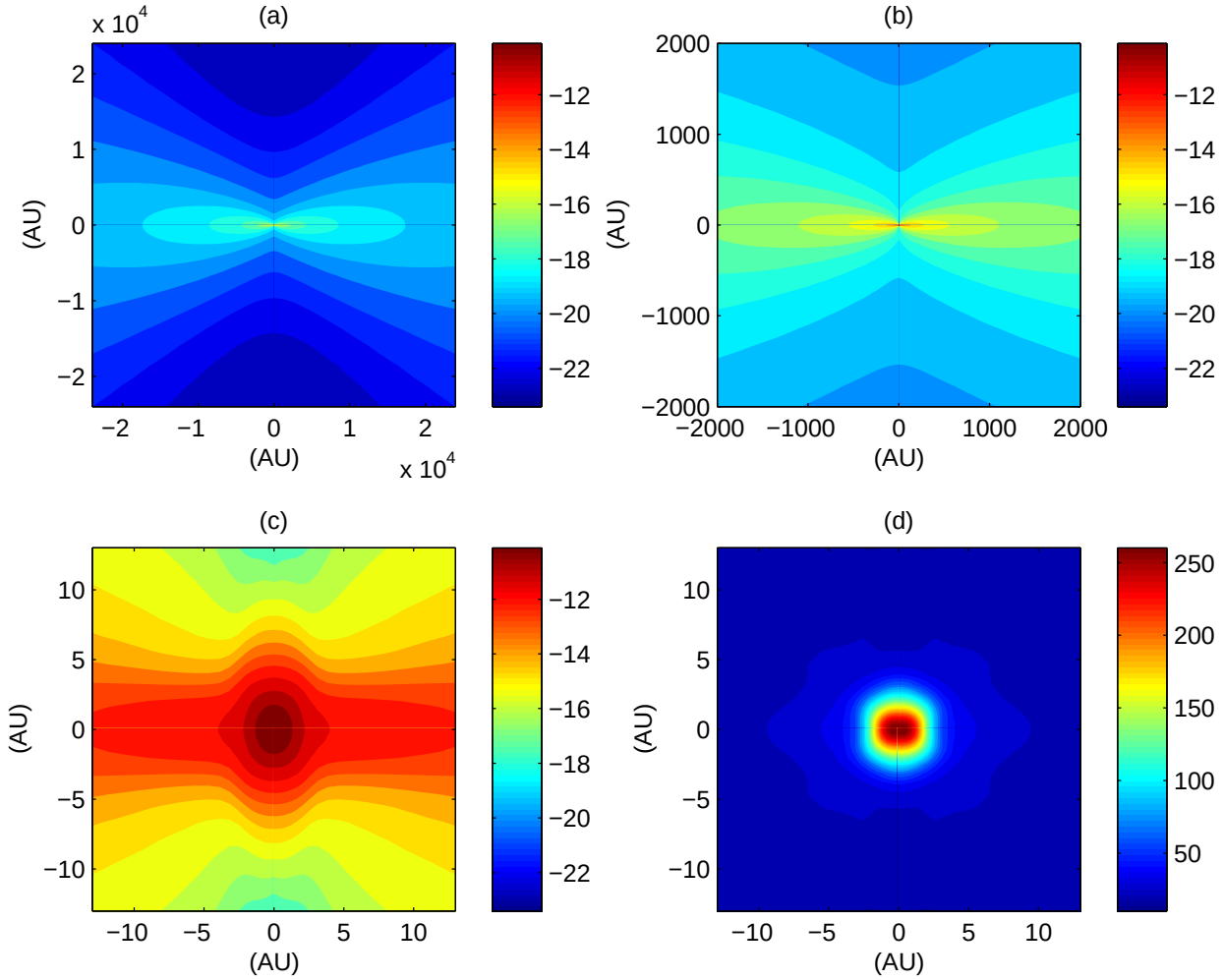

Figure 4.1 Numerical results of the KM2010 model. (a) Neutral density (in g cm^{-3}). Color contours are in logarithmic scales. (b)-(c) Same as panel (a) but zoomed in to focus on the inner region. (d) Gas temperature (in K).

the second collapse, triggered by dissociation of molecular hydrogen, to form a true class 0 protostar.

Observations of Class –I YSOs have been rare, as these extremely young objects are cool and faint. To date, only a few candidate Class –I objects have been suggested. For example, Chamaeleon-MMS1 (Belloche et al., 2006), L1448 IRS 2E (Chen et al., 2010), Per-Bolo 58 (Enoch et al., 2010; Dunham et al., 2011), and L1451-mm (Pineda et al., 2011) are some candidate sources and the last three drive molecular outflows. More candidate sources have been suggested but none of the identification is definite yet (see the discussions in Dunham et al., 2011). Furthermore, observational properties of Class –I YSOs and its relation with the Very Low Luminosity Objects (VeLLOs, embedded sources with internal luminosity below 0.1 $L_{\odot}$, Kauffmann et al., 2005; Dunham et al., 2008) remain unclear.

With the increasing popularity of the Class –I YSOs and results of theoretical simulations on hand, we carry out synthetic observations of current and future interferometers including Combined Array for Research in Millimeter Astronomy (CARMA), Atacama Large Millimeter Array (ALMA), and Expanded Very Large Array (EVLA). Moreover, while directly measuring magnetic fields strengths in star-forming regions is currently constrained to bright sources only, one can alternately test the magnetic theories by comparing the predicted envelope structure with interferometric observations.

4.2 Methods

To simulate interferometric observations of a typical KM2010 Class –I objects, we first map the model brightness using radiative transfer calculations in full geometry. A distance of 250 pc, which is a typical distance to nearby star-forming regions, is assumed. With the density and temperature profiles from the KM2010 numerical simulations, the specific intensity of

dust thermal emission can be calculated by

$$I_\nu = \int_{los} B_\nu(T)\, e^{-\tau_\nu}\, \mathrm{d}\tau_\nu = \int_{los} B_\nu(T(\vec{r}))\, e^{-\tau_\nu(\vec{r})}\, \rho(\vec{r})\, \kappa_\nu\, \mathrm{d}\vec{r}, \tag{4.1}$$

where $B_\nu(T)$ is the Planck function at dust temperature T, τ_ν is the optical depth from the position $\vec{r}$ along the line of sight to the observer, ρ is the envelope density, and $\vec{r}$ denotes the position. Consistent dust opacity coefficient κ_ν, which is dependent of both temperature and frequency, as in the KM2010 model is used. Model images of dust emission are calculated with spatial resolution much higher than observational resolution. Also, multiple wavelengths are considered depending on the telescope capabilities.

Interferometers sample emission at the spatial scales determined by the baselines of antenna pairs in the array configurations. Therefore, information at the non-observed scales is lost. In other words, interferometers filter emission spatially, and emission at scales larger than the scale set by the shortest baseline is resolved out. The interferometric filtering effect complicates the interpretation to the observed images, but it allows us to detect individual components of specific scales and minimizes confusion from the background clouds. Other observational effects such as primary beam correction and Fourier transform are considered by the Multichannel Image Reconstruction, Image Analysis and Display (MIRIAD [1]) software for CARMA and by the Common Astronomy Software Applications package (CASA [2] [3]) for ALMA and EVLA observations.

4.3 Synthetic Interferometric Observations

We carry out synthetic observations by CARMA, ALMA, and EVLA to examine the interferometer response to the KM2010 model. Inclination angles of 0, 30, 60, 75, and 90 degrees are considered at multiple array configurations to demonstrate the observability of

[1] http://carma.astro.umd.edu/miriad/
[2] http://casa.nrao.edu/
[3] http://casaguides.nrao.edu/

the circumstellar structures in the KM2010 model. In the following sections, the results of synthetic interferometric observations are presented as long with modeling specifications.

4.3.1 CARMA

CARMA observations at 1.3 mm dust continuum are simulated using the MIRIAD package. In particular, most observational effects are modeled by uvmodel . We consider observations in A- and C-configuration using the revised CARMA correlator (Rauch, 2011) with the optimal setup for continuum, that is, with a bandwidth of 3.5 GHz at both upper and lower sidebands for a total bandwidth of 7 GHz.

The CARMA RMS Calculator gives a noise level of ∼0.5 mJy/beam for an integration of 4 hours with 4-bits sampling of the correlator and natural weighting. A typical weather condition, $\tau_{zenith} \sim 0.32$ at 1.3 mm, is assumed. Observational effects from the heterogeneous interferometer are included. For example, the image is corrected by the primary beam effect considering the baselines of both the 6.1-meter BIMA dishes and 10.4-meter OVRO dishes and the combinations. We first simulate images without noise, then add noise in in the image space according to the CARMA RMS calculator. Results are shown in Figure 4.2.

4.3.2 ALMA

We utilize the simdata task in CASA to simulate fully operational ALMA observations. We consider dust continuum observations centered at 100 GHz with the Band 3 receiver. The full 8 GHz bandwidth with dual polarizations is used, therefore, the effective bandwidth becomes 16 GHz. Fifty 12-m antennas are used with a total observing time of 1 hour. According to ALMA Sensitivity Calculator [4], the expected surface brightness sensitivity is ∼6 μJy/beam.

The highest angular resolution achievable by ALMA will be ∼0.04″ at 100 GHz. Here we demonstrate the cases with beamsizes of 0.05″ and 0.25″. Note that practically, ALMA

[4]http://www.eso.org/sci/facilities/alma/observing/tools/etc/index.html

has dynamical configurations to match the requested beamsize instead of having named configurations. Thermal noise from the atmosphere and the receiver with current ALMA specifications are considered. The AATM library is used for modeling the atmospheric transmission at the site. The precipitable water vapor is assumed to be 2.3 mm, the typical value at the site for 100 GHz observations. Also, the ambient temperature is assumed to be 269K. However, ALMA will use Water Vapor Radiometers to correct the atmospheric delay fluctuation, so the real observations will be potentially better.

Figure 4.3 shows the simulated observations. We plot the contours according to the noise level determined by the images, which is a factor of a few higher than the estimations of the ALMA Sensitivity Calculator. The reasons are (1) we overestimate the noise level by eye, and (2) noise from imaging makes it worse, especially in cases structures are resolved out.

4.3.3 EVLA

We also use the simdata task in CASA to simulate EVLA observations. We consider thermal continuum at 7 mm (or 42.86GHz) observed by the EVLA Q-band receiver and 27 25-m antennas. With a bandwidth of 2GHz, dual polarization, and 4 hour of integration in average spring weather, the EVLA Exposure Calculator [5] estimates the noise to be $\sim$6.6 μJy with natural weighting. Observations are simulated in A and C configurations with beamsizes of around 0.05″ and 0.5″.

Observations are first simulated without thermal noise in CASA, and then random noise is added in the image space. Results without and with the addition of thermal noise are shown in Figure 4.4 and Figure 4.5, respectively.

[5] http://science.nrao.edu/evla/tools/exposure/exposurecalc.shtml

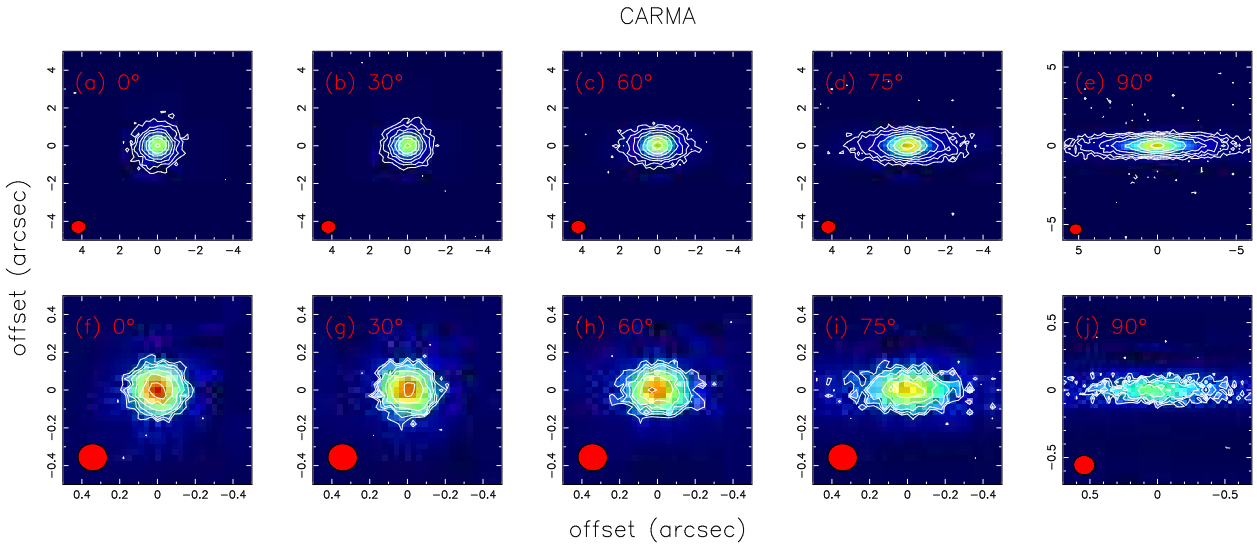

Figure 4.2 Synthetic CARMA observations in A and C configurations. (a)-(e) C-array, contour levels are [-3,3,5,8,12,20,30,50,70]×0.499 mJy/beam (f)-(j) A-array, contour levels are [-3,3,4,5,7,10,14,20]×0.499 mJy/beam

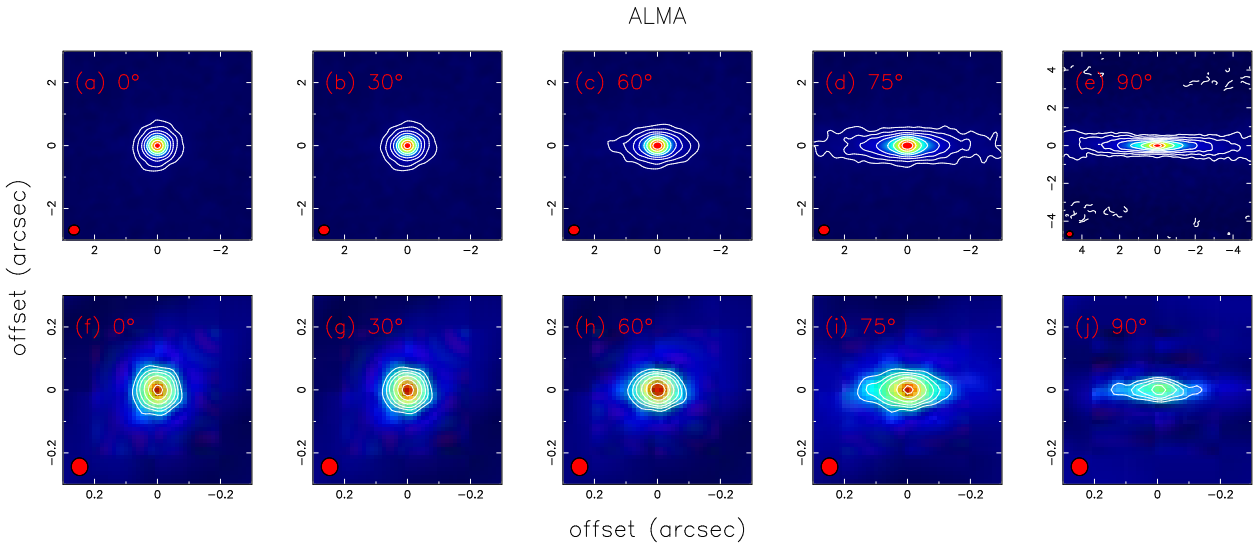

Figure 4.3 Synthetic ALMA observations with two resolutions. (a)-(e) Contour levels are [-2,3,5,8,12,20,30,50,70]×0.02 mJy/beam (f)-(j) Contour levels are [-2,3,4,5,7,10,14,20]×0.03 mJy/beam

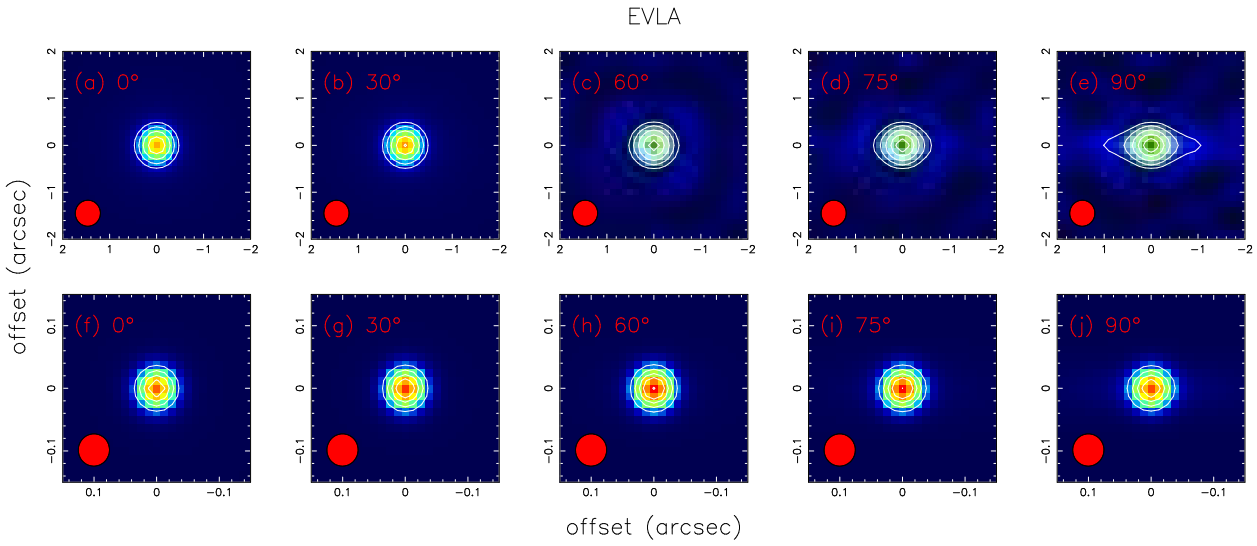

Figure 4.4 Synthetic EVLA observations without thermal noise. (a)-(e) C-configuration. Contour levels are [-2,3,5,8,12,16,20]×6.615 μJy/beam (f)-(j) A-configutation. Contour levels are [-2,3,5,7,9,12,15]×6.615 μJy/beam

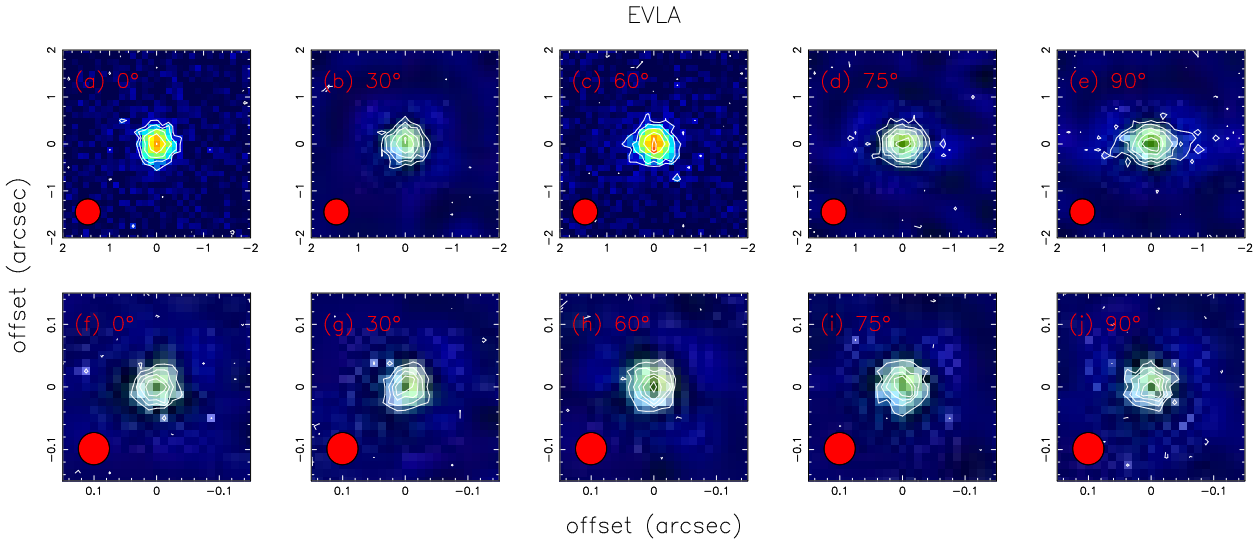

Figure 4.5 Synthetic EVLA observations with thermal noise. The contour levels are identical to Figure 4.4.

4.4 Prospects

Class –I YSOs represent the transient sources with evolutionary stages between prestellar cores and Class 0 protostars. Their properties remain highly uncertain both theoretically and observationally. To date, several candidate sources have been identified with a wide variety of observational characteristics such as luminosity and outflow (e.g., see Dunham et al., 2011). As more observational data towards these objects are collected, these sources will be soon better understood. In particular, while their evolutionary stage is mostly determined by their SEDs and luminosity, interferometric observations resolve the emission in multiple scales, allowing us to examine their spatial structures. Theoretical envelope models have been used to fit some candidate Class –I YSOs, but implications are mostly confined by observational resolution and sensitivity so far (e.g., Pineda et al., 2011).

The KM2010 model is the first model that considers both non-ideal magnetohydrodynamic effects and radiation field for the early core formation process. Unfortunately, the computation is too expensive to evolve past the Class –I stage, therefore it would be unfair to compare the KM2010 model with Class 0 sources, such as those presented in Chapter 2 and Chapter 3. However, synthetic observations based on the KM2010 model give us a picture of the observability of these sources by current and future interferometers. A Class –I object as predicted by the KM2010 model is detectable by forthcoming observations and its spatial structure can be resolved if the inclination is close to edge on. Also, synthetic observations are the basic of future model-data comparison, which, combined with statistical inference, provides a way to test star formation theories. A more complete modeling with interferometric data of YSOs will be discussed in the next chapter.

Chapter 5

Constraining the Earliest Circumstellar Disks and their Envelopes: II. Full Modeling

5.1 Introduction

Protostars are surrounded by their parental envelopes in the earliest stage of evolution. These envelopes supply the material that is actively infalling onto the embedded star-disk system, and their properties can affect the subsequent evolution. However, the physical conditions of these envelopes and the detailed processes of the gravitational collapse remain uncertain to date. Some theoretical work has been done to address the collapse process. For example, the Shu (1977) model presents the collapse process of a singular isothermal sphere. A perturbation near the center starts the collapse, and the collapse wave propagates inside-out, while the region inside the collapse wave undergoes free-fall infall. Although simple and illustrative of the basic physics during collapse, the Shu model fails to fit a sample of class 0 protostars with reasonable ages (Looney et al. 2003). The next generation model of Terebey, Shu, & Cassen (1984, hereafter the TSC model) builds on the Shu model and considers the effects of non-zero angular momentum. The TSC model has been widely used in studies of young stellar objects, and consistent results have been obtained, especially in fitting the spectral energy distributions of unresolved young stellar objects (e.g., Robitaille et al., 2007).

Interferometers allow us to measure the brightness at various spatial scales, providing a powerful tool to probe the structures of protostellar envelopes and reveal the process of star formation. While various theoretical models of the collapsing envelope have been suggested, distinguishing among them has always been an observational challenge. With the aim to bet-

ter constrain the envelope structure, we carry out a complete modeling with dual-wavelength data of different spatial resolutions. By comparing the predicted envelope structure with interferometric observations, theoretical collapse models are tested (e.g., Chiang et al., 2008; Maury et al., 2010). A better understanding of the envelope also enables us to constrain the physical properties of the embedded disk component.

In this chapter, we focus on the edge-on Class 0 protostar L1157-mm (also known as L1157-IRS or IRAS 20386+6751, hereafter L1157) at the distance of 250 pc (Looney et al., 2007). A chemically active outflow driven by L1157 has been detected in multiple species (Gueth et al., 1996; Bachiller et al., 2001; Nisini et al., 2010). Perpendicular to the outflow orientation, a flattened envelope with a linear size of ∼20,000 AU is seen in 8 μm absorption (Looney et al., 2007), as well as in N_2H^+ and NH_3 emission (Chiang et al., 2010; Tobin et al., 2011). The molecular line observations show complex kinematics from rotation, infall, and outflow in the envelope. On the other hand, dust continuum traces the envelope structure as well as reveals a compact core (e.g., Gueth et al., 2003). Additionally, the presence of a circumstellar disk embedded inside the envelope has been implied by methanol observations (Goldsmith et al., 1999; Velusamy et al., 2002).

A complete analysis requires a well-sampled u-v plane; therefore, we have collected 1 mm and 3 mm interferometric data at multiple array configurations using the Combined Array for Research in Millimeter-wave Astronomy (CARMA [1] [2]). §5.2 overviews the observations and the data reduction. Details of the modeling are addressed in §5.3, including the description of our statistical approach (§5.3.5). The results are shown in §5.4, their implications are discussed in §5.5, and a summary is given in §5.6.

[1] http://www.mmarray.org/

[2] Support for CARMA construction was derived from the states of Illinois, California, and Maryland, the James S. McDonnell Foundation, the Gordon and Betty Moore Foundation, the Kenneth T. and Eileen L. Norris Foundation, the University of Chicago, the Associates of the California Institute of Technology, and the National Science Foundation. Ongoing CARMA development and operations are supported by the National Science Foundation under a cooperative agreement, and by the CARMA partner universities.

Table 5.1. Summary of Observations

Frequency (GHz)	Array Config.	Date	Observing Time (hr)	Bandpass Calibrator	Flux Calibrator	Beam Size [a] (″)	Beam P.A. [a] (degree)
229	B	2007-12-17 [b]	1.5	3C454.3	MWC349	0.4×0.3	-75
	C	2008-04-13	3.1	3C454.3	MWC349	1.0×0.8	-66
	D	2008-03-07	3.1	3C454.3	MWC349	2.3×2.0	-29
91	A	2009-01-27 [bc]	3.3	1642+689	MWC349	0.4×0.3	-65
		2010-01-26 [bd]	2.2	3C273	MWC349		
		2010-02-01 [bd]	2.9	3C454.3	Neptune		
	B	2007-11-17 [b]	4.5	1751+096	MWC349	0.9×0.8	-83
		2007-11-19 [b]	2.4	3C454.3	Neptune		
		2007-11-20 [b]	1.5	3C273	3C273		
		2009-12-14 [b]	0.6	3C454.3	Uranus		
		2009-12-15 [bd]	5.4	3C345	MWC349		
	C	2007-10-03	2.5	1751+096	MWC349	2.3×2.0	-87
		2007-10-05	2.8	1751+096	MWC349		
		2008-04-05	4.8	3C273	MWC349		
	D	2008-02-29	3.1	3C454.3	Uranus	6.0×5.2	84
		2009-03-19	6.0	3C345	MWC349		
		2009-03-20	6.2	3C345	MWC349		
		2009-03-27	0.8	1642+689	MWC349		
		2009-03-29	3.0	1642+689	MWC349		
	E	2008-10-02	4.2	3C454.3	Uranus	11.5×10.2	78
		2008-10-05	3.5	3C84	MWC349		

[a] The synthesized beam of the combined data with natural weighting at each array configuration

[b] Long-baseline tracks with a secondary phase calibrator 2009+724

[c] The primary phase calibrator for this track is 1849+670 instead of 1927+739.

[d] Track calibrated with C-PACS using the atmospheric calibrator 2022+616

5.2 Observations and Data Reduction

L1157 was observed by the 15-element CARMA during Oct 2007 to Jan 2010. At that time, the science array of CARMA consisted of six 10.4-meter antennas from the Owens Valley Radio Observatory (OVRO) and nine 6.1-meter antennas from the Berkeley-Illinois-Maryland Association (BIMA). Dust continuum at both 1 mm and 3 mm bands was observed using multiple array configurations, as summarized in Table 5.1.

The phase center of the observations before September 2008 was $\alpha = 20^h39^m06\overset{s}{.}20$, $\delta = 68°02'15\overset{''}{.}9$, and shifted to $\alpha = 20^h39^m06\overset{s}{.}26$, $\delta = 68°02'15\overset{''}{.}8$ afterwards as more precise coor-

dinates were determined by high resolution observations. However, all data presented here have been corrected to have the common phase center at $\alpha = 20^h39^m06\overset{s}{.}26$, $\delta = 68°02'15\overset{''}{.}8$ (J2000).

The main phase calibrator for all tracks was 1927+739 (with an exception of one A-array track) and was observed with a phase calibrator-source cycle of 10-15 minutes. For all A- and B-array observations, a weaker quasar, 2009+724, was observed as the secondary phase calibrator. The secondary phase calibrator was not used in the calibration process; instead, it is used to check the point source response. For 3 mm A- and B-array tracks observed in winter 2009-2010, the CARMA Paired Antenna Calibration System (C-PACS; Pérez et al., 2010) was employed to calibrate the atmospheric phase variation on short time-scale. With C-PACS, a reference array continuously monitors a nearby quasar, called the atmospheric calibrator, for atmospheric delay, while the science array observes the science target. The eight 3.5-meter antennas from the Sunyaev-Zel'dovich Array (SZA) were used as the reference array. The C-PACS correction is especially effective for data with long baseline. As an example, Figure 5.1 compares the result image of the science target L1157 with and without the C-PACS correction.

The data reduction, calibration, and imaging were done using the software Multichannel Image Reconstruction, Image Analysis and Display (MIRIAD; Sault et al., 1995)[3]. The bandpass and flux calibrators for each track are listed in Table 5.1. After the data are reduced, the flux density of both primary and secondary phase calibrators is plotted as a function of u-v distance in order to verify that a flat trend, implying that decorrelation is not significant at long baselines, is seen.

The largest uncertainty of interferometric data comes from flux or absolute amplitude calibration. Although independent of relative brightness and image quality, the absolute flux affects significantly on multi-wavelength analysis. The uncertainty can be as large as 10% (e.g., Moreno & Guilloteau, 2002), mostly due to the model of planetary atmosphere used

[3]http://carma.astro.umd.edu/miriad/

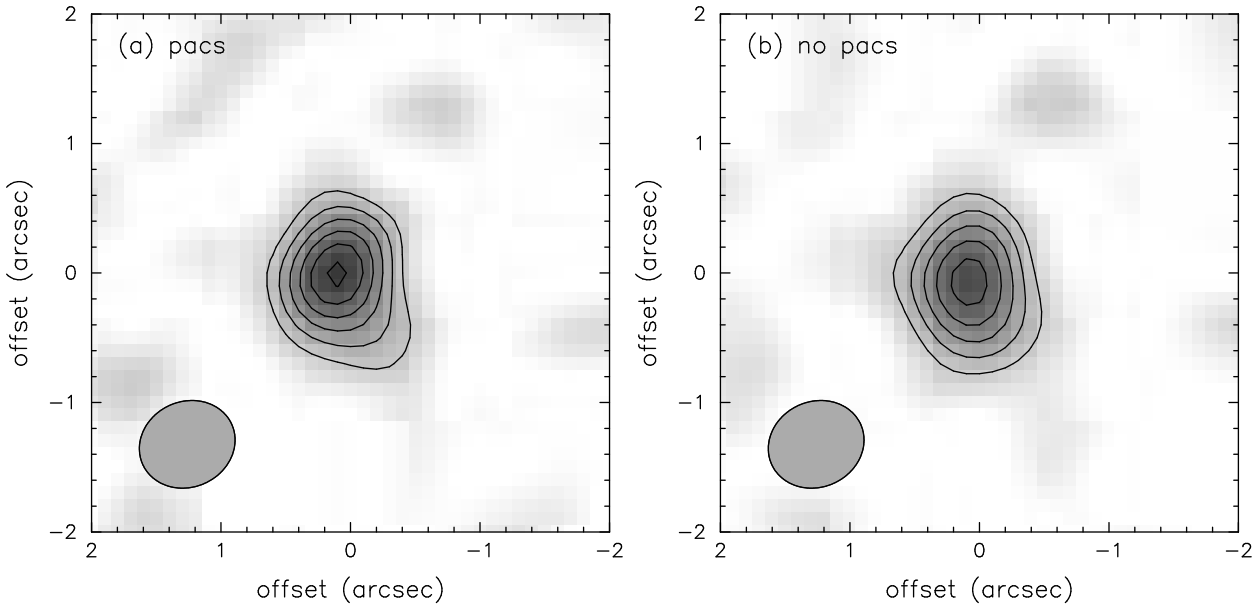

Figure 5.1 Effects of C-PACS calibration shown by the 3 mm dust continuum maps of L1157 with the CARMA B-array data taken on Dec 15, 2009. (a) Calibration of C-PACS is applied. The peak brightness is 11.6 mJy/beam. (b) Calibration of C-PACS is not applied. The peak brightness is 10.4 mJy/beam. In both panels, the contour levels start with 2 σ in increments of 1 σ, where σ is 1.6 mJy/beam.

in the data reduction process. The large uncertainty can not be avoided unless the planet modeling is improved. However, we examine our data for consistency. Figure 5.2 shows the flux density variation with respect to observation dates for the common phase calibrator 1927+739 at 3 mm. Besides the values derived in our tracks, values from the standard CARMA/MIRIAD catalog are also included. Consistent flux density with a smoothly varying trend is seen.

The reduced data of the science target L1157 are shown in Figure 5.3 by the annuli-averaged flux density with respect to u-v distance. Continuum data from all spectral windows are combined. Data taken at different array configurations are shown separately to stress the consistency between the reduced data. Figure 5.4 presents the continuum maps of L1157. Super-uniform weightings with different robustness parameters are used to obtain different synthesized beamsizes in order to emphasize envelope structures at different size scales. The continuum of L1157 shows spherical structures from 2000 AU scale ($8''$) down to 100 AU

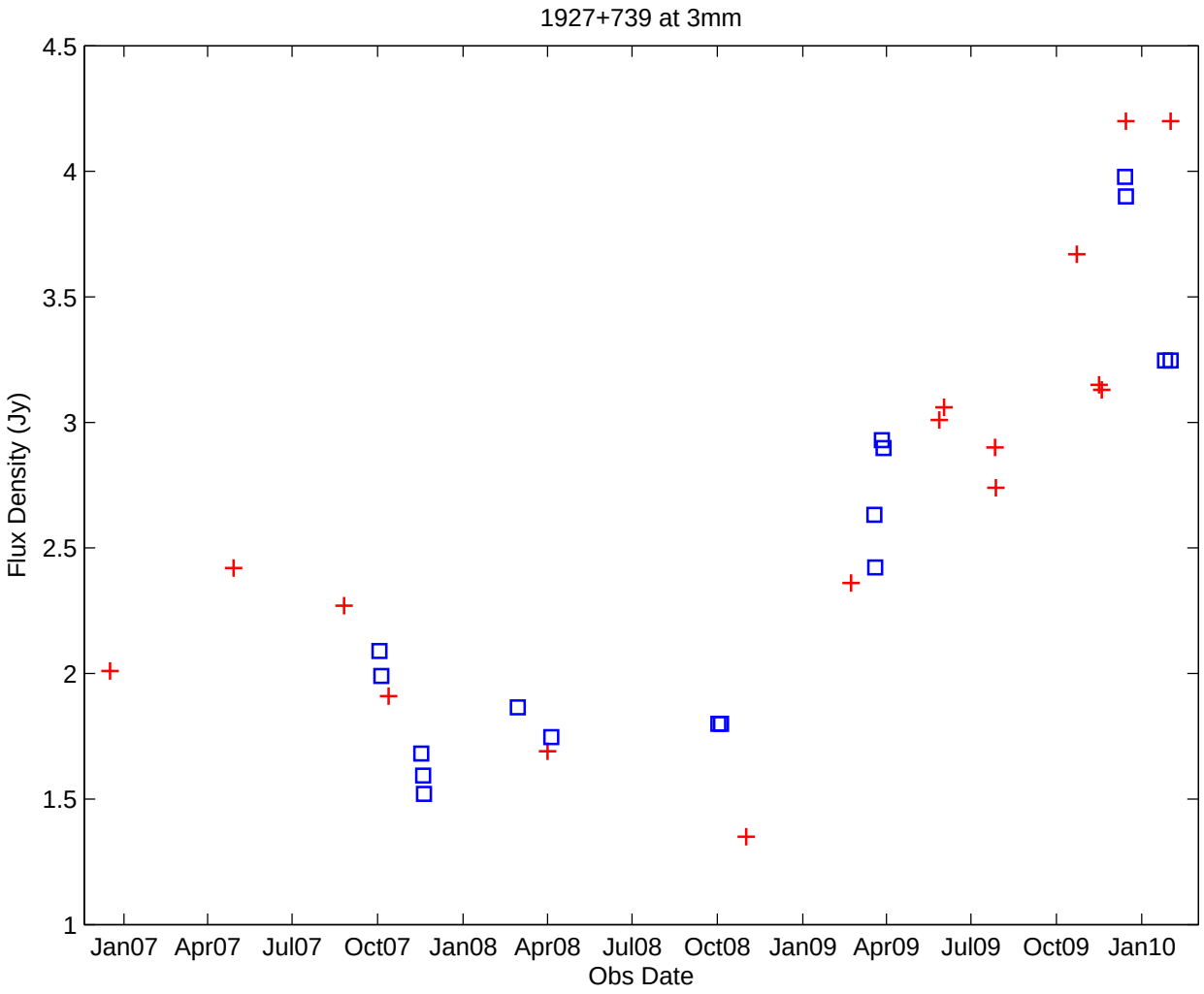

Figure 5.2 The flux density variation of 1927+739, the main phase calibrator, with respect to observation dates. Only the 3 mm data are shown. Crosses represent the standard flux from the CARMA/MIRIAD calibrator catalog; squares represent the derived flux from our data using MIRIAD task bootflux. Each observational track was calibrated separately to deduce the flux of the phase calibrator and the science target. A smooth and consistent trend is seen.

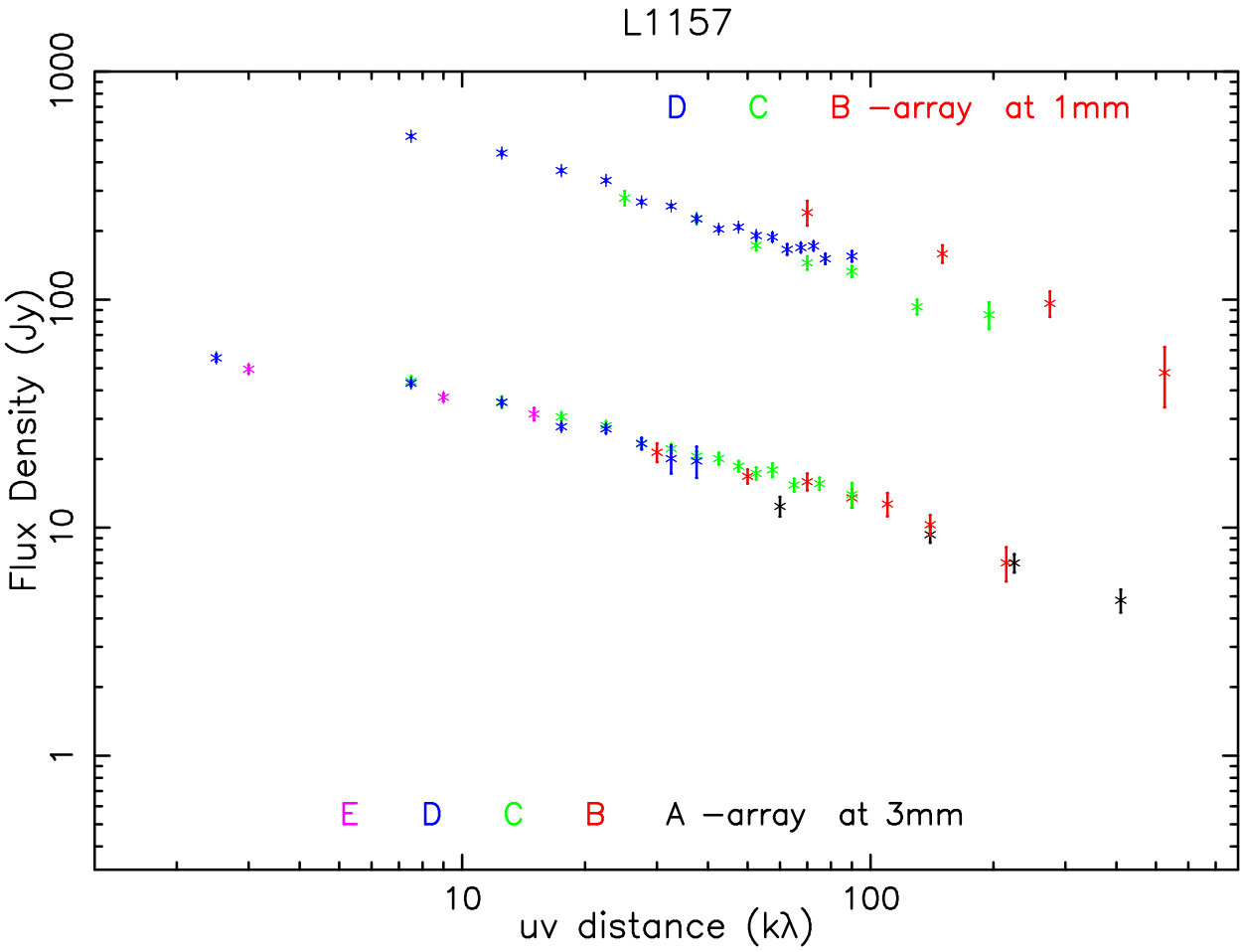

Figure 5.3 Flux density of L1157 dust continuum at 1 mm (*upper*) and 3 mm (*lower*). The visibilities are vector averaged around the source center and binned into u-v annuli. Data collected in different array configurations are plotted separately to showcase the consistency of absolute flux.

scale (0.4″). Although slightly elongated perpendicular to the outflow direction, no apparent disk or flattened structure is seen in the dust continuum at either small or large scale with the current resolution and sensitivity.

5.3 Aspects of Modeling a Class 0 YSO

To compare a YSO model with observations, we consider both the interferometric effects and the physical conditions of the system, including the density and temperature structures and dust grain properties. In the following sections, we discuss the details of each facet in

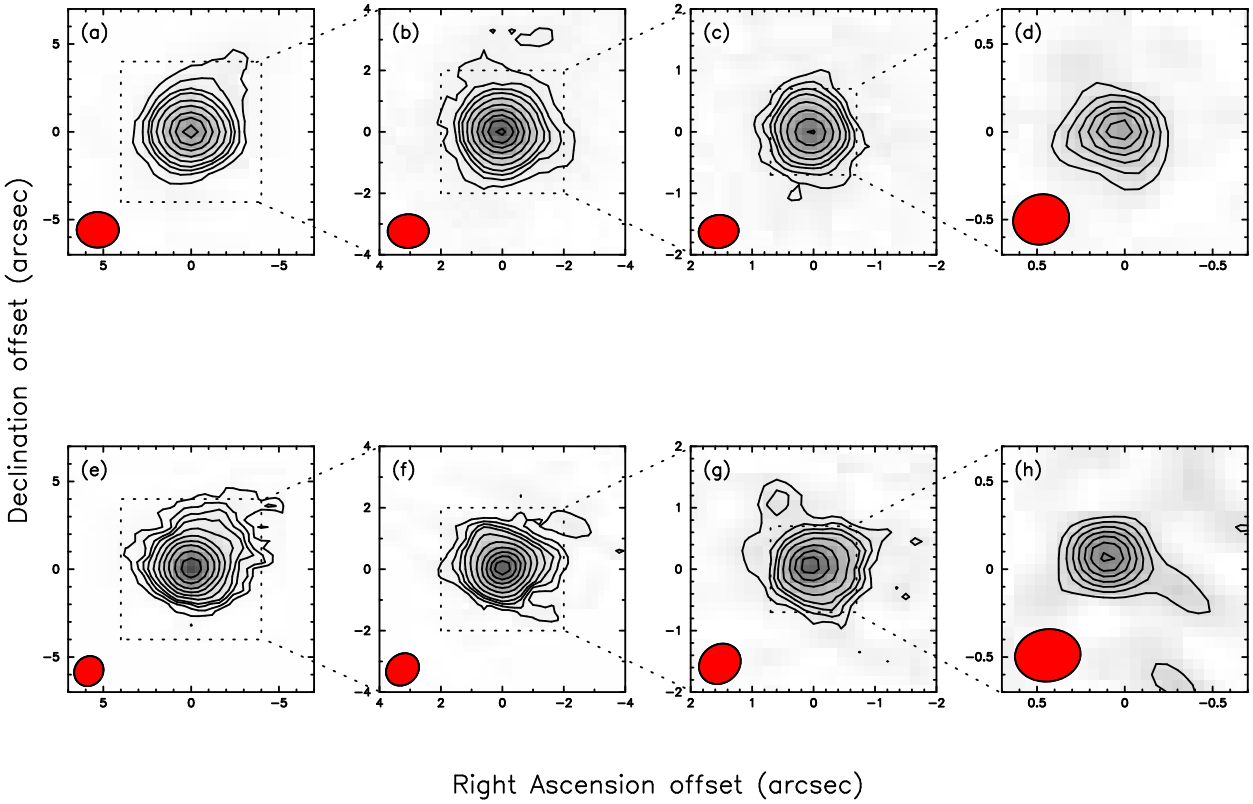

Figure 5.4 CARMA 3 mm (*upper*) and 1 mm (*lower*) dust continuum images of L1157. The same multi-configuration data with different u-v imaging weightings are shown to emphasize structures on different size scales. The contour levels, noise rms (σ), and beams are as follows: (a) [2,3,4,5,7,10,14,18,22]$\times\sigma$, σ = 0.9 mJy beam^{-1}, 2.40″×2.03″ at a position angle of 90°; (b) [2,3,4,5,7,10,14,18,22,26]$\times\sigma$, σ = 0.6 mJy beam^{-1}, 1.34″×1.10″ at a position angle of -88°; (c) [2,3,4,5,7,10,14,18]$\times\sigma$, σ = 0.6 mJy beam^{-1}, 0.65″×0.54″ at a position angle of -82°; (d) [2,3,4,5,6,7]$\times\sigma$, σ = 0.9 mJy beam^{-1}, 0.32″×0.28″ at a position angle of -73°. (e) [2,3,4,5,7,10,14,20,30,42]$\times\sigma$, σ =4.0 mJy beam^{-1}, 1.77″×1.61″ at a position angle of -38°; (f) [2,3,4,5,7,10,14,18,22,26]$\times\sigma$, σ =5.5 mJy beam^{-1}, 1.14″×0.98″ at a position angle of -48°; (g) [2,3,4,5,7,10,13,16]$\times\sigma$, σ = 7.0 mJy beam^{-1}, 0.71″×0.62″ at a position angle of -51°; (h) [2,3,4,5,6,7,8]$\times\sigma$, σ = 12.0 mJy beam^{-1}, 0.37″×0.30″ at a position angle of -83°.

the modeling.

5.3.1 Envelope Structure

A simple Class 0 YSO model consisting of a dusty envelope, a bipolar outflow, and possibly a circumstellar disk is considered. For the envelope structures, we examine a simple power-law density profile, representing self-similar collapse solutions, and a collapse with rotation (Terebey et al. 1984). An unresolved component is included to represent a compact disk structure.

We introduce two cones of emptiness as the bipolar outflow cavity and orientate the envelope geometry with outflow observations: a position angle of 152° for the outflow-axis cut, an inclination angle of 80°, and an opening angle 30° for the outflow cavity are assumed (Choi et al., 1999; Gueth et al., 1996, 1997). For simplicity, the inner and outer radii are fixed to be 12 AU and 10,000 AU, respectively. The inner envelope cavity is smaller than the highest observational resolution, and always within the central cell in the model images. A large outer radius is adopted so there is no ringing effect due to interferometric response on a sharp cutoff in the envelope. Additionally, as the density and temperature are much lower in the outer envelope, precise choice of the outer radius does not play a important role.

5.3.2 Temperature Structure

While many theoretical models ignore the internal heating from the newborn protostar, it is critical to take into account the protostellar contribution to agree with observational luminosity (Adams & Shu, 1985). The heating and cooling of dust grains, dominated by the central illumination and dust grain properties, should be balanced to obtain an equilibrium temperature. To simulate millimeter-wave observations of protostars surrounded by dusty environments, such a realistic temperature distribution need to be either assumed or calculated.

The temperature structure can be approximated assuming simple conditions of the dusty envelope. Assuming a centrally illuminated spherical envelope of which the density has a power-law dependence on radius,

$$\rho(r) = \rho_0 \left(\frac{r}{r_0} \right)^{-p}, \tag{5.1}$$

where ρ_0 is the density at an arbitrary radius r_0 and p is the density power-law index, and assuming a pure power-law dust opacity with a spectral index β, the temperature structure in the optically thin outer envelope can be approximated by

$$T(r) = T_0 \left(\frac{r}{r_0} \right)^{-\frac{2}{\beta+4}} \tag{5.2}$$

(Wolfire & Cassinelli, 1986; Adams, 1991).

Although widely used, Eq. (5.2) may not be a good approximation of the true temperature if that the envelope structure is much deviated from spherical symmetry or a power-law relationship with radius, or if that the dust opacity is much deviated from a power-law relationship with wavelength. While we want to investigate theoretical density profiles not limited to a simple spherically symmetric power-law profile, the approximate temperature is not adequate. Also, the dust opacity is not a power-law with wavelength either. For example, silicate features are apparent at near- and mid-infrared, and the opacity is approximately grey at wavelengths smaller than the grain size. Furthermore, Eq. (5.2) is only valid in the optically thin region and relies on T_0 at r_0. With a fixed central heating source, T_0 at r_0 is characterized by the optically thick-thin transition zone, and is difficult to estimate without a good understanding of the optically thick inner region. Figure 5.5 illustrates how the temperature profile changes as the envelope mass changes, due to the dependency between mass and optical depth. Difference of a few degrees at the outer envelope can result in more than 10% difference in sub-millimeter flux.

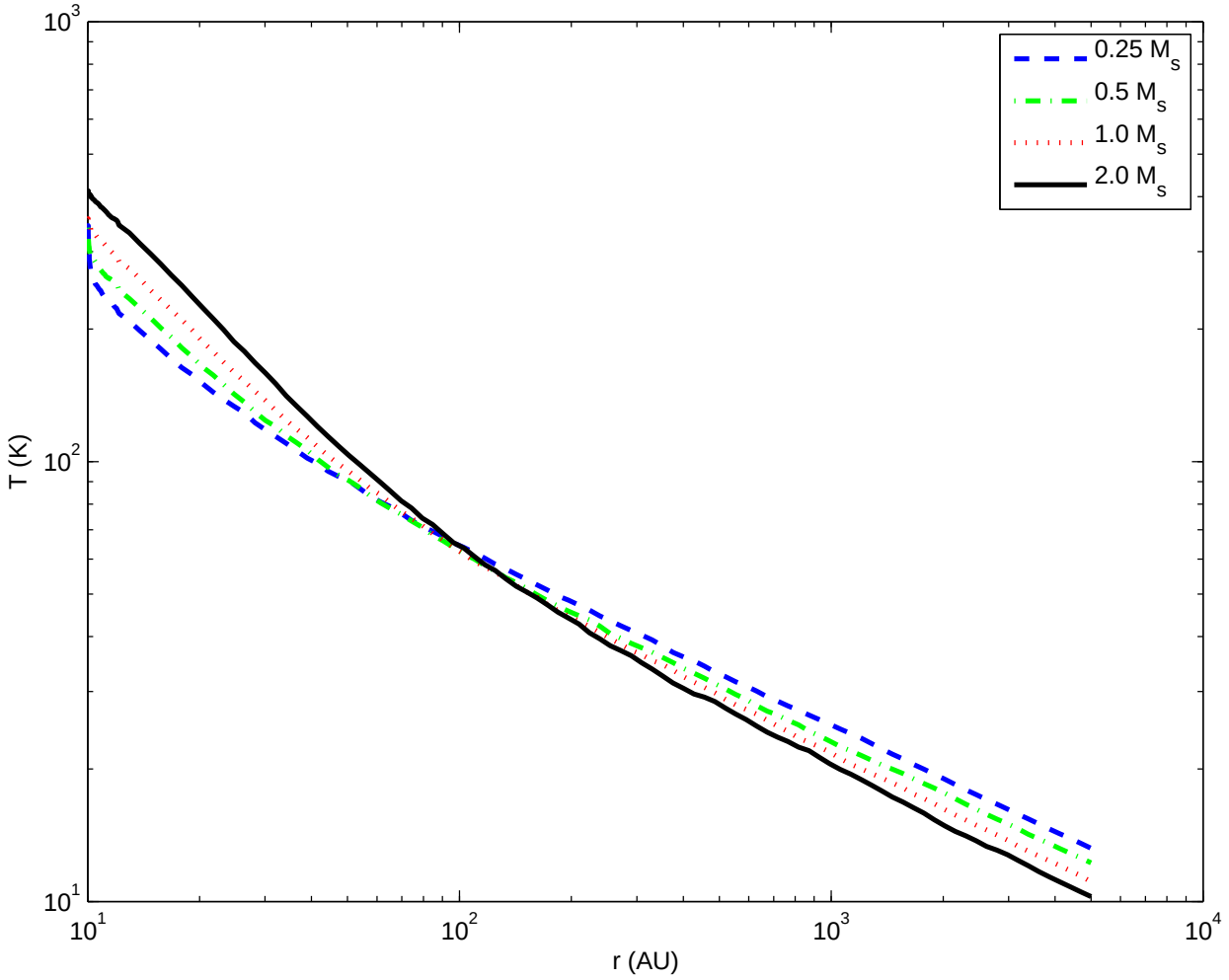

Figure 5.5 Dust temperature distribution of a spherical envelope with a power-law of -1.7 density profile, estimated by Monte Carlo radiative transfer calculations. The envelope model has carbonaceous-silicate grains between an inner radius of 10 AU and an outer radius of 5000 AU, heated by a 10 $L_\odot$ inner source. Total envelope masses are 0.25, 0.5, 1.0, and 2.0 $M_\odot$ for the dashed, dash-dot, dotted, and solid lines, respectively. The more massive the envelope, the larger radius at which it becomes optically thin. A power-law relationship is a good approximation in the outer optically thin region, but not in the inner optically thick region. A power-law fit to the temperature of the outer envelope (r > 100 AU) yields indices of -0.403, -0.413, -0.436, and -0.461 for the four envelope masses, respectively. This test demonstrates the difficulty in assuming a common power-law temperature profile as in Eq. (5.2) with changing envelope parameters.

Given the difficulty to approximate the temperature structure with a variety of envelope models and ranges of model parameters, we calculate a self-consistent temperature distribution for each set of parameters using a Monte Carlo radiative transfer code. We use the RADMC-3D package developed by C. P. Dullemond and co-authors (Dullemond & Dominik, 2004) [4]. For L1157, we adopt a luminosity of 8.4 $L_\odot$ from the source's bolometric luminosity in Froebrich (2005)'s catalog. In the radiative transfer calculation, the total luminosity is divided into photon packages and reprocessed by dust grains. As the scattering efficiency of dust grains is proportional to λ^{-4} at Rayleigh regime and much smaller than absorption, we ignore scattering for computational efficiency. Also, a constant gas-to-dust ratio of 100:1 is assumed.

With the radiative transfer tool, we can examine how temperature structure is affected by other model parameters. For instance, we find that the temperature structure is mostly determined by dust opacity (see next section) at short wavelengths. The dust property at long wavelengths, such as the submillimeter opacity spectral index β, plays a less important role (Chandler et al., 1998).

5.3.3 Dust Grain Properties

Dust grains properties such as chemical composition, geometry, alignment, degree of ionization, and size distribution play important roles in star-forming processes from aspects of thermodynamics, grain surface chemistry, to timescales of magnetic field effects. They are fundamental for interpreting observations of extinction and emission. For dust grains in diffuse interstellar medium, the classic model constructed by Mathis et al. (1977, hereafter MRN) with optical constants calculated by Draine & Lee (1984) has remarkably reproduced the interstellar extinction and polarization observations from infrared to ultraviolet wavelengths. The MRN model is composed of graphite and silicate grains with a power-law size distribution $dn \propto a^{-3.5} da$, where a is the grain size ranging from 50 Å to 0.25 μm. However,

[4] http://www.ita.uni-heidelberg.de/~dullemond/software/radmc-3d/

for dust grains in dense cores and star forming regions, collision and interaction between grain particles become more important. Ossenkopf & Henning (1994) has considered the dust coagulation process in dense protostellar cores and found that the opacity can be enhanced by a factor of a few as grains aggregate. The authors started with the MRN grains covered with different amount ice mantles, and investigated the optical constants after 10^5 yrs of coagulation in gas density ranging from 10^5 to 10^8 cm^{-3}. The dust opacity, or the mass absorption coefficient κ defined as the cross section per unit mass, is plotted as a function of wavelength in Figure 5.6.

In our modeling, we adopt κ values from the column 5 of Table 1 in Ossenkopf & Henning (1994), the so-called the OH5 grain which is covered by a thin layer of ice mantle and coagulated at 10^6 cm^{-3}. Besides being widely used, the OH5 model shows agreements with and in some cases favored by multi-wavelength observations of star-forming regions (e.g., van der Tak et al., 1999; Evans et al., 2001; Shirley et al., 2005, 2011a). Despite uncertain, the dust opacity used in the analysis substantially affect the deduced SED as well as temperature structure of YSOs.

At far-infrared and millimeter wavelengths, κ can be approximated as a power law with respect to frequency

$$\kappa = \kappa_0 \left(\frac{\nu}{\nu_0} \right)^{\beta}. \tag{5.3}$$

The dust opacity spectral index β, which can only be studied with multi-wavelength observations, varies with environment and is related to grain properties mentioned previously. β is about 2 in the diffuse interstellar medium and starless cores (e.g., Draine & Lee, 1984; Schnee et al., 2010), but significantly lower in protoplanetary disks ($\beta \lesssim 1$, e.g., Beckwith & Sargent, 1991; Natta et al., 2007; Ricci et al., 2010b). One explanation of the lower β is a larger grain size, as $\beta = 0$ implies grain size larger than the observed wavelength (grey opacity). In order to better determine the dust property of L1157, we include β as a model parameter. Based on the OH5 model, we modify the opacity curve with a power-law of index

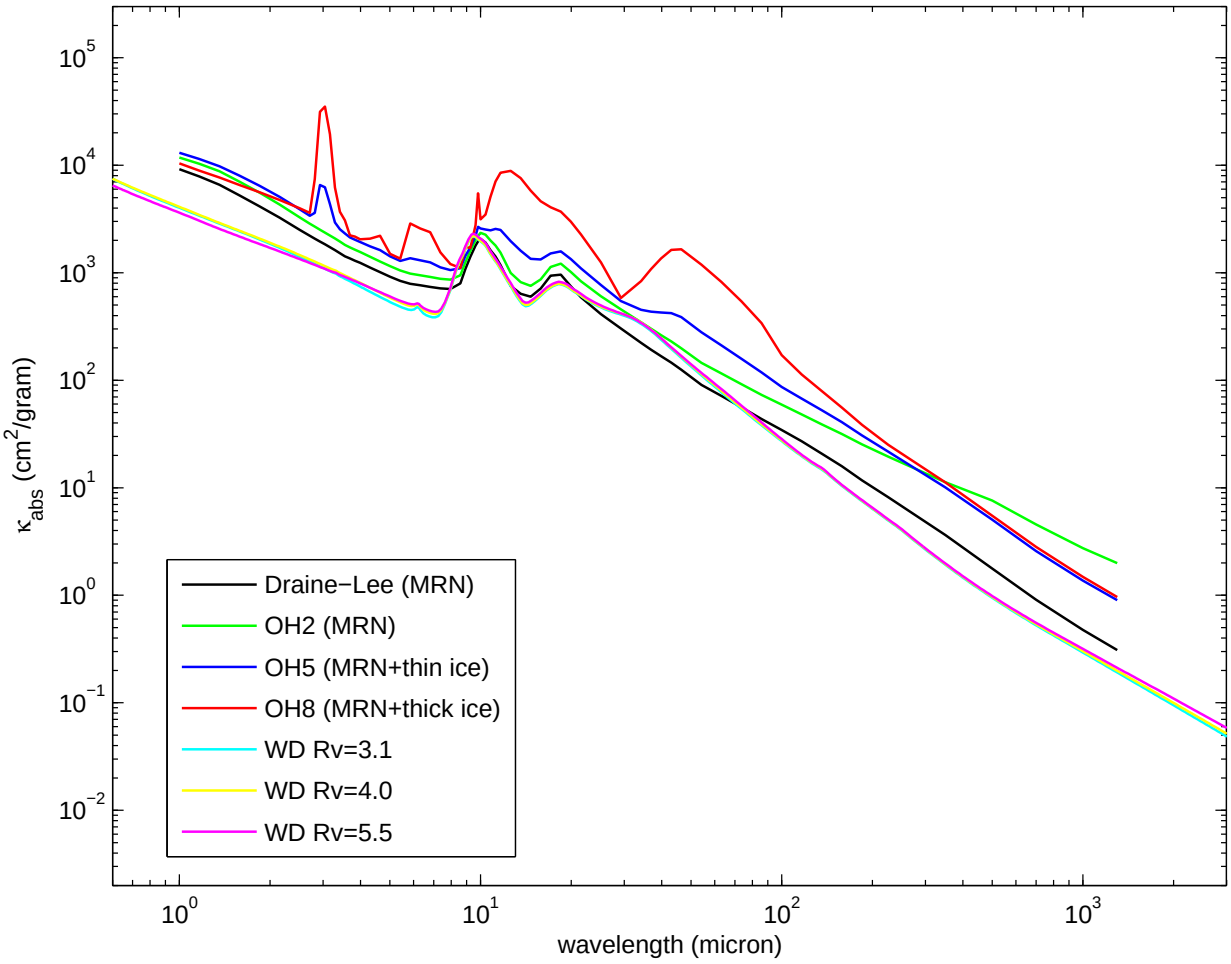

Figure 5.6 Dust opacity κ as a function of wavelength. The grain models are: Draine-Lee: Draine & Lee (1984) based on MRN; OH: the coagulated grains in Ossenkopf & Henning (1994) with different amount of coated ice; and WD: the updated version of Weingartner & Draine (2001) with various R_V, the ratio of visual extinction to reddening ($A(V)/E(B-V)$). The Draine-Lee model and WD model are suitable for diffuse interstellar medium, while the OH model are for dense cores.

β as in Eq. (5.3) at wavelengths longer than an arbitrary choice of 700 μm.

For simplicity, we assume uniform grain properties in the envelope model. In other words, κ is only a function of frequency and independent of radius. Although dust properties must differ when physical conditions such as temperature change and β has been suggested to have a radial dependence at some YSOs (Kwon et al., 2009; Isella et al., 2010), β at L1157 does not seem to show obvious radial variation. Figure 5.7 shows the approximate dust opacity spectral index β_{thin} with the optically thin assumption and Rayleigh-Jeans approximation. In this limit, $F_\nu \propto \kappa_\nu B_\nu \propto \nu^{\beta+2}$ and β_{thin} is estimated using flux ratio of the annuli-averaged visibility at each u-v distance bin. No strong radial dependence is suggested.

5.3.4 Modeling Procedure

Given a set of model parameters, we run another radiative transfer calculation to estimate the sky brightness distribution, the so-called ray-tracing calculation, for the dust continuum. The density and self-consistent temperature distributions in three dimensions are considered along with the model dust property. Essentially, for each pixel on the plane of sky, the flux is calculated by integrating the dust emission along the line of sight (e.g., Adams, 1991). Assuming no background brightness, the specific intensity can be expressed as

$$I_\nu = \int_{los} B_\nu(T)\, e^{-\tau_\nu}\, \mathrm{d}\tau_\nu = \int_{los} B_\nu(T(\vec{r}))\, e^{-\tau_\nu(\vec{r})}\, \rho(\vec{r})\, \kappa_\nu\, \mathrm{d}\vec{r}, \tag{5.4}$$

where $B_\nu(T)$ is the Planck function at dust temperature T, ρ is the envelope density, $\vec{r}$ denotes the position, and τ_ν is the optical depth from the position $\vec{r}$ along the line of sight to the observer

$$\tau_\nu(\vec{r}) = \kappa_\nu \int_{los} \rho(\vec{r}) d\vec{r} = \kappa_\nu \int_l^\infty \rho(\vec{r}) dl'. \tag{5.5}$$

T, ρ, and τ_ν are all dependent of $\vec{r}$.

With the model sky brightness, we simulate interferometric observations and generate

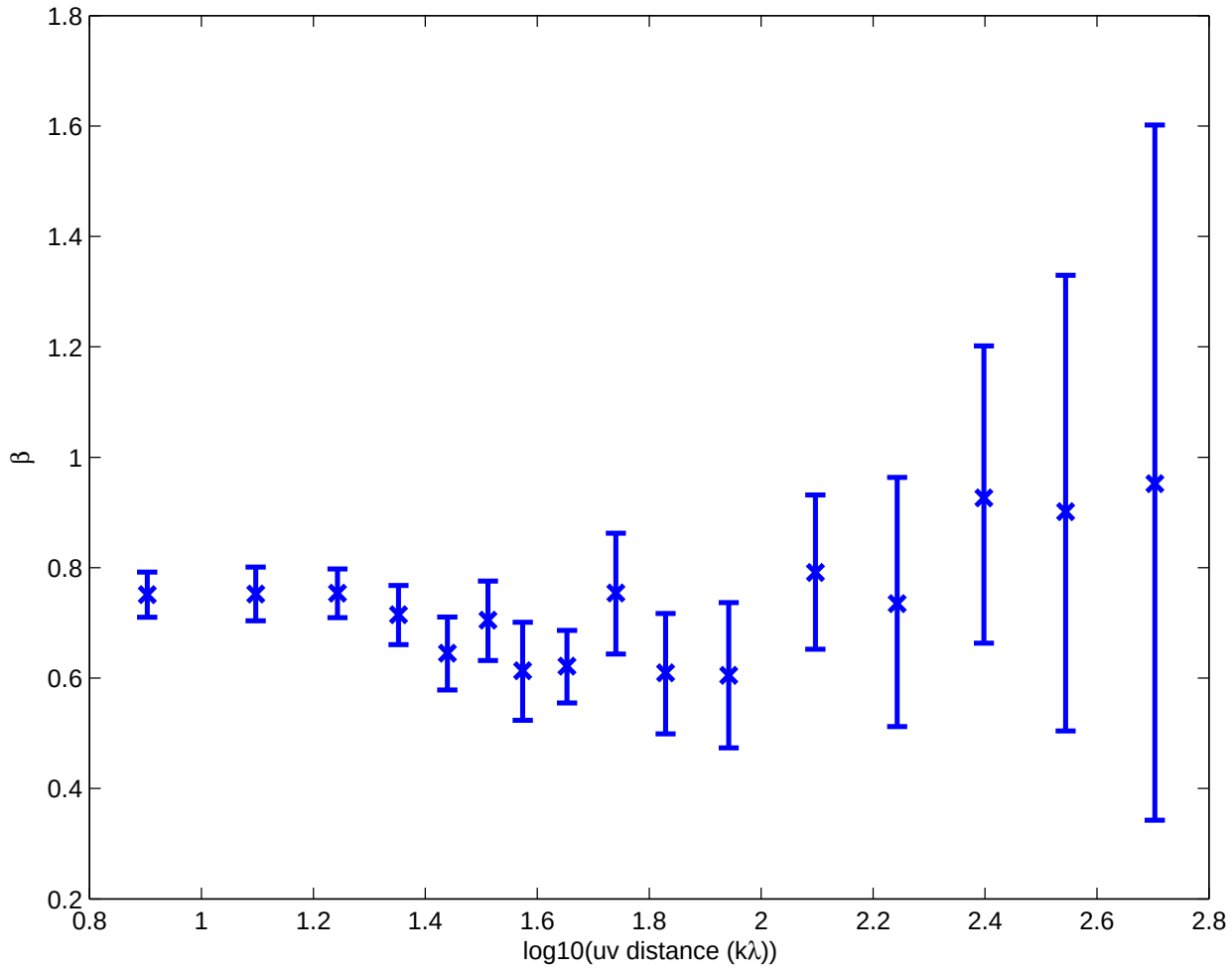

Figure 5.7 Approximate dust opacity spectral index β_{thin} of L1157 assuming optically thin condition. The error bars show statistical uncertainty only and do not include uncertainty from flux calibration.

model visibilities. The sky image is convolved with the primary beam patterns of the antennas and then Fourier transformed into visibilities with the observational u-v sampling. In the case of 15-element CARMA, the 6.1-meter BIMA dishes and 10.4-meter OVRO dishes give 3 types of baselines. Therefore we construct separate primary-beam-corrected images for each kind of baseline, and sample the images with corresponding u-v spacing for each data visibility from real observations. In addition, images at two wavelengths are constructed individually based on the same model.

Model visibilities are compared with observational data at each u-v sample and wavelength. The analysis is done in the visibility domain so as to avoid the complexity brought by the CLEAN algorithm, u-v sampling, and imaging process. Some information is lost in the image domain through the imaging process, since structures in images can be sensitive to beamsize or weighting. In other words, emission at different size scales can either be emphasized or suppressed, causing biases in the model-data comparison. Furthermore, visibilities are compared data point by data point. No binning nor averaging are done which preserves any asymmetric structures.

5.3.5 Fitting Technique and Statistical Analysis

This section describes our statistical approach to evaluate the goodness of fits, and our technical procedure to characterize model parameters and their uncertainty.

Assuming the noise from observations are normally distributed or Gaussian noise, the goodness of a fit can be characterized by the standard chi-square statistics. Real and imaginary parts of each visibility point are considered individually without any averaging on the u-v plane, as in

$$\chi^2 = \sum_i \frac{(Re(V_{model,i}) - Re(V_{data,i}))^2 + (Im(V_{model,i}) - Im(V_{data,i}))^2}{\sigma_i^2} \tag{5.6}$$

where i stands for each visibility point at its unique u-v. The noise of each visibility σ is

square root of data variance (outputted by MIRIAD task uvinfo) multiplied by a scaling factor to account for imperfect weather conditions. The noise level before the scaling follows

$$\sigma_o = \frac{2k_b T_{sys}}{\eta_a \eta_c A \sqrt{N(N-1)\Delta\nu t_{int}}}, \tag{5.7}$$

where k_b is the Boltzmann's constant, T_{sys} is the system temperature, η_a is the aperture efficiency, η_c is the correlator efficiency, A is the antenna collecting area, N is the number of antennas, $\Delta\nu$ is the bandwidth, and τ is the on-source integration time.

The scaling factor is used to correct σ for the phase decorrelation and determined by the phase scatter in each array configuration at each wavelength. This factor is around 1 in good weather conditions at compact array configurations, and should be always larger than 1. In other words, we only adjust σ to make data less constraining.

We use the Bayesian approach to compare model with data. Bayesian inference has been widely used in astronomy, from fields in exoplanets to cosmology, as well as applications in star formation (e.g., Ford, 2005; Spergel et al., 2007; Crutcher et al., 2010). The main concept of Bayesian inference is to incorporate prior knowledge on the hypothesis. Also, information is represented in terms of probability density function (PDF) in parameter space. Mathematically, given the observed data, the posterior probability of model parameters can be specified by the Bayes' theorem

$$P(x|D,M) = \frac{P(D|x,M)P(x|M)}{P(D|M)} \tag{5.8}$$

where x stands for model parameters, D stands for data, M denotes a particular model with its model assumptions and other background information, $P(x|M)$ is the prior probability of the model parameters, $P(D|x,M)$ is the conditional probability or the likelihood of data given the model with parameter x, and $P(D|M)$ is the evidence or global likelihood. The evidence $P(D|M)$ is the net probability of the data given the model, as it sums the product

of likelihood and prior over parameter space:

$$P(D|M) = \int P(D|x, M)P(x|M)dx. \tag{5.9}$$

The evidence is independent of the parameter values and can be seen as a normalizing factor in Eq. (5.8); therefore it is not important for parameter estimation of a single model. For the same reason, the model label M is sometimes omitted when only one model is considered.

Whether to view a statistics problem with Bayesian or frequentist approach is under debate. The disputes are beyond the scope of this study and more discussions can be found in Loredo (1990, 1992). Nevertheless, in the case of a uniform prior, the method of using the posterior probability is equivalent to maximum likelihood estimate as far as identifying the best-fit parameter values is concerned. As for full parameter estimation including of estimating the parameter errors, different approaches are adopted for Bayesians and frequentists, and will be discussed later.

The likelihood of data given the model is characterized by χ^2 as defined in Eq. (5.6) and $P(D|x) \sim \exp(-\chi^2(x, D)/2)$ with model parameter x and observational data D. Therefore the most probable parameters with the maximum likelihood can be obtained by locating the global minimum of χ^2. We use the Nelder-Mead simplex algorithm as implemented in MATLAB with bound constraints to search for the minimum. Besides fast convergence, this method does not evaluate function derivative, which suits our application because fewer modeling evaluations are required. Several starting points are used to look for several convergent minimums, and they are checked to be consistent with each other. This is to make sure that what is found is the global minimum, not local minimum.

Once the best-fit parameter values are identified, efforts are made to characterize the uncertainty. The essence of parameter estimation is to characterize the reliability of an estimate on model parameters under the assumption that the best-fit model is correct. In other words, the best-fit model needs to show statistical significance based on a hypothesis

test before any of the following parameter estimation can make sense. For example, in the standard Pearson's chi-square hypothesis test, χ^2 value of the model needs to be smaller than a critical value depending on the degrees of freedom to reject the null hypothesis. In the following I discuss two common methods of parameter estimation: (1) a frequentist approach to characterize $\Delta\chi^2$ and infer statistical significance, and (2) Markov chain Monte Carlo (MCMC) in the context of Bayesian inference.

The frequentist $\Delta\chi^2$ statistics has been suggested in Lampton et al. (1976) and Avni (1976), and summarized in Press et al. (2002). With the definition of $\Delta\chi^2(x) = \chi^2(x) - \chi^2(x_{best\text{-}fit})$, $\Delta\chi^2(x)$ is chi-square distributed with p degrees of freedom, where p is the number of fitted parameters or parameters of interest. Then the level of confidence can be estimated according to the chi-square distribution. Although it relies on the validity of the best-fit model, the exact value of $\chi^2(x_{best\text{-}fit})$ is not important for parameter estimation. The $\Delta\chi^2(x)$ statistics is independent of the Pearson's chi-square test and $\chi^2(x)$ statistics, and focuses on the variation of $\chi^2(x)$ in parameter space x. A common way to illustrate the results is through iso-chi-square contours or hyper-surface in multi-dimensional parameter space as the confidence region. In the case that only partial parameters are of interest, the remaining nuisance parameters should be varied to minimize $\Delta\chi^2(x)$ instead of direct projections. (c.f. In Bayesian inference, the nuisance parameters are marginalized over.) For example, when only one parameter is of interest, $\Delta\chi^2(x)$ is distributed as a chi-square distribution with one degree of freedom. The 68% confidence interval corresponds to the region bounded by $\Delta\chi^2(x) = 1$.

Despite the controversy over the flaws of applying this method with nonlinear models (Loredo, 1992), estimating $\Delta\chi^2(x)$ over a large parameter space can be computationally difficult. A grid on parameters or equivalent technique is required. The large number of evaluations usually makes this method impractical, especially when the number of parameters is large (Ford, 2005).

On the other hand, MCMC offers a very efficient way to estimate the posterior prob-

ability in Bayesian inference, compared to any other methods that require grid searching. Rather than minimizing on each grid point and probing the variation of $\chi^2(x)$, the posterior probability respect to parameters of interest is estimated through marginalization over all other parameters. For example, given a PDF $P(x_1, x_2|D)$ where x_1 is the parameter of interest and x_2 is a nuisance parameter, the x_2 space is integrated over according to probability to obtain the marginalized PDF, as in

$$P(x_1|D) = \int P(x_1, x_2|D)dx_2 = \int P(x_1|x_2, D)P(x_2|D)dx_2. \tag{5.10}$$

At first glance, a straightforward marginalization can be very computationally extensive, similar to the necessity of a grid evaluation in frequentist methods. However, marginalized results can be obtained efficiently with MCMC. One of the reasons is that it searches the parameter space according to probability and the parameter space with low probability is less explored and sometimes not probed at all.

The Metropolis-Hastings algorithm of the MCMC method is utilized to construct the Markov chain. Markov chain is a sequence of parameter values representing the system and characterized by a transition probability that controls the random process from one state to another. The transition probability and the next state are only dependent of the current state, but not any previous states. Regardless of the starting state, the chain eventually converges to a stationary or equilibrium distribution according the PDF. We use the Metropolis-Hastings algorithm to draw the sample and construct the chain. This algorithm uses a proposal distribution $q(x'|x)$, or the candidate transition probability distribution function, to generate a trial state x' based on the current state x. Then the proposed state is randomly accepted with the acceptance probability

$$\alpha(x'|x) = \min\left[\frac{P(x'|D)q(x|x')}{P(x|D)q(x'|x)}, 1\right], \tag{5.11}$$

or otherwise rejected. The arrangement results in a transition probability

$$T(x'|x) = q(x'|x)\alpha(x'|x) \tag{5.12}$$

which is reversible ($\pi(x)T(x'|x) = \pi(x')T(x|x')$, where $\pi(x)$ is the equilibrium probability at state x) and irreducible (possible to go from any state to any state). As introduced earlier, $P(x|D)$ is the posterior PDF given the observational data, and approximately proportional to $\exp(-\chi^2(x, D)/2)$ with flat prior. Practically, $\chi^2(x, D)$ is evaluated at each proposed state change.

The Metropolis-Hastings algorithm assures that the chain converges to $P(x|D)$ as the sample number is large. The convergence rate is related to the choice of $q(x'|x)$. A typical choice is a Gaussian function centered around x, that is,

$$q(x'|x) = \frac{1}{\sqrt{2\pi w^2}} \exp\left(-\frac{(x' - x)^2}{2w^2}\right) = q(x|x'). \tag{5.13}$$

The width of the Gaussian, specified by w, determines the trial step size. If the step size is too large, most trial states are rejected so the calculation becomes very inefficient; if the step size is too small, the chain behaves like a random walk and requires a long time to converge. An optimal acceptance rate is suggested to be around 0.23 for multi-dimensional parameter space (Gelman et al., 2004). The choice of a symmetric proposal distribution also reduces the acceptance probability into a simper form

$$\alpha(x'|x) = \min\left[\frac{P(x'|D)}{P(x|D)}, 1\right] = \min\left[\exp\left(\frac{\chi^2(x, D) - \chi^2(x', D)}{2}\right), 1\right]. \tag{5.14}$$

The posterior probability is obtained with a converged Markov chain, as its density of points in parameter space follows the posterior probability of the parameters. Marginalization is done through projecting the Markov chain to the space of parameters of interest. We estimate the 68% and 95% confidence limits and the corresponding standard deviation

based on the simulated MCMC. Specifically, the 68% or 1 σ confidence limit encloses 68% of accepted points along the Markov chain, and represents the region containing 68% of the total probability distribution. We also report the expectation value of each parameter, weighted by the posterior marginalized probability as in

$$\langle x_i \rangle = \int P(x_i|D) x_i dx_i = \frac{1}{N} \Sigma_j x_{i,j} \tag{5.15}$$

where j denotes the points in the Markov chain and N is the total number of points. The expectation values from the marginalized distributions do not need to be identical to the parameters with the maximum likelihood, because we are projecting the values from a high dimensional distribution which may not be a multivariate Gaussian; however, they should be consistent.

Note that the deduced parameters are valid only within the framework of model assumptions. Evaluating the goodness of a model and comparisons between models will be discussed in §5.5.4.

5.4 Results

In this section, the modeling results using the procedures detailed in §5.3 are presented. Several models are considered and shown individually.

5.4.1 Spherical Power-law Envelope Model

We first consider a spherical envelope with a power-law density profile and self-consistent temperature structure. In this simplest model, three model parameters are included: (a) the dust opacity spectral index β as in Eq. (5.3), (b) a mass scaling factor representing the total envelope mass, and (c) the density power-law index p as in Eq. (5.1). All other model properties are fixed as described in §5.3.

Table 5.2. Power-law Envelope Model

parameter	Mean	Radius of the 68% confidence interval (statistical noise only)	(with flux uncertainty)
dust opacity spectral index β	0.84037	1.4×10^{-4}	0.11
envelope mass (in $M_\odot$)	1.8120	1.3×10^{-3}	0.38
density power-law index p ...	2.00939	2.0×10^{-4}	0.03

We begin with only considering the statistical noise of data visibility and ignoring the uncertainty of absolute flux. A global minimum of χ^2 is searched and verified to be a good fit with a chi-square hypothesis test. Then, MCMC is calculated to characterize the uncertainty of parameter estimation. Table 5.2 lists the expectation values and uncertainties of all parameters, and Figure 5.8 shows the the marginalized posterior probability distributions in 1-D and 2-D parameter space. The 68% and 95% confidence regions are shown by 2-D contours to reveal any correlation between parameters. As shown by the marginalized contours in the p-mass plane in Figure 5.8 (lower row, middle column), a correlation between the density power-law index p and envelope mass is implied. This is because a steeper density profile means more material having a higher temperature in the inner envelope, resulting in more flux with the same amount of total material.

The parameters are determined with a high precision within the framework of model assumptions. The narrow uncertainties can be understood since approximately five million independent data visibilities are used to fit only three model parameters. Strong assumptions are imposed in the model. Similar results have been obtained in other studies as well. For example, Kwon et al. (2011) have taken the Bayesian approach to estimate model parameters and their errors in the applications of T-Tauri disks, and small uncertainties are obtained when only the statistical errors in the data are considered.

However, the absolute amplitude uncertainty, originated by the absolute flux calibration in the data reduction process, brings more uncertainties to the model parameter estimation.

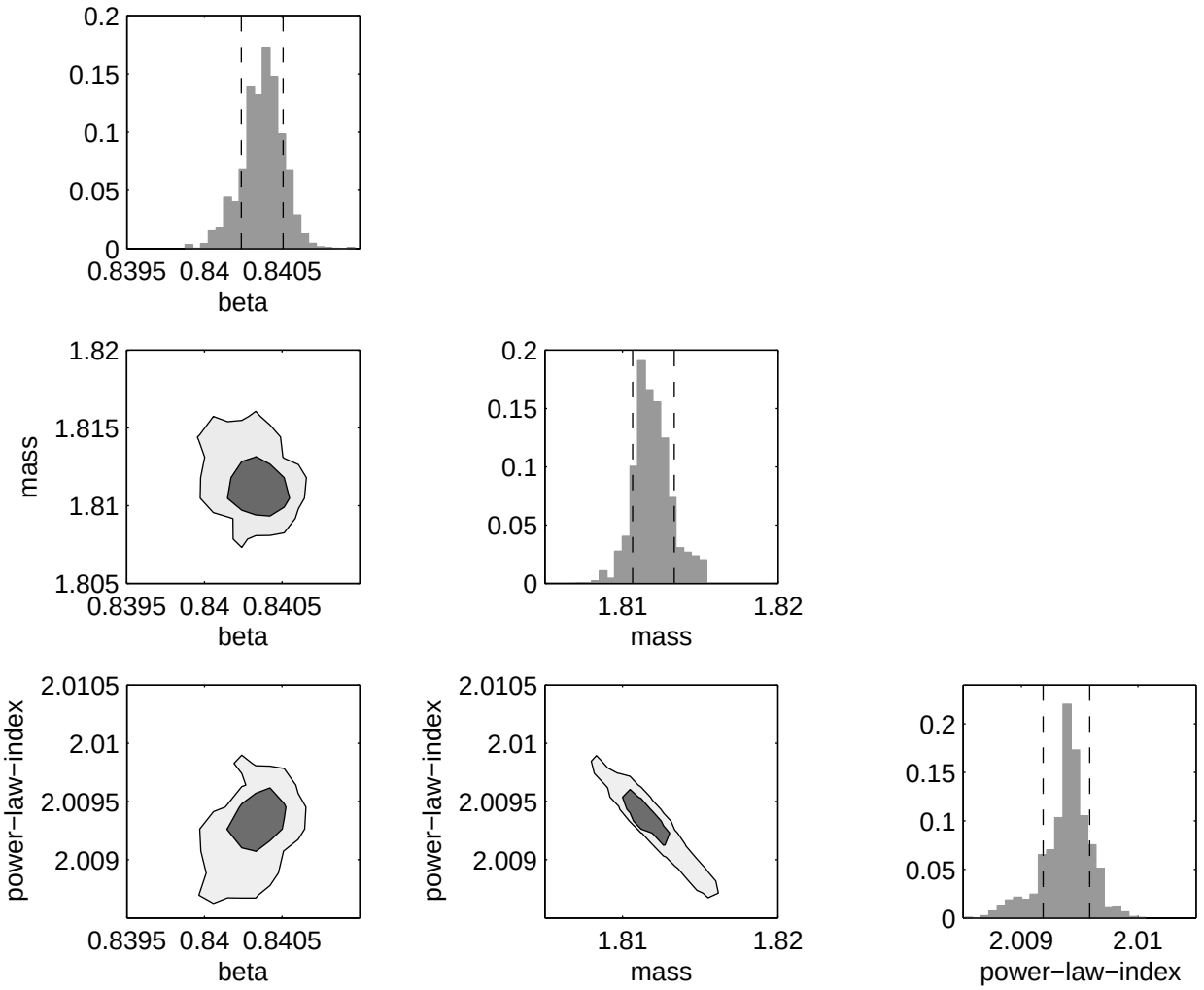

Figure 5.8 Marginalized posterior probability distributions for all three parameters (dust opacity spectral index β, envelope mass, and envelope density power-law index p) of the power-law envelope model. In the histograms, the dashed vertical lines enclose 68% or 1 σ confidence interval, with the expectation values and σ listed in Table 5.2. The dark and light areas in the 2-D contour plots are the 68% and 95% confidence regions. Only the statistical errors are considered for the data.

As we have verified that the calibrator flux is consistent among all observational tracks at multiple array configurations, the absolute flux errors effectively cause a uncertain scaling to the whole data at each wavelength. Therefore, the absolute flux uncertainty can play a dominating role in estimating frequency-dependent parameters, but cause minimal effects at the relative spatial structures probed at one single wavelength.

Marginalization in the framework of Bayesian statistics allows us to quantitatively take the absolute flux uncertainty into consideration. We introduce two additional nuisance parameters, S_{1mm} and S_{3mm}, to scale the absolute amplitude of all data at 1 mm and 3 mm, respectively. $S_{1mm} = 1$ and $S_{3mm} = 1$ means no scaling is done, as in the presented dataset. Since the main uncertainty of flux calibration results from the choice of planetary models and no model is preferred, a flat probability distribution for both S_{1mm} and S_{3mm}, ranging from 0.9 to 1.1, is assumed. The range of the scaling factors is chosen to be consistent with the commonly quoted 10% errors for the absolute flux calibration. Our approach is similar to the method of Lay et al. (1995).

Figure 5.9 shows the marginalized posterior probability distributions of model parameters with consideration of the absolute flux uncertainty. The uncertainties of parameters are listed in Table 5.2 column 4. Inclusion of absolute flux uncertainty increases the parameter errors by a factor of 2-3 order of magnitude, and it is critical for parameter estimation as it makes data much less constraining. In particular, the dust spectral index β is mostly determined by the flux ratio between 1 mm and 3 mm, hence it becomes much more uncertain due to the uncertainty of absolute amplitude.

For additional visualization, visibilities are averaged vectorially and binned in u-v annuli around the source center, and shown as a function of u-v distance in Figure 5.10. Both the observational data of L1157 and the model calculated with the marginalized parameters are shown as an *a posteriori* comparison. Note that visibility data are not averaged in the modeling process. Also, the error bars in Figure 5.10 show the standard deviation of data visibilities in the u-v annuli, which is different from the data uncertainty used in the modeling

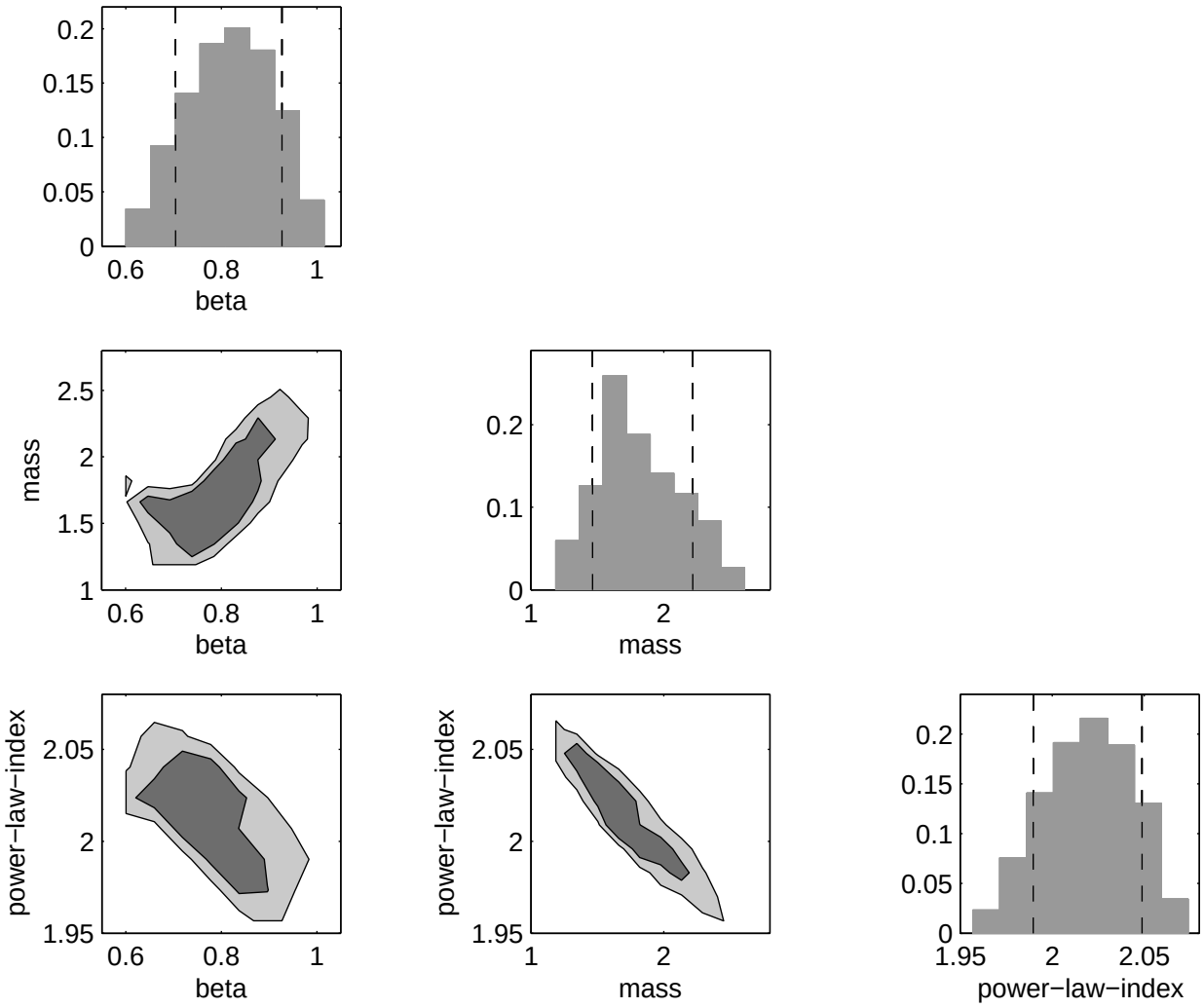

Figure 5.9 Same as Figure 5.8 but with the consideration of the absolute flux uncertainty. Marginalized posterior probability distributions for all three parameters (dust opacity spectral index β, envelope mass, and envelope density power-law index p) of the power-law envelope model are shown. In the histograms, the dashed vertical lines enclose 68% or 1 σ confidence interval, with the expectation values and σ listed in Table 5.2. The dark and light areas in the 2-D contour plots are the 68% and 95% confidence regions.

process.

Figure 5.11 and Figure 5.12 continue the *a posteriori* check and compare the model with the data in the image domain for the 3 mm and 1 mm dust continuum, respectively. The model visibilities are calculated with the marginalized parameters, corrected by the primary beam effect according to CARMA antennas, and sampled as in the actual data. We image the model visibilities in the same way the data visibilities are imaged as shown in Figure 5.4, that is, the same sets of u-v imaging weightings are used for showing structures at four size scales at each wavelength. Residuals in the visibility domain are also imaged and shown in Figure 5.11 and Figure 5.12 to demonstrate the fitting error in the image space. The subtraction of model from data leaves no residuals greater than 3 σ level at the 3 mm images, confirming that a good fit is obtained. In the large-scale image of 1 mm continuum, the residuals extend towards the north-west of the protostar, which aligns with the outflow direction and is likely due to the asymmetric structure from the outflow. In the small-scale image of 1 mm continuum, a 3 σ peak is seen at the north-east of the protostar, which can be caused by the differences of the emission peak position measured using 1 mm and 3 mm data. We estimate the protostar position by fitting a Gaussian to the highest resolution observations at 3 mm, and there is a slight offset to the protostar position measured using 1 mm data.

The posterior-weighted results suggest a density power-law index $p \sim 2$. In this case, the envelope density structure is similar to a singular isothermal sphere or the beginning stage of the Shu model with a very small infall region. In the Shu model, a free-fall-like $p \sim 1.5$ profile is established quickly during the collapse process. If the Shu model is applied strictly, an extremely young age of $\sim 10^3$ yrs is implied. This age is much younger than other age estimate. For example, a kinematic age of $\sim$15,000 yrs is suggested by the outflow observations (Bachiller et al., 2001). The results are consistent with the single-wavelength study of Looney et al. (2003), in which a larger sample of Class 0 YSOs are modeled and unphysical young ages are derived using the simple self-similar model. A steep density

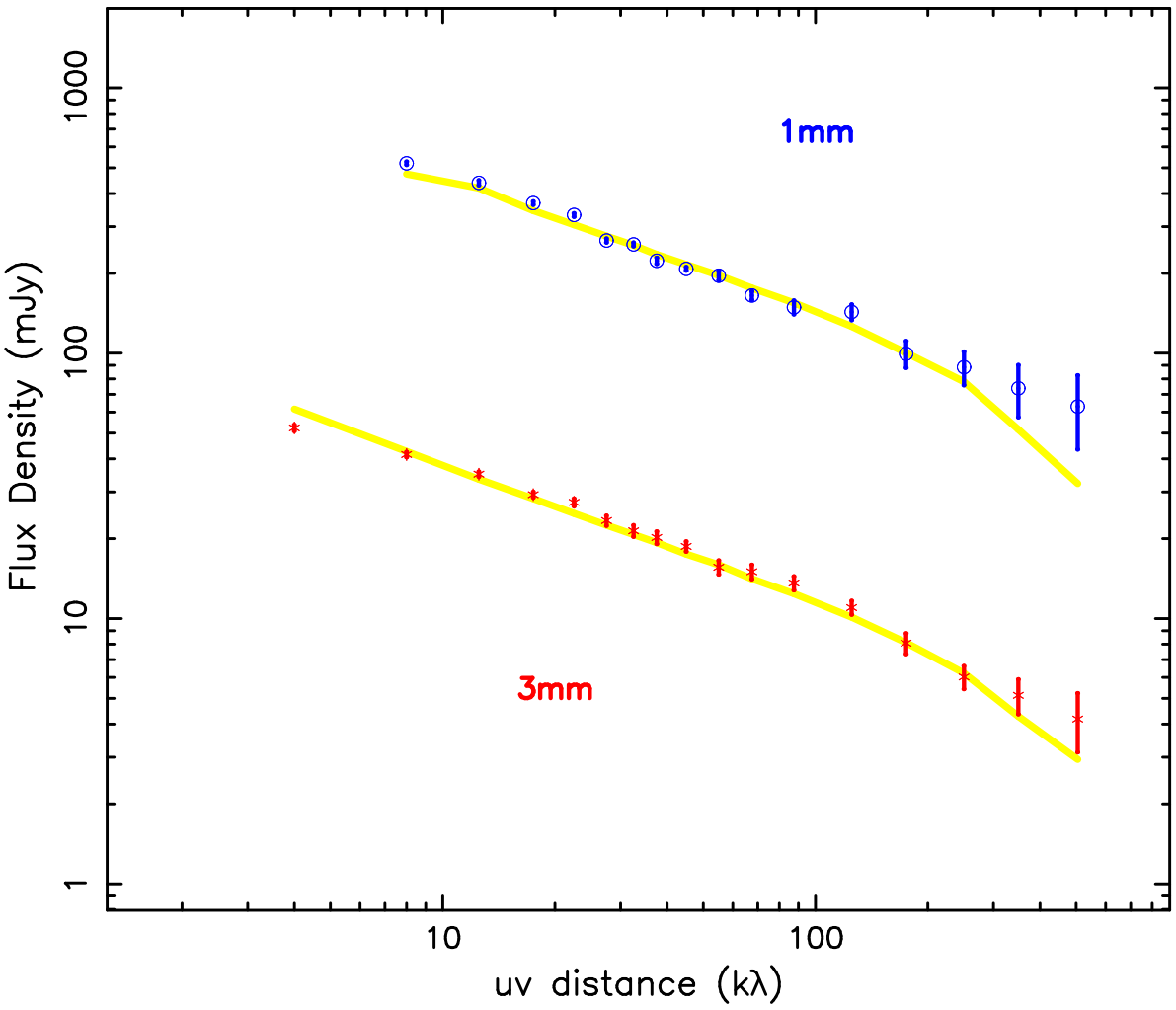

Figure 5.10 Flux density of the observational data (circles for 1 mm data and asterisks for 3 mm data) and the model fit (solid lines) with the marginalized parameters for the power-law envelope model. While modeling is done with non-averaged visibilities, annuli-averaged visibilities are shown as a function of u-v distance. Error bars are statistical errors in the annuli-bins only and different from the visibility uncertainty used in the modeling.

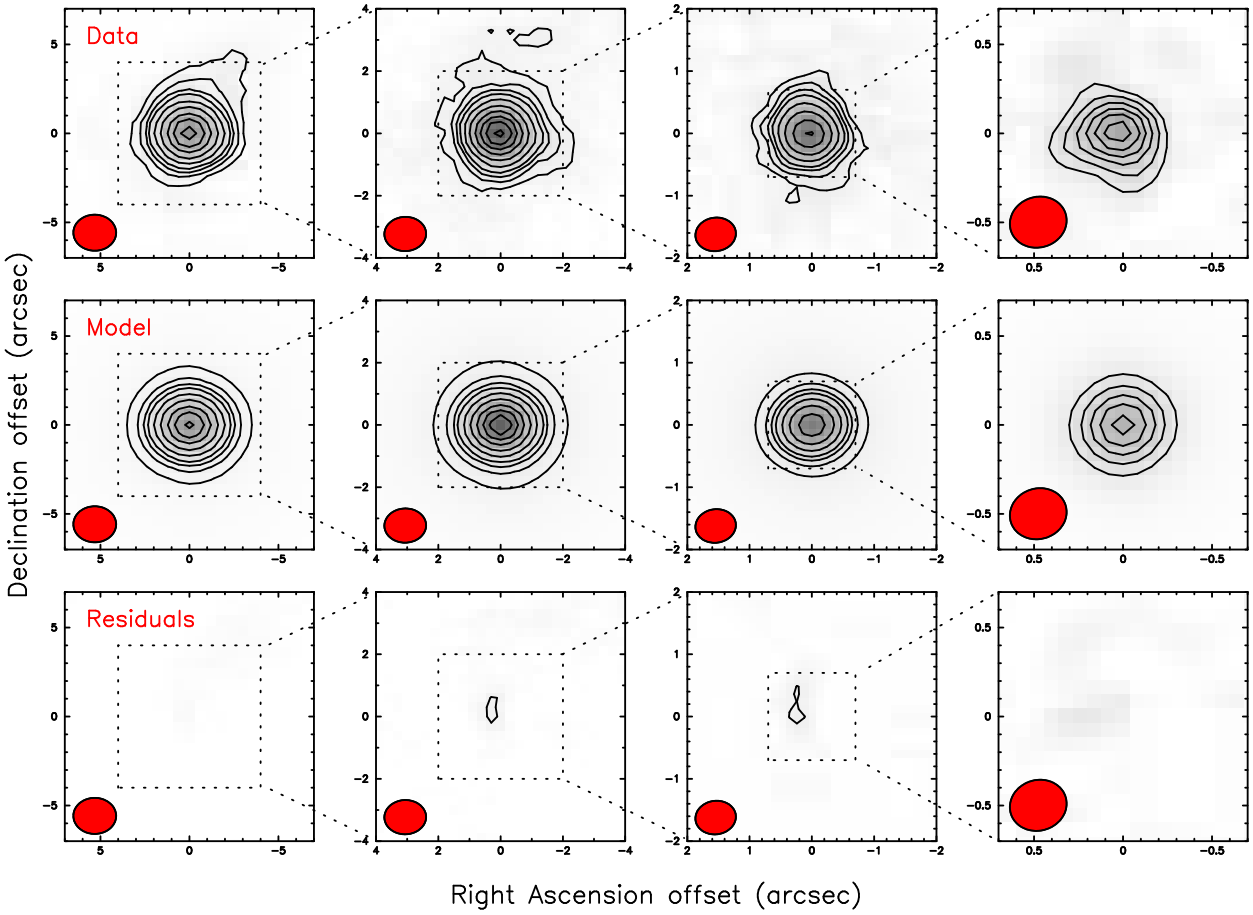

Figure 5.11 Comparison between 3 mm dust continuum data (*upper row*, as shown in Figure 5.4), model (*middle row*), and residuals (*lower row*) of L1157 in the image space. The power-law envelope model is used. Images in each column share the same *u-v* imaging weighting and contour levels. The contour levels, noise rms (σ), and beams are: *column 1*: [-3,2,3,4,5,7,10,14,18,22]$\times\sigma$, σ = 0.9 mJy beam^{-1}, 2.40″×2.03″ at a position angle of 90°; *column 2*: [-3,2,3,4,5,7,10,14,18,22,26]$\times\sigma$, σ = 0.6 mJy beam^{-1}, 1.34″×1.10″ at a position angle of -88°; *column 3*: [-3,2,3,4,5,7,10,14,18]$\times\sigma$, σ = 0.6 mJy beam^{-1}, 0.65″×0.54″ at a position angle of -82°; *column 4*: [-3,2,3,4,5,6,7]$\times\sigma$, σ = 0.9 mJy beam^{-1}, 0.32″×0.28″ at a position angle of -73°.

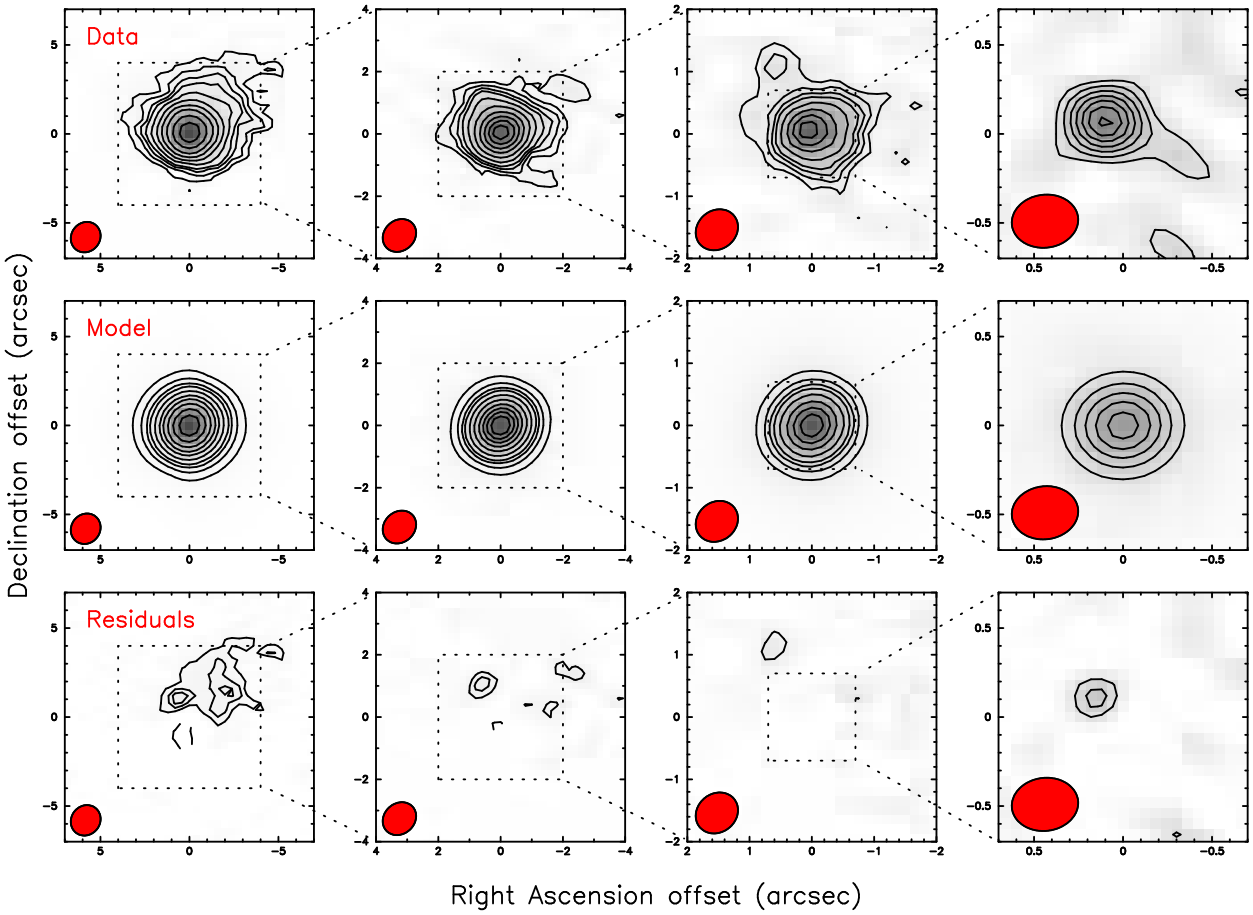

Figure 5.12 Comparison between 1 mm dust continuum data (*upper row*, as shown in Figure 5.4), model (*middle row*), and residuals (*lower row*) of L1157 in the image space. Images in each column share the same *u-v* imaging weighting and contour levels. The contour levels, noise rms (σ), and beams are: *column 1*: [-3,2,3,4,5,7,10,14,20,30,42]$\times\sigma$, σ =4.0 mJy beam^{-1}, 1.77″×1.61″ at a position angle of -38°; *column 2*: [-3,2,3,4,5,7,10,14,18,22,26]$\times\sigma$, σ =5.5 mJy beam^{-1}, 1.14″×0.98″ at a position angle of -48°; *column 3*: [-3,2,3,4,5,7,10,13,16]$\times\sigma$, σ = 7.0 mJy beam^{-1}, 0.71″×0.62″ at a position angle of -51°; *column 4*: [-3,2,3,4,5,6,7,8]$\times\sigma$, σ = 12.0 mJy beam^{-1}, 0.37″×0.30″ at a position angle of -83°.

profile can be related to a finite mass reservoir, as the constraint from an outer boundary can steepen the density in the outer envelope (Vorobyov & Basu, 2005a). Another possibility is the change of dust grain properties across the envelope. In particular, the inner dense part of the envelope is likely to have larger grains due to grain coagulation and hence greater opacity, making the estimated profile steeper than the actual value.

5.4.2 Spherical Power-law Envelope with an Inner Unresolved Component

Disk formation is a natural consequence as a rotating envelope collapses. It is expected to happen early in the star formation process, approximately in the Class 0 stage. While characterizing disks in Class 0 YSOs, in particular their size and mass, is critical to reveal the mass accretion process, observing them is difficult due to the dusty envelopes around them. Distinguishing the disk component from the envelope emission requires a good understanding of the envelope, measuring the unresolved emission as the circumstellar disk component (e.g., Keene & Masson, 1990; Chandler et al., 1995).

Despite that the pure power-law envelope can fit the observational data with statistical significance (§5.4.1), we add another parameter, a point source flux density, to the model to represent any unresolved component in our interferometric observations of L1157. In this study, we assume that the dust properties of the unresolved component are the same as the rest of the envelope for simplicity. Physically, this point source flux density is interpreted as an upper limit of the embedded disk component with a size smaller than the highest observational resolution of $\sim 0.3''$ or 75 AU.

We first consider only the statistical noise of the data visibility, and then include the absolute flux uncertainty using the same technique as discussed in §5.4.1. The result marginalized probability distributions of model parameters are shown in Figure 5.13 and Figure 5.14 for the cases without and with the absolute flux uncertainty, respectively. Table 5.3 lists the

Table 5.3. Power-law Envelope Model with an Unresolved Component

parameter	Mean	Radius of the 68% confidence interval (statistical noise only)	(with flux uncertainty)
dust opacity spectral index β	0.84813	3.8×10^{-4}	0.11
envelope mass (in $M_\odot$)	2.0662	2.6×10^{-3}	0.30
density power-law index p	1.95004	3.1×10^{-4}	0.02
unresolved 1 mm flux density (in mJy)	19.1835	3.2×10^{-3}	1.5

expectation values and uncertainties of the model parameters. Visualization of the model-data comparison using the marginalized parameters is shown in Figure 5.15, Figure 5.16, and Figure 5.17 in the visibility domain and the image domain.

Results of the power-law envelope plus an unresolved component model are consistent with the results of the pure power-law envelope model presented in §5.4.1. The posterior-weighted mean of the density power-law index p is slightly smaller than that of the pure power-law envelope model, due to the contribution of the point source flux. The dust opacity spectral index β and envelope mass is consequently affected. With the added complexity of the model, larger uncertainties for the model parameters are obtained. In particular, the flux of the unresolved component is low and not well constrained as it is not a necessary parameter. Nonetheless, the density index p is still close to 2, so the inconsistency with the Shu model still exists (§5.4.1).

The flux density of the unresolved component can be converted to the upper limit of the embedded disk mass. If we follow the empirical method of disk mass approximation in Looney et al. (2003) based on the disk modeling of HL Tau in Mundy et al. (1996), a disk of 0.05 $M_\odot$ at a distance of 140 pc is used as the standard candle for 100 mJy emission at 2.7 mm. As a result, our marginalized model gives a disk mass of 0.0039 $M_\odot$ or 4.1 M_{Jup}. Alternatively, we can use a single-temperature optically thin source model to estimate the mass, that is, $M = F_\nu d^2/\kappa_\nu B_\nu(T)$ (Hildebrand, 1983). Following Looney et al. (2000) with the assumptions of T = 60 K and κ=0.1(ν/1200 GHz) cm^2 g^{-1} (dust+gas), the estimated

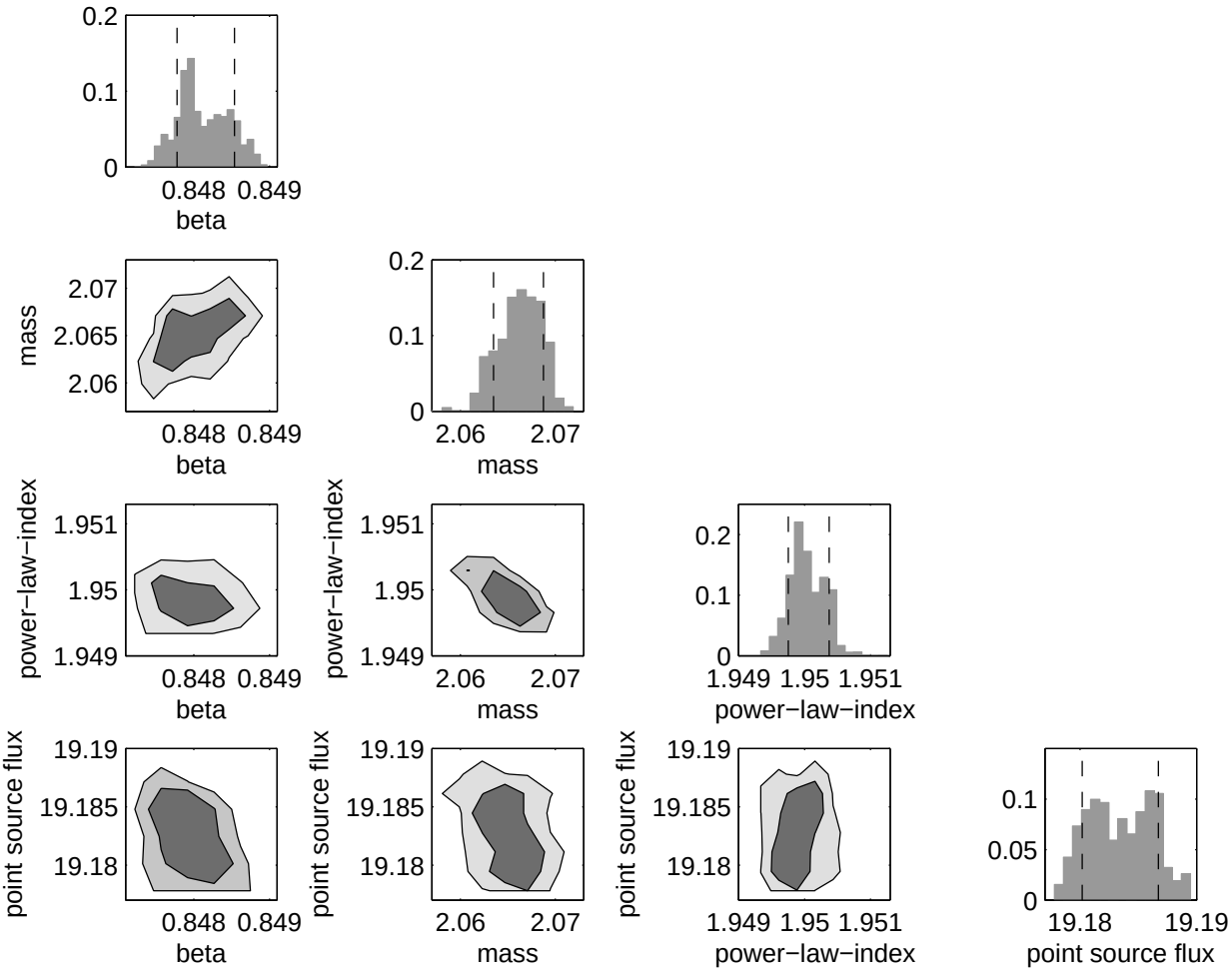

Figure 5.13 Same as Figure 5.8 but for the spherical power-law model with an unresolved component. The absolute flux uncertainty is not included. Marginalized posterior probability distributions for all four parameters (dust opacity spectral index β, envelope mass, envelope density power-law index p, and point source flux density at 1 mm) are shown. The units for envelope mass and point source flux density are $M_\odot$ and mJy, respectively. In the histograms, the dashed vertical lines enclose 68% or 1 σ confidence interval, with the expectation values and σ listed in Table 5.3. The dark and light areas in the 2-D contour plots are the 68% and 95% confidence regions.

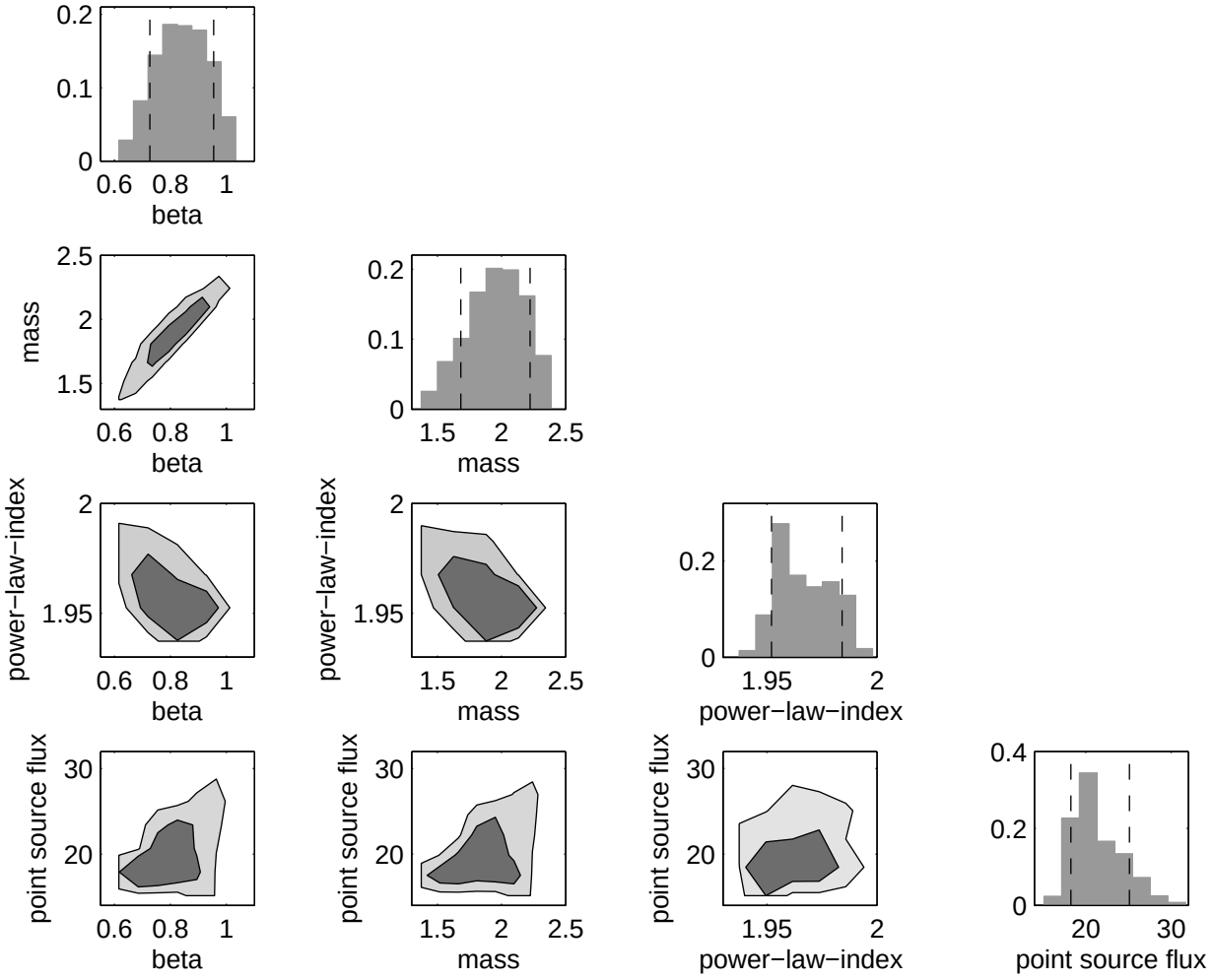

Figure 5.14 Same as Figure 5.13 for the spherical power-law model with an unresolved component, but the absolute flux uncertainty is included.

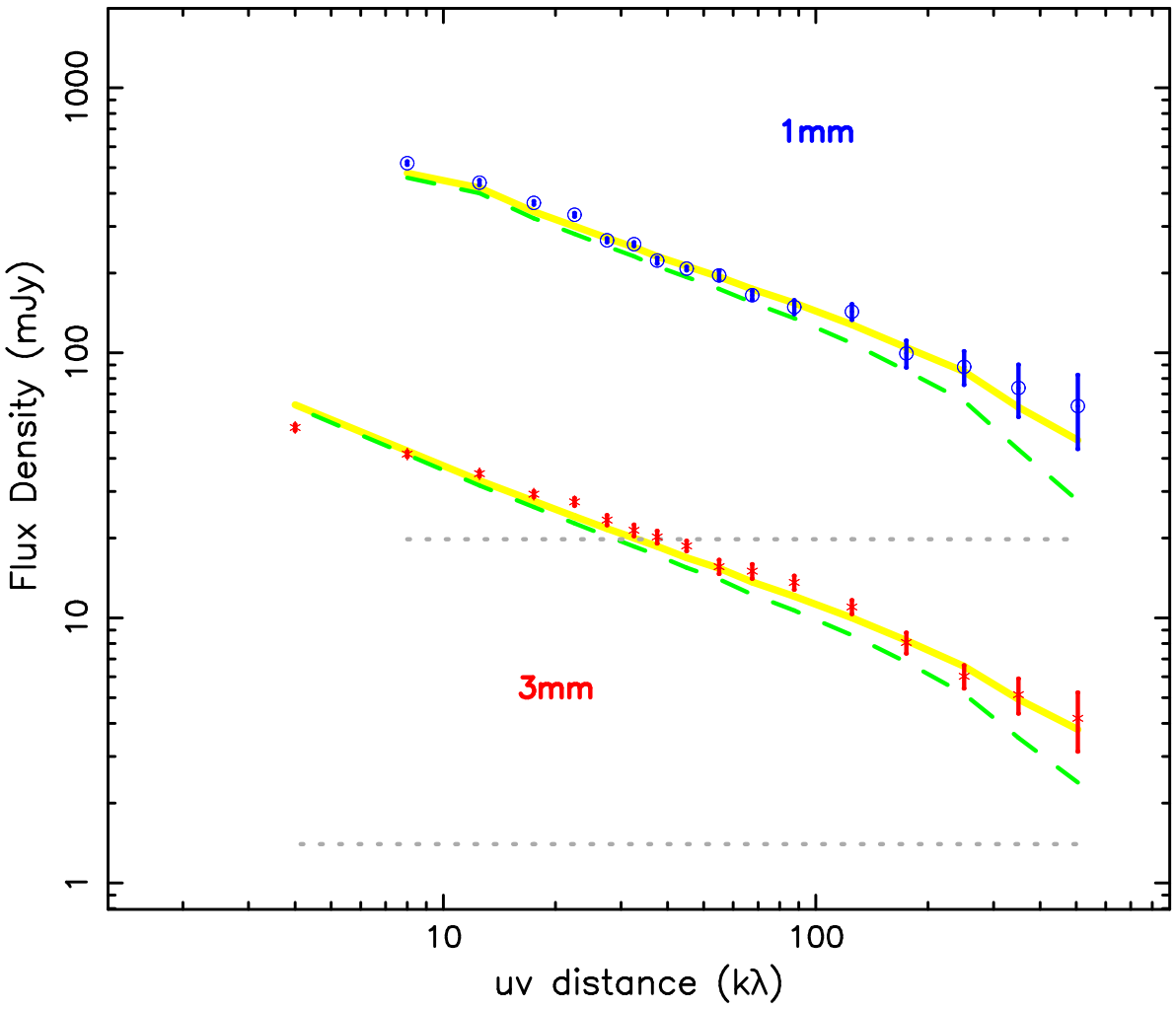

Figure 5.15 Same as Figure 5.10 but for the power-law envelope model plus an unresolved component. Observational flux density, averaged vectorially and binned in u-v annuli around the source center, are shown by circles for the 1 mm data and asterisks for the 3 mm data. The model fit with the marginalized parameters is shown by solid lines, which includes two components: a power-law envelope (broken lines) and an unresolved disk (dotted lines).

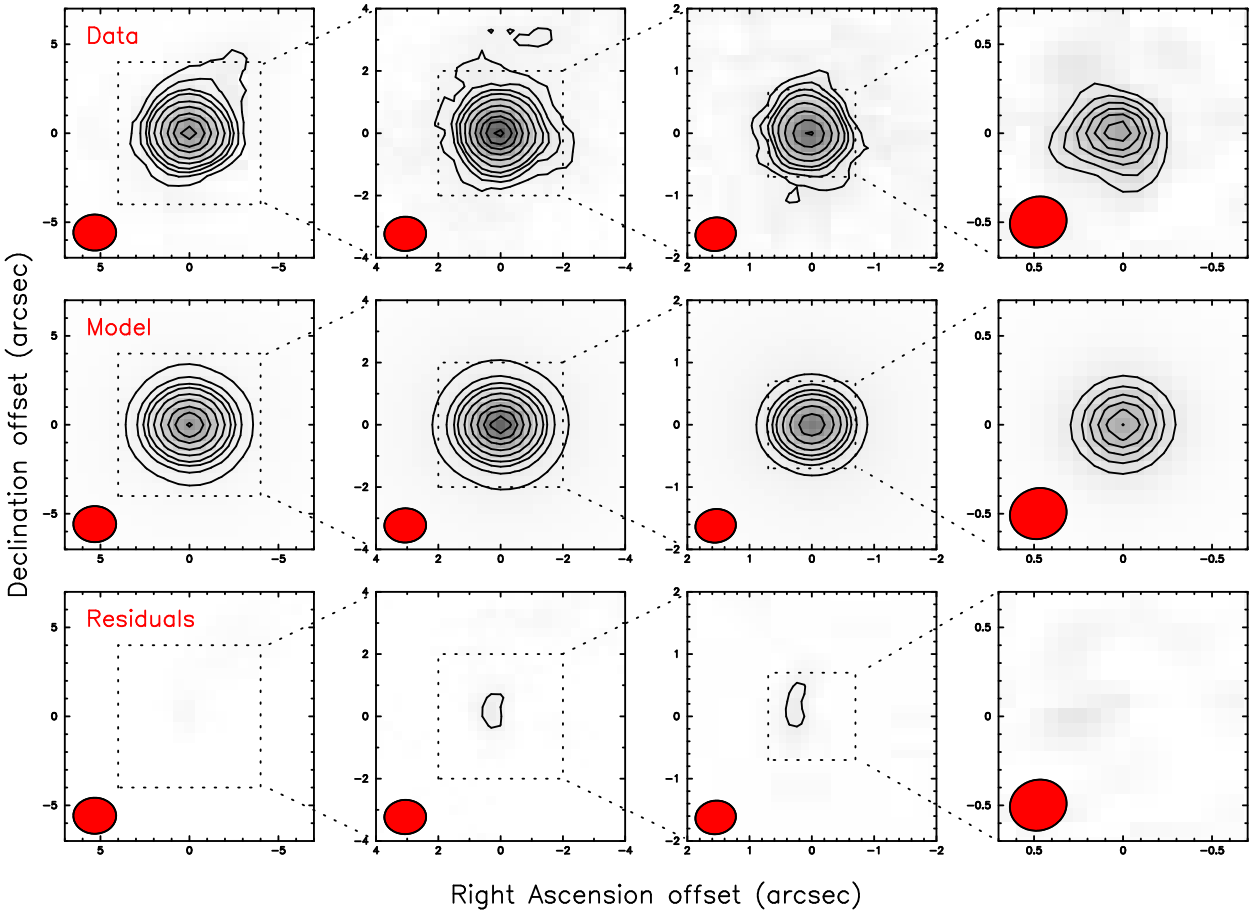

Figure 5.16 Same as Figure 5.11 but for the power-law envelope model with an unresolved component. Comparison between 3 mm dust continuum data (*upper row*), model (*middle row*), and residuals (*lower row*) of L1157 in the image space.

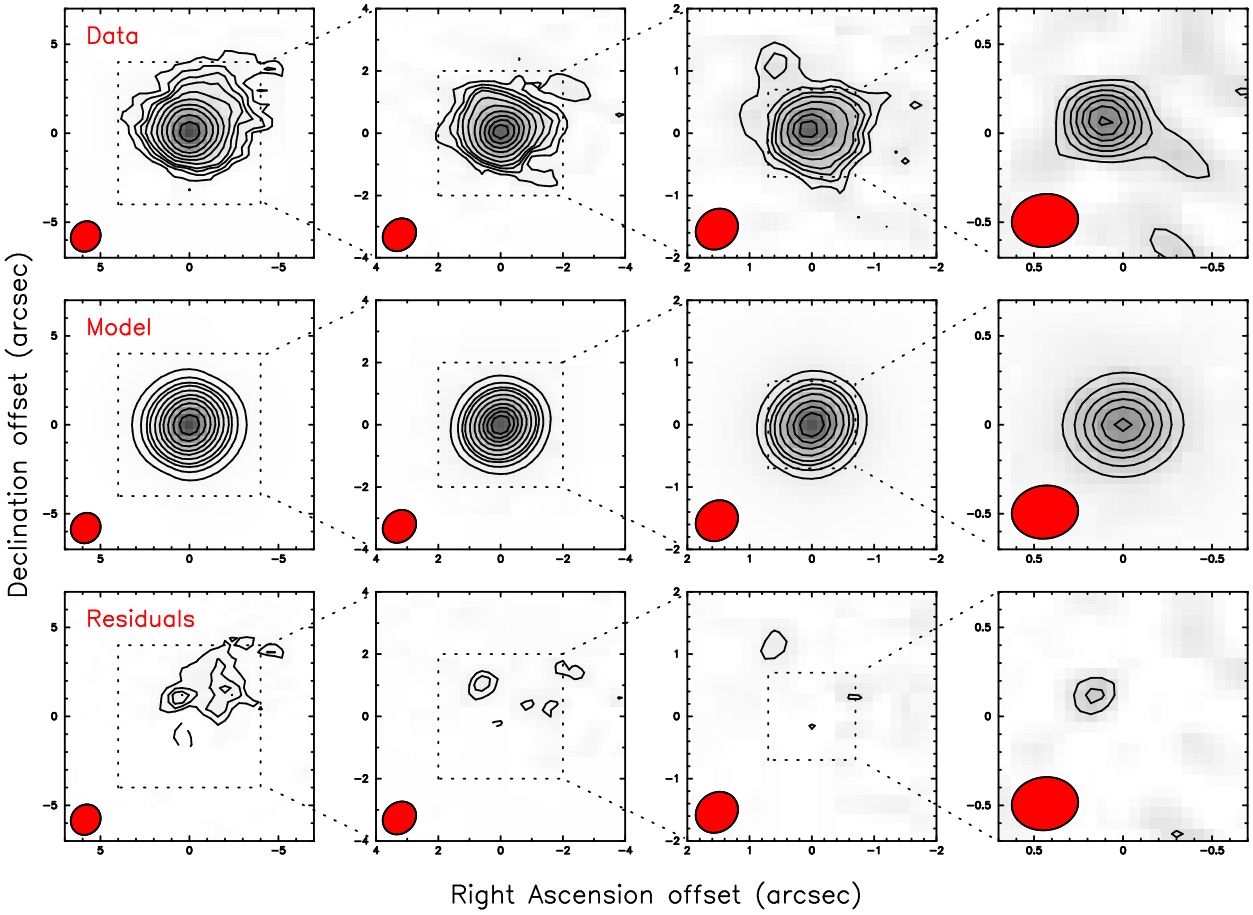

Figure 5.17 Same as Figure 5.12 but for the power-law envelope model with an unresolved component. Comparison between 1 mm dust continuum data (*upper row*), model (*middle row*), and residuals (*lower row*) of L1157 in the image space.

disk mass is 0.0034 $M_\odot$ or 3.6 M_{Jup}. Although these two methods of disk mass estimation give consistent results, the mass estimate is subject to the uncertainty of dust emissivity and temperature (see §5.5.6).

5.4.3 Rotating Collapse Model

Gravitational collapse of an envelope with uniform rotation has been studied in Ulrich (1976), Cassen & Moosman (1981), and Terebey, Shu, & Cassen (1984, hereafter the TSC model). The initial condition of the TSC model is a singular isothermal sphere, as in the Shu model. The non-zero angular momentum causes material to fall onto the midplane, following the streamline equation

$$\frac{r}{r_c} = \frac{\sin^2\theta_0}{1 - \cos\theta/\cos\theta_0}, \tag{5.16}$$

where r_c is the centrifugal radius ($r_c = r_0^4\Omega^2/GM$). A disk structure is expected inside the envelope with the density distribution

$$\rho = \frac{\dot{M}}{4\pi(GMr^3)^{1/2}}(1 + \frac{\cos\theta}{\cos\theta_0})^{-1/2}(\frac{\cos\theta}{\cos\theta_0} + \frac{2\cos^2\theta_0}{r/r_c})^{-1}. \tag{5.17}$$

We adopt the TSC model for the envelope fitting. The model parameters include: (a) the dust opacity spectral index β as in Eq. (5.3), (b) a mass scaling factor representing the total envelope mass, (c) the centrifugal radius r_c of the TSC model in Eq. (5.16) and Eq. (5.17), and (d) a point source flux density (at 1 mm) to represent any unresolved component. The unresolved component is assumed to have the same dust properties as the envelope for scaling the 1 mm flux density to 3 mm. Other model properties are as described in §5.3.

As in §5.4.1 and §5.4.2, the model fitting is done both without and with the absolute flux uncertainty. Figure 5.18 and Figure 5.19 show the marginalized probability distributions of model parameters for both cases, and Table 5.4 lists the expectation values and uncertainties of model parameters. Furthermore, visualization of the model-data comparison using the

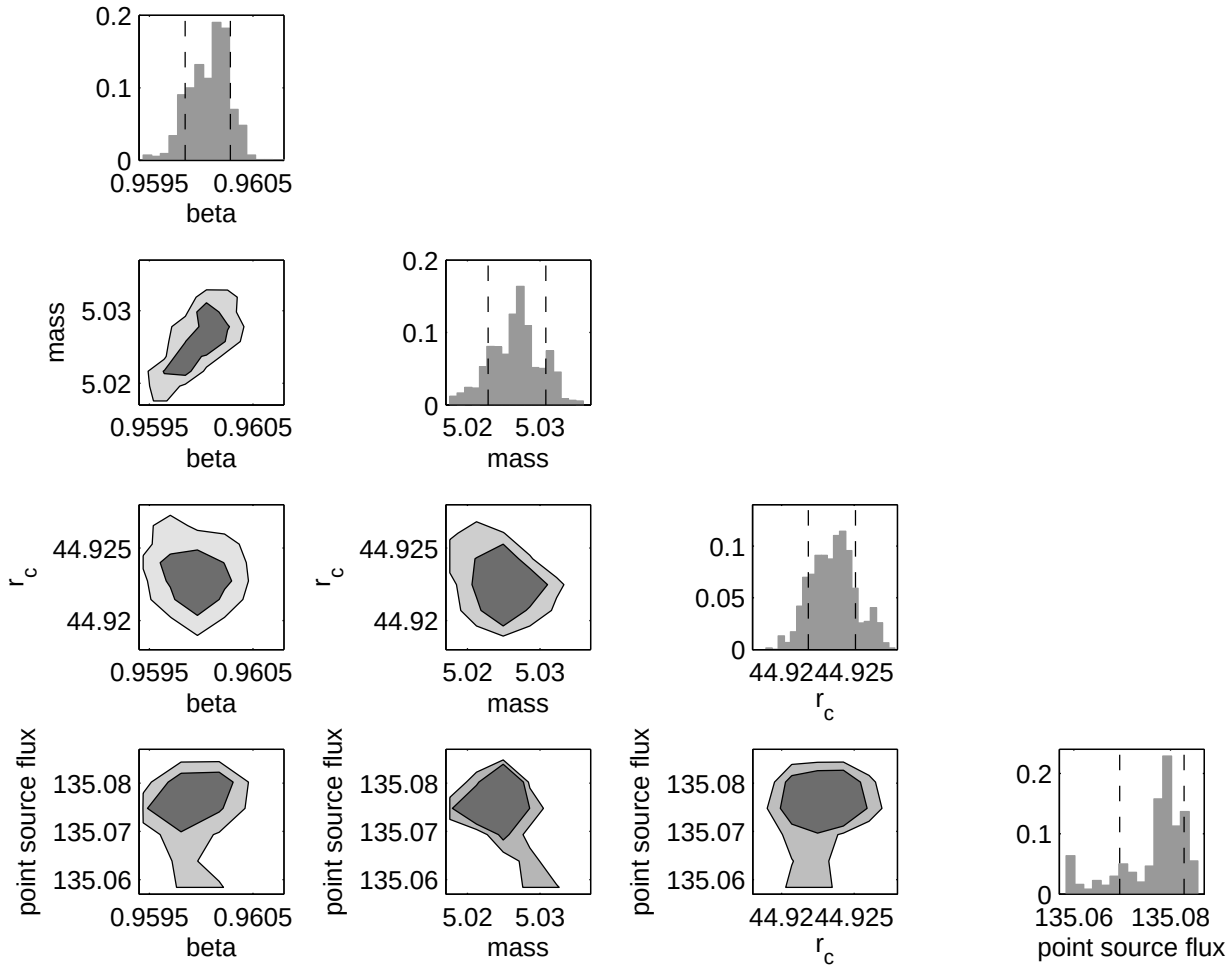

Figure 5.18 Same as Figure 5.8 but for the TSC model with an unresolved component. The absolute flux uncertainty is not included. Marginalized posterior probability distributions for all four parameters (dust opacity spectral index β, envelope mass, centrifugal radius r_c, and point source flux density at 1 mm) are shown. The units are $M_\odot$, AU, and mJy for envelope mass, centrifugal radius, and point source flux density, respectively. In the histograms, the dashed vertical lines enclose 68% or 1 σ confidence interval, with the expectation values and σ listed in Table 5.4. The dark and light areas in the 2-D contour plots are the 68% and 95% confidence regions.

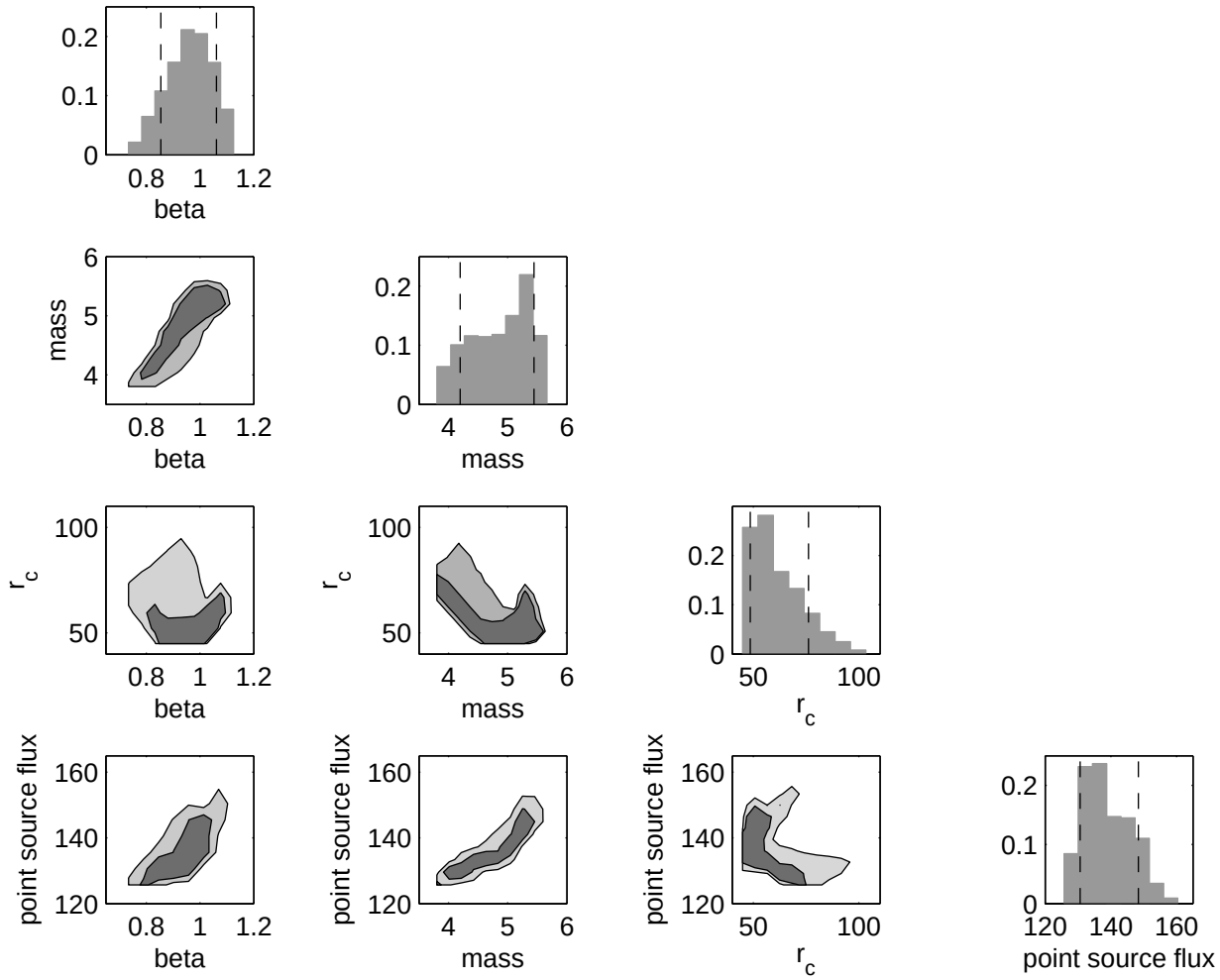

Figure 5.19 Same as Figure 5.18 for the TSC model with an unresolved component, but the absolute flux uncertainty is included.

Table 5.4. TSC Model with an Unresolved Component

parameter	Mean	Radius of the 68% confidence interval (statistical noise only)	(with flux uncertainty)
dust opacity spectral index β	0.96008	2.2×10^{-4}	0.10
envelope mass (in $M_\odot$)	5.0266	4.0×10^{-3}	0.62
centrifugal radius r_c (in AU)	44.9236	1.6×10^{-3}	13.76
unresolved 1 mm flux density (in mJy)	135.0764	6.7×10^{-3}	8.85

marginalized parameters is shown in both the visibility domain and image domain in Figure 5.20, Figure 5.21, and Figure 5.22

The TSC model fits the data with a bright point source component. In this case, the envelope contributes little flux towards the total dust continuum, and the unresolved disk component dominates the emission at both 1 mm and 3 mm, especially at long baselines (Figure 5.20). While a rather flat envelope model such as TSC is assumed, a stronger small-scale component is required to fit the data. Similar results have also been seen in other studies (e.g., Terebey et al., 1993; Enoch et al., 2009). As discussed in §5.4.2, the unresolved flux density can be converted to the upper limit of disk mass. The posterior-weighted parameters implies an embedded disk of $\sim$0.025 $M_\odot$ or 25 M_{Jup} using either method in §5.4.2.

In Figure 5.20, the model does not seem to match the data very well, although the best-fit model does pass a chi-square hypothesis test (or the null hypothesis is rejected with 90% confidence). This is partially a confusion resulting from data representation. Because there are about five million data visibilities and each data visibility contains low signal-to-noise, plotting them all does not show information. Therefore, for plotting purpose, data are averaged and binned in u-v annuli using the MIRIAD task uvamp, and the shown errors are statistical errors in the bins, not the uncertainty used in the modeling. Figure 5.23 plots the same data with a different set of bins, which in fact is somewhat closer to the effective weightings in the modeling. The same dataset can have multiple representations depending on how they are binned, and the statistical errors in the bins may not reflect

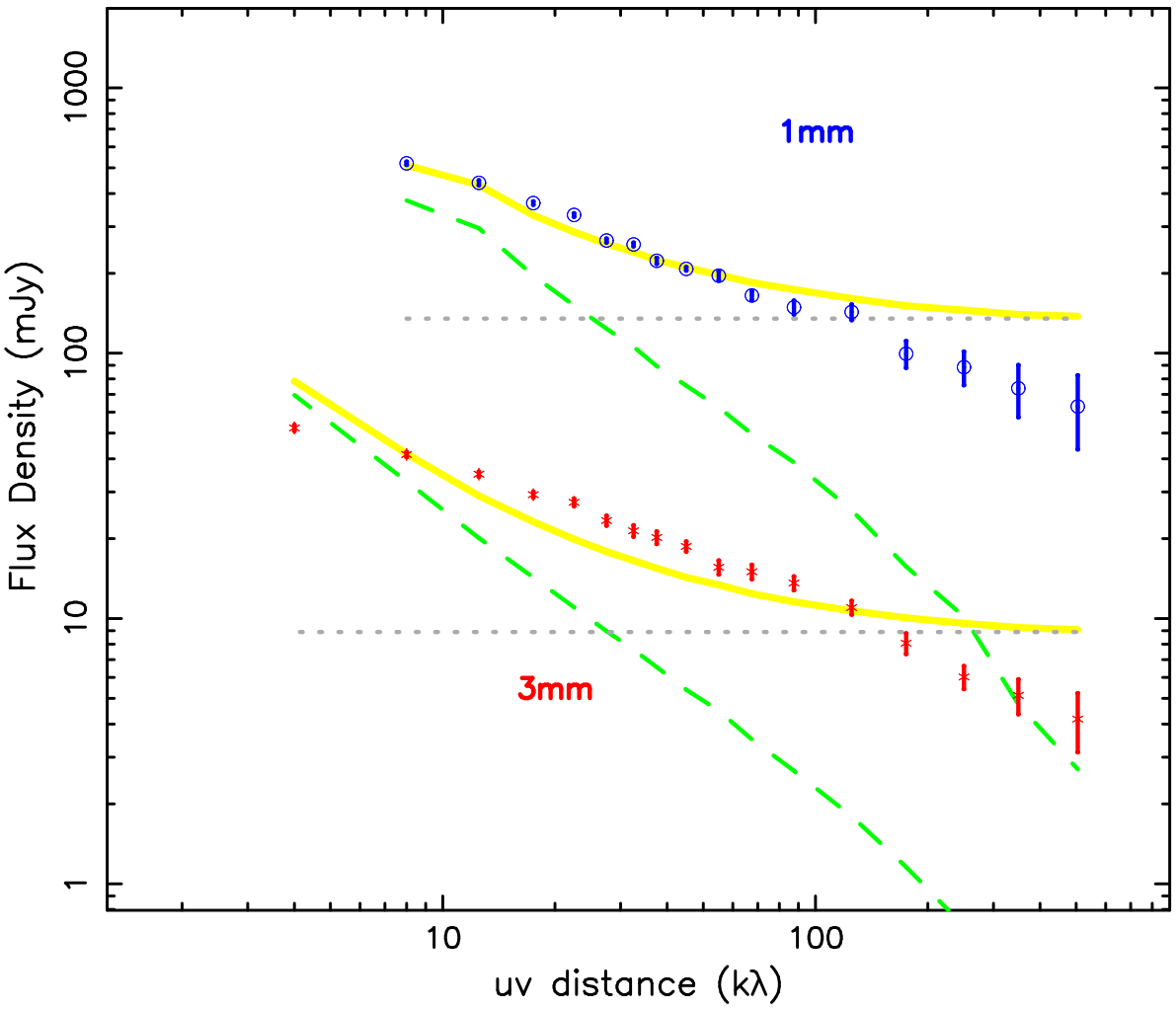

Figure 5.20 Same as Figure 5.15 but for the TSC envelope model plus an unresolved component. Observational flux density, averaged vectorially and binned in u-v annuli around the source center, are shown by circles for the 1 mm data and asterisks for the 3 mm data. The model fit with the marginalized parameters is shown by solid lines, which includes two components: an envelope (broken lines) and an unresolved disk (dotted lines).

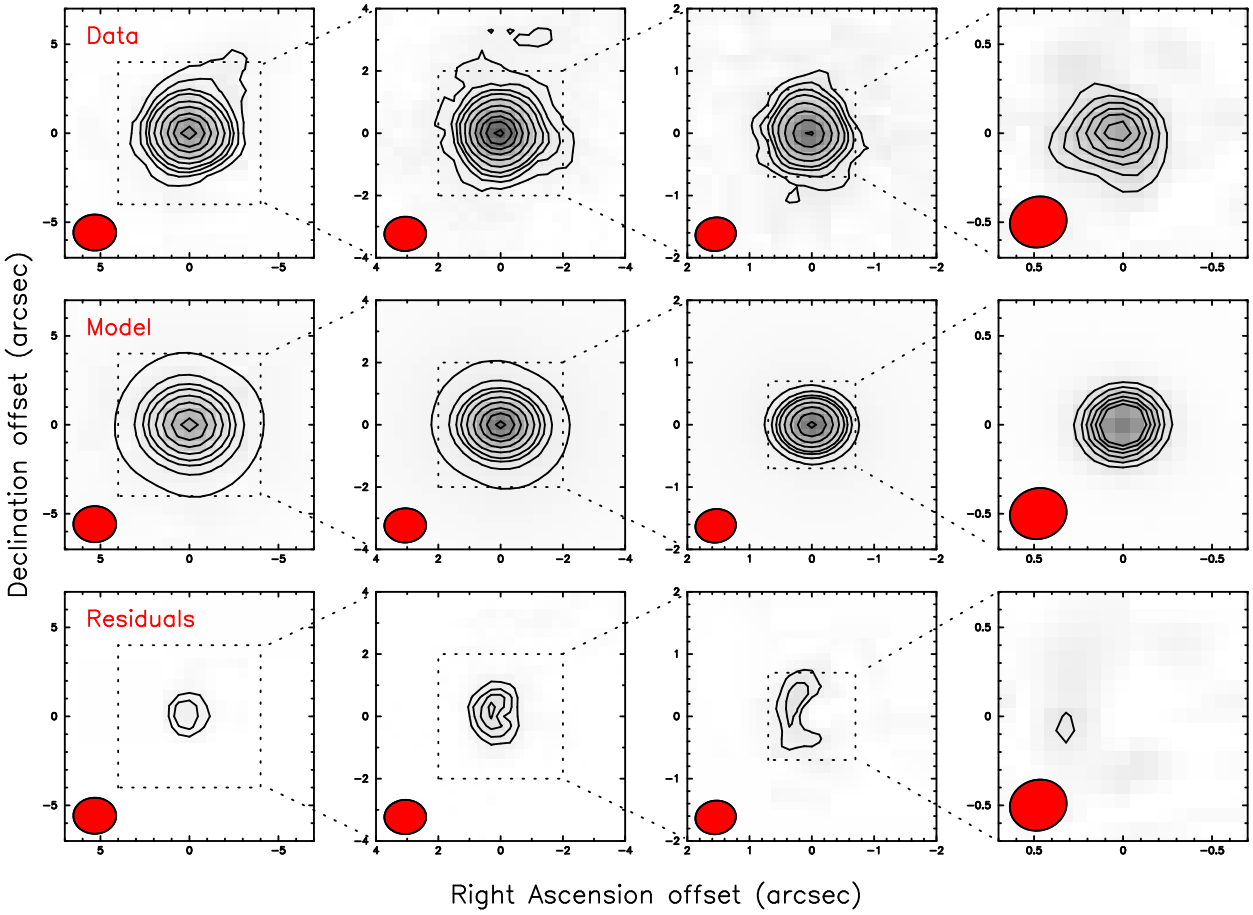

Figure 5.21 Same as Figure 5.11 but for the TSC model with an unresolved component. Comparison between 3 mm dust continuum data (*upper row*), model (*middle row*), and residuals (*lower row*) of L1157 in the image space.

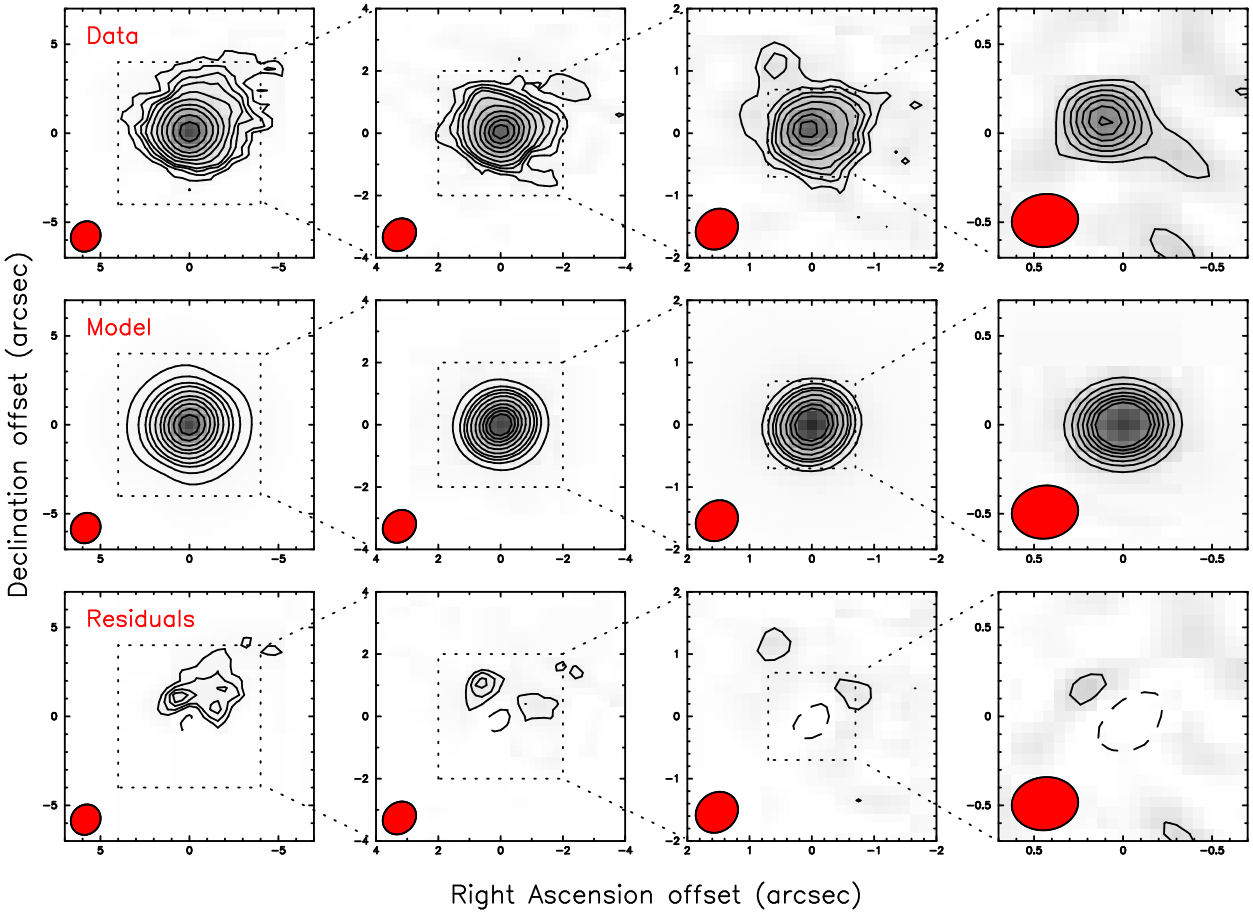

Figure 5.22 Same as Figure 5.12 but for the TSC model with an unresolved component. Comparison between 1 mm dust continuum data (*upper row*), model (*middle row*), and residuals (*lower row*) of L1157 in the image space.

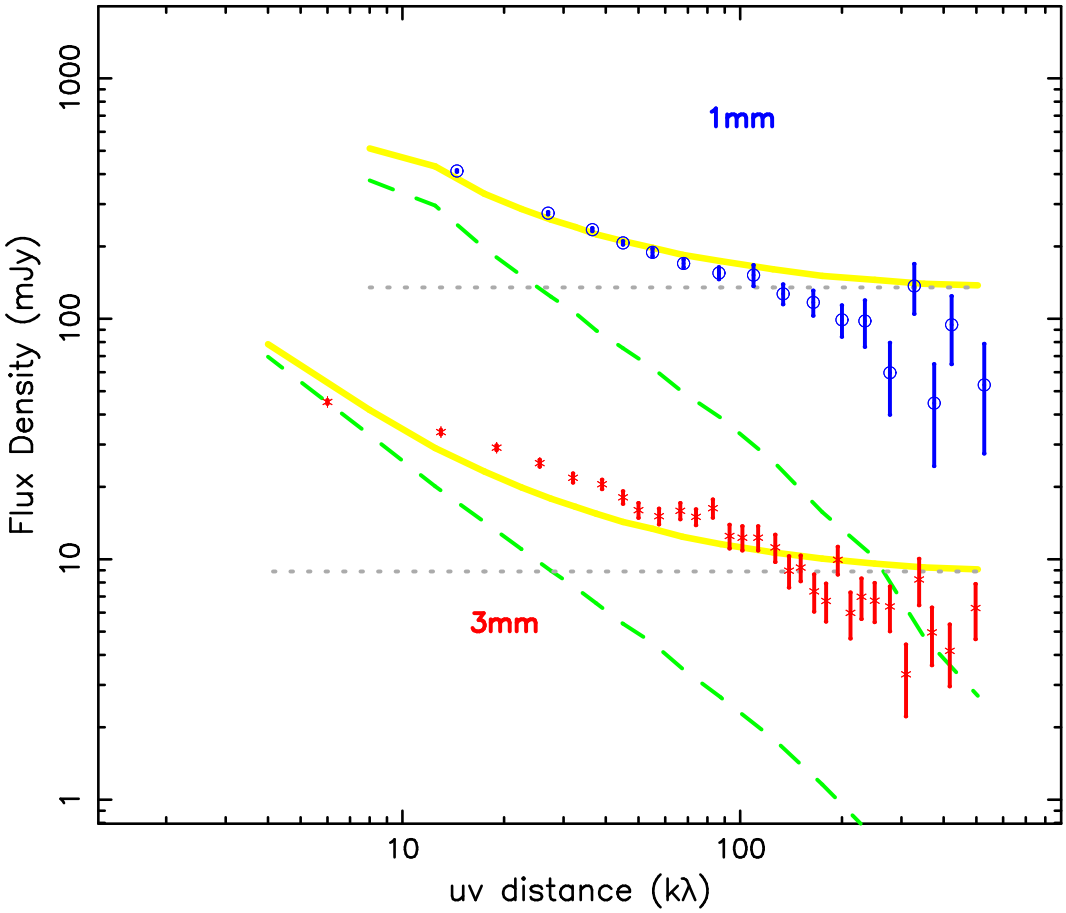

Figure 5.23 Same as Figure 5.20 but observational data are binned differently to demonstrate that binned visibilities can be misleading. As there are approximately five million data visibilities, they are binned (using MIRIAD task uvamp) for plotting. However, the choice of bins can significantly alter the data realization.

the whole uncertainty, therefore can be misleading. Moreover, any information on non-spherically symmetric structures is lost in the annuli-bins. This also demonstrates that it is more proper to perform model fitting data point by data point instead of averaged bins only.

Nonetheless, the fit with the TSC model appears to be worse than the power-law envelope model. As seen in Figure 5.21 and Figure 5.22, the model does not subtract the data as cleanly as the power-law model does and leaves more residuals. In particular, residuals at 5 σ level are seen in the 3 mm image (column 2 in Figure 5.21). A worse fit is also shown by a larger χ^2, which will be examined in more detail in §5.5.4.

5.5 Discussion

5.5.1 Data Uncertainty

The absolute flux uncertainty is the largest source of systematic uncertainty in the data. Although the relative amplitudes are somewhat preserved against the absolute flux uncertainty, it dominates the errors in parameter estimation of model fitting. In particular, the spectral parameter β is significantly less constrained when the absolute flux uncertainty is included, and other parameters can be affected directly or indirectly through the uncertainty of β. We consider the absolute flux uncertainty by marginalizing over the 10% uncertainties and demonstrate its effects on parameters. Other systematic uncertainty from instruments and calibrations may exist and propagate in the analysis as well, but are presumably less than 10%.

5.5.2 Free-free Contamination

We ignore contribution of free-free emission in this study. Free-free emission from ionized winds or jets can contribute partial flux at millimeter wavelengths ($\sim$20% at 7 mm, Rodmann et al., 2006) and affect model parameter estimates especially for β and disk component. However, it plays a minimal role for our data of L1157 at 1 mm and 3 mm. By extrapolating fluxes at 8.5 GHz and 4.86 GHz (Meehan et al., 1998) to our observed frequency, we estimated the free-free emission to be around 0.53 mJy at 3 mm and 0.39 mJy at 1 mm for L1157. The free-free correction is negligible in the analysis.

5.5.3 Connection with Gas Emission

As shown in Chiang et al. (2010, or Chapter 2), a large-scale flattened envelope that extends $\sim$20,000 AU normal to the outflow direction is detected around L1157 in both N_2H^+ molecular emission and 8 μm absorption. This flattened structure is not seen in the dust

continuum because the large-scale dust emission at millimeter wavelengths is too dim to be detected with current observational sensitivity, as demonstrated in §2.4.4. The large-scale geometry is not incorporaed into the dust continuum modeling presented in this chapter; however, tests have shown that the large-scale geometry ($\gtrsim$2,000 AU) does not significantly affect the envelope emission at small scales.

5.5.4 Model Comparison

A model is just a simplification of the unknown reality. As George E. P. Box said, "all models are wrong, but some are useful," we want to know which model provides a better approximation to all available data. In this section we apply model selection techniques and rank the models.

By applying Bayesian inference at the model level, one can use the Bayesian evidence for model selection. Formulated in Eq. (5.8) and Eq. (5.9), the Bayesian evidence represents the probability of data given the model. It is marginalized over the full parameter space so the values of model parameters are not important, as opposed to parameter estimation for a particular model (§5.3.5). For comparing two competing models, the ratio of evidence, also known as the Bayes factor, represents posterior odds and can infer whether one model is preferred over the other (see Liddle, 2009, for a review).

However, an exact method to compute the Bayesian evidence needs to fully evaluate likelihood in the entire parameter space and is very computationally expensive. The posterior distribution sampled by MCMC (§5.4) peaks around the maximum posterior probability, and is not sufficient to calculate the Bayesian evidence. Approximation such as the use of information-theoretic methods is a good alternative approach for model selection (e.g., Liddle, 2007). For example, the Akaike information criterion (AIC, Akaike, 1974), derived using the Kullback-Leibler information (or K-L distance), is defined as

$$\mathrm{AIC} \equiv -2 \ln \mathcal{L}_{max} + 2k, \tag{5.18}$$

where $\mathcal{L}_{max}$ is the maximum likelihood and k is the number of model parameters. AIC provides a simple measure of how good the model approximates the information contained by the data, and a smaller value implies less information is lost and hence a better model. Detailed derivation and statistical implications can be found in Burnham & Anderson (2002). A second-order AIC, or AIC corrected, is suggested for small-sample bias adjustment as in

$$\mathrm{AIC}_c = \mathrm{AIC} + \frac{2k(k+1)}{N-k-1}, \tag{5.19}$$

where N is the number of data points. But in our case, $N \gg k$ so AIC and AIC_c converge. On the other hand, the Bayesian information criterion (BIC, Schwarz, 1978), defined as

$$\mathrm{BIC} \equiv -2 \ln \mathcal{L}_{max} + k \ln N, \tag{5.20}$$

is an approximation based on the Bayesian evidence ratio (also see Liddle, 2004).

A good model seeks for balance between goodness of fit and model simplicity. To obtain a better fit to the data or a smaller χ^2, one may increase the model complexity with more parameters, but unnecessary use of parameters and over-fitting should be discouraged. The tradeoff is also seen in Eq. (5.18) and Eq. (5.20). As the best model minimizes AIC and BIC, smaller χ^2 decreases the first term but extra parameters increase the second term. Model complexity in terms of the number of parameters is penalized in either AIC or BIC.

In this study, we evaluate AIC_c and BIC for all models. Because either AIC_c or BIC is on a relative scale, only the differences instead of actual values are meaningful (Burnham & Anderson, 2002). Results are listed in Table 5.5, where the model with the smallest value is preferred. As AIC_c and BIC suggest different ranking between the pure power-law envelope model and the power-law envelope plus an unresolved component, we do not make an inference between them. However, the results show a large positive $\Delta\mathrm{AIC}_c$ and ΔBIC for the TSC model, implying that the power-law envelope model (either with or without

Table 5.5. Model Comparison

Model	k	$\Delta\mathrm{AIC}_c$	ΔBIC
Power-law envelope	3	1.9	0
Power-law envelope + an unresolved component	4	0	11.5
TSC envelope + an unresolved component	4	2229.5	2241.0

Note. — The preferred model has the smallest value.

the unresolved component) is decisively preferred against the TSC model plus an unresolved component.

The model selection results are consistent with the *a posteriori* check presented in §5.4. Compared to either pure power-law envelope model or the power-law envelope plus an unresolved component, considerable residuals are seen in the image domain for the TSC model plus an unresolved component.

5.5.5 Grain Growth

As mentioned in §5.3.3, dust properties are characterized by the opacity spectral index β in our modeling. Depending on the environment, β typically varies between 0 and 2. While $\beta \sim 2$ implies small grains as in the interstellar medium, a smaller β is usually found in many YSOs (e.g., Natta et al., 2007). Decrease of β can be caused by many factors, such as change of composition or grain geometry, but is usually associated with change of grain size distribution (e.g., Krügel & Siebenmorgen, 1994). The β value can be an evolutionary indicator of the dust grains in YSOs, as small grains in YSOs grow through coagulation, and eventually form planet if conditions allow. Nevertheless, Miyake & Nakagawa (1993) studied the size effect and showed that the observed decrease of β in disk regions can be explained by the growth of grain size without change of chemical composition. If the grains in a dense

region are composed of the same materials as in the interstellar grains, the maximum grain size is expected to be larger than 3 mm to explain the observational results of $\beta \lesssim 1$ (Draine, 2006). Grain growth has been the most widely accepted explanation for the small β found in protoplanetary disks (e.g., Beckwith et al., 2000; Draine, 2006).

In the three envelope models presented in §5.4, the posterior-weighted mean of β range from 0.84 to 0.96. The absolute flux calibration dominates the uncertainty of β estimation, resulting in a systematic uncertainty of $\sim$0.1. Still, β being significantly smaller than the interstellar value is indicated. Our β estimate for L1157 is in agreement with the samples of Class 0 YSOs in Jørgensen et al. (2007), Kwon et al. (2009), and Shirley et al. (2011b). The result implies that dust grains in L1157, and arguably most Class 0 YSOs, have gone through some grain growth to at least millimeter size from the initial interstellar grains. However, when exactly dust grains start to grow during the protostellar evolution is uncertain. For example, Ricci et al. (2010a) compared β of YSOs with their evolutionary ages and did not find apparent trend or difference in β for YSOs in different evolutionary stages.

As a uniform dust grain property is adopted in our simple dust model, our estimate of β represents the grain property in the whole system, including disk and envelope. Depending on the assumed envelope model, the embedded disk can contribute a significant fraction of flux. Compared to grains in the envelope, grains in the disk are expected to be larger in size as an initial step of planet formation. Therefore, a smaller β is expected in the disk than in the envelope. Besides, grain properties are likely to vary across the envelope, as has been observationally suggested for Class 0 sources (e.g., Chandler & Richer, 2000; Kwon et al., 2009). The radial dependence of β or a disk with a different β is not modeled in this study; to address the dust property change in YSOs requires a more complex model.

5.5.6 The Earliest Circumstellar Disks

Circumstellar disks form as a physical consequence of dynamical collapse when protostars accrete materials from their surrounding envelopes. These planet-forming pre-main-sequence

disks have been observed and studied extensively (e.g., see the reviews of Williams & Cieza, 2011). To date, studies of protostellar disks mostly focus on the T Tauri phase or later, while disks at earlier ages are poorly constrained. In particular, disk evolution from early Class 0 to Class I stage is interesting as it is the phase that most mass accretion is going on. The size of the disk, characterized by the centrifugal radius r_c, grows rapidly as the system evolves and depends on the rotation rate and the magnetic field strength of the background cloud (e.g., Terebey et al., 1984; Basu, 1998).

While the mass and size of these youngest disks are essential to reveal the early process of disk formation, observing them is, however, not straightforward. In addition to the limitations of observational resolution and sensitivity, these disks are deeply embedded in their natal envelopes; probing them usually relies on indirect methods. For example, detection of water and methanol lines in Class 0 protostars can constrain the embedded circumstellar disks as the emission is probably originated from the warm shocked layer of the disk-envelope interface (e.g., Goldsmith et al., 1999; Velusamy et al., 2002; Watson et al., 2007; Jørgensen & van Dishoeck, 2010). Near-infrared scattered light image, showing a dark lane along the edge-on disk, has also been used to infer the embedded disk structure (Tobin et al., 2010a).

Another way to probe these youngest disks in embedded YSOs is through observations of dust continuum with a two-component model. With assumptions of the envelope structure, radiative transfer modeling of millimeter interferometric data separates the circumstellar disk component from the emission of the surrounding envelope. In other words, the disk component is measured as the residual emission with the envelope contribution subtracted (e.g., Keene & Masson, 1990; Looney et al., 2003; Harvey et al., 2003; Jørgensen et al., 2005). This method avoids the complexity of chemical effects, but requires the use of a theoretical envelope model.

Using a two-component model, attributing the entire unresolved flux to be from the embedded disk, and following the mass estimation in Looney et al. (2000) and Looney et al. (2003), we derive the disk mass to be $\sim$4 M_{Jup} assuming a power-law envelope, or $\sim$25

M_{Jup} assuming a TSC envelope. The mass estimate is highly dependent of the assumed envelope structure, dust opacity, disk temperature, and optical depth. For the envelope structure, we have shown that the power-law envelope model is preferred against the TSC model. But a large uncertainty still exists. For example, if instead we follow Greaves & Rice (2011) with the assumed dust opacity of κ=0.015(ν/300 GHz) cm^2 g^{-1} (dust+gas) and single temperature of 30 K, the disk mass is ∼13 M_{Jup} for the power-law envelope and ∼92 M_{Jup} for the TSC envelope. Additionally, the deduced disk mass appears to be in the low end compared with other Class 0 YSOs presented in Greaves & Rice (2011).

On the other hand, an empirical method that measures the small-scale flux at baseline ∼50 kλ has also been used to estimate the disk mass in embedded YSOs (Jørgensen et al., 2009; Enoch et al., 2011). This is based on the presumption that envelope contributes little flux $\gtrsim$50 kλ. The 1 mm flux density of L1157 is around 200 mJy at 50 kλ, implying a disk mass of 0.166 $M_\odot$ or 174 M_{Jup} with $\kappa_{1.3mm}$=0.009 cm^2 g^{-1} as in Enoch et al. (2011). The estimated disk mass is comparable to other Class 0 sources in Enoch et al. (2011) and lighter than those in Jørgensen et al. (2009), but much heavier than our disk mass estimate using a two-component model. The empirical method of Jørgensen et al. (2009) and Enoch et al. (2011) seems to over-estimate the disk component in L1157, as it may not be applicable to L1157; one reason is that the flux density drops significantly longward of 50 kλ (Figure 5.3) so the flux from the unresolved disk is apparently lower than 200 mJy. In addition, a relatively flat envelope profile is assumed in either study (power-law of 1.5 in Jørgensen et al. 2009 and TSC in Enoch et al. 2011), and the assumed envelope structure considerably affect the flux ratio from envelope and disk.

Since our observations do not resolve the circumstellar disk, we can put an upper limit on the disk size for L1157. Assuming a distance of 250 pc, the upper limit of the disk radius is ∼40 AU. This size is consistent with the estimates of embedded disks in other Class 0 YSOs. For example, an upper limit of 50 AU in radius is suggested for the edge-on Class 0 YSO VLA 1623A in Ward-Thompson et al. (2011). On the contrary, the disk embedded in

the edge-on Class 0 YSO L1527 has been resolved by 7 mm VLA observations in Loinard et al. (2002); the disk structure is also seen with SMA and CARMA observations (Tobin et al. in preparation). The size of Class 0 disks is comparable to or smaller than the size of older circumstellar disks (e.g., Eisner et al., 2005; Andrews et al., 2009; Vicente & Alves, 2005), but no clear trend can be inferred at this point.

5.6 Summary

1. Multi-configuration CARMA observations of the edge-on Class 0 YSO L1157 are presented. In both 1 mm and 3 mm dust continuum, a nearly spherical circumstellar envelope is seen at the size scale of $\sim 10^2$ to $\sim 10^3$ AU. The large-scale ($>10^4$ AU) flattened structure, seen in the 8 μm absorption, N_2H^+, and NH_3 emission (Looney et al., 2007; Chiang et al., 2010; Tobin et al., 2011), is not detected in the dust continuum. No circumstellar disk on the small scale is resolved.

2. Radiative transfer modeling is performed to compare the interferometric data with the theoretical envelope models. A power-law envelope and a TSC envelope are considered. We add an unresolved component to represent the embedded disk. Bayesian inference is employed for parameter estimation. The absolute amplitude uncertainty, resulting from the flux calibration of the data reduction process, plays a critical role in parameter errors.

3. A density index $p \sim 2$ is suggested for the power-law envelope, consistent with the results in Looney et al. (2003) for a larger sample of Class 0 YSOs. An unphysical young age is suggested if the Shu model is applied strictly. The data can be fitted by a pure power-law envelope without a compact emission from the embedded disk component.

4. The dust grain properties of the envelope are studied through the dust opacity spectral

index β. The result $\beta \sim 0.9$ is significantly smaller than the β value in the interstellar medium, implying that grain growth has already started in L1157.

5. The unresolved disk component is constrained to be smaller than ∼40 AU in radius and ∼4-25 M_{Jup} in mass. However, the mass estimate of the embedded disk component heavily relies on the assumed envelope model as well as the assumed disk characteristics. For example, a flat envelope, such as the TSC model with a density power-law index $p \sim 1.5$ in the outer region, requires a strong point source flux from the unresolved disk, while a steep envelope with $p \sim 2$ can fit the observations without an embedded disk.

6. Different envelope models are compared using an information-theoretic approach. The results prefer the power-law envelope model against the TSC model, which is also shown in the *a posteriori* check in the image domain.

7. This is the first study that utilizes the Bayesian techniques and model selection to consider multiple envelope models and make statistical inference for embedded YSOs. Future observations, especially high-resolution ALMA observations, will resolve the transition zone between the envelope and the disk, and further constrain the structures of Class 0 YSOs.

Chapter 6

Conclusions

This thesis presents interferometric observations and modeling of the circumstellar material around low-mass protostars in their earliest stage of evolution. At such a young age, protostars are surrounded by their natal dusty envelopes and are nearly invisible at optical and near-infrared wavelengths; observing them at millimeter wavelengths is one of the best ways to understand these young systems. Using millimeter-wave interferometers, I aim to reveal the nature of the circumstellar structures on multiple size scales. In particular, archived BIMA data as well as new CARMA observations of a sample of Class 0 YSOs are studied, utilizing theory-inspired models and radiative transfer calculations.

While most protostars are formed in multiple systems, the Class 0 YSO L1157 appears to be isolated, making it an ideal laboratory to study low-mass star formation. Besides the simpler environment, its nearly edge-on orientation is well-determined by outflow observations; hence ambiguity is minimized in the analysis. In Chapter 2 and Chapter 5, I focus on L1157 and study its structures and kinematics from sub-arcsecond to arcminute scales, using both molecular lines and dust continuum.

Unlike most of the Class 0 YSOs, which show complex morphology at 10,000 AU scales, L1157 has a highly-symmetric flattened envelope. This flattened structure extends over 20,000 AU in the direction normal to the outflow orientation and is detected in both 8 μm absorption and N_2H^+ emission. The N_2H^+ emission also shows a trend of increasing N_2H^+ abundance towards the protostar as well as depletion in the innermost region; this is consistent with the expectations of chemical models.

Gas kinematics in the flattened envelope of L1157 is examined with a simple modeling

of the position-velocity diagram. A velocity gradient of $\sim$1.5 km s^{-1} pc^{-1}, slower than most other Class 0 samples in Chen et al. (2007) and Tobin et al. (2011), is detected perpendicular to the outflow direction; though the flattened structure is not rotationally supported. The large-scale velocity gradient can be interpreted as a slow solid-body rotation, as commonly seen in many prestellar cores. In addition, a broader linewidth is observed in the inner envelope, which was initially thought to be caused by gravitational infall, but has later found to show outflow interactions (Chiang et al., 2010; Tobin et al., 2011). In reality, both infall and outflow are likely ongoing.

On the other hand, the dust continuum of L1157 shows compact, nearly-spherical envelope from $\sim$75 AU to $\sim$2000 AU. The flattened structure at $\sim$20,000 AU scale, seen in 8 μm absorption and N_2H^+ emission, is too dim to be detected in dust continuum by our CARMA observations. A simple model motivated by the large-scale geometry is constructed to illustrate the connection between the large-scale gas emission and the small-scale dust emission. Deviation from spherical symmetry is important at large scales, but not observed at small scales.

The detailed physical properties of the collapsing envelope are not yet well established, given the current observational resolution and sensitivity. In Chapter 3 and Chapter 5, attempts are made to fit dust continuum observations with theoretical envelope models. In particular, while neither the Larson-Penston nor the Shu model can fit a sample of Class 0 YSOs with reasonable ages, the Tassis-Mouschovias model provides statistically significant fits in a 1-D approximation. A more complete 3-D modeling is later performed with Bayesian statistics to study a selection of envelope models. The fits are obtained for each model and examined in both visibility and image domain. Furthermore, models are compared using an information-theoretic approach. For the case of L1157, a power-law envelope model is preferred against the commonly used Terebey-Shu-Cassen model.

Circumstellar disks are expected to form around Class 0 protostars; though the disk around L1157 is not yet resolved spatially by our CARMA observations. However, a close

examination combined with radiative transfer modeling constrains the circumstellar disk around L1157 to be smaller than ∼40 AU in radius and ∼4-25 M_{Jup} in mass. The mass estimate of the disk component highly depends on the model assumptions for the envelope. A flat envelope, such as the Terebey-Shu-Cassen model with a power-law index $p \sim 1.5$ in the outer region, requires a strong point source flux from the unresolved disk, while a steep envelope with $p \sim 2$ can fit the observations without an embedded disk.

Dust grain properties are investigated through the dual-wavelength observations of L1157. A dust opacity spectral index β of ∼0.9 is found for L1157, consistent with the values found for other Class 0 sources. The β value in Class 0 YSOs being significantly smaller than that in the interstellar medium ($\beta \sim 2$) implies that grain growth has already started in the Class 0 stage of protostellar evolution.

Future observations with higher resolution and sensitivity will resolve disk and envelope structures at small scales along with multiple molecular tracers revealing the kinematics and chemical conditions. Several survey projects are already underway. For example, Tobin et al. (2011) carry out a kinematics survey using both single-dish (IRAM) and interferometric (CARMA and SMA) data; the EVLA key science project *Disks@EVLA* led by C. Chandler aims to investigate the grain growth process in protoplanetary disks; the SMA project *DISCS* focuses on the chemical evolution in disks (Öberg et al., 2011). Furthermore, ALMA will be fully operational in the next few years with its unprecedented angular resolution and spatial coverage from far-infrared to millimeter wavelengths. One example that demonstrates ALMA's capability is shown by synthetic observations of an extremely young object in Chapter 4. For embedded YSOs, ALMA will be unambiguously resolve the earliest disks and unveil their characteristics, thus revealing the initial conditions of planet formation. In addition, ALMA is particularly sensitive to the transition zone between the disk and the envelope for nearby Class 0 YSOs, and will be able to break the model degeneracy between a disk component and inner envelope structure.

As we advance with observations of higher angular resolutions and sensitivities, our un-

derstanding of star formation process progresses from qualitative descriptions of the general scenario to quantitative constraints of the detailed models. Once both theories and observations of star formation are sufficiently developed, we will enter the era of precision star formation and determine protostellar evolution with high accuracy. This thesis focuses on dust emission from embedded protostars using interferometric data at millimeter wavelengths; other observational data such as near-infrared scattered light, extinction maps, and SEDs from optical to radio wavelengths all constrain the properties of these young objects. Future modeling, with consideration of all available data, will lead towards a more comprehensive understanding of star formation.

References

Adams, F. C. 1991, ApJ, 382, 544

Adams, F. C., Lada, C. J., & Shu, F. H. 1987, ApJ, 312, 788

Adams, F. C. & Shu, F. H. 1985, ApJ, 296, 655

Aikawa, Y., Herbst, E., Roberts, H., & Caselli, P. 2005, ApJ, 620, 330

Aikawa, Y., Ohashi, N., & Herbst, E. 2003, ApJ, 593, 906

Akaike, H. 1974, IEEE Transactions on Automatic Control, 19, 716

Andre, P., Ward-Thompson, D., & Barsony, M. 1993, ApJ, 406, 122

Andre, P., Ward-Thompson, D., & Barsony, M. 2000, in Protostars and Planets IV, ed. V. Mannings, A. Boss, & S. S. Russell, 59

Andrews, S. M., Wilner, D. J., Hughes, A. M., Qi, C., & Dullemond, C. P. 2009, ApJ, 700, 1502

Arce, H. G., Santiago-García, J., Jørgensen, J. K., Tafalla, M., & Bachiller, R. 2008, ApJ, 681, L21

Arce, H. G. & Sargent, A. I. 2006, ApJ, 646, 1070

Bachiller, R. 1996, ARA&A, 34, 111

Bachiller, R., Martin-Pintado, J., & Fuente, A. 1993, ApJ, 417, L45

Bachiller, R. & Perez Gutierrez, M. 1997, ApJ, 487, L93

Bachiller, R., Pérez Gutiérrez, M., Kumar, M. S. N., & Tafalla, M. 2001, A&A, 372, 899

Bally, J., Devine, D., & Reipurth, B. 1996, ApJ, 473, L49

Barranco, J. A. & Goodman, A. A. 1998, ApJ, 504, 207

Basu, S. 1998, ApJ, 509, 229

Basu, S. & Mouschovias, T. C. 1994, ApJ, 432, 720

Beckwith, S. V. W., Henning, T., & Nakagawa, Y. 2000, Protostars and Planets IV, 533

Beckwith, S. V. W. & Sargent, A. I. 1991, ApJ, 381, 250

Belloche, A. & André, P. 2004, A&A, 419, L35

Belloche, A., André, P., Despois, D., & Blinder, S. 2002, A&A, 393, 927

Belloche, A., Parise, B., van der Tak, F. F. S., Schilke, P., Leurini, S., Güsten, R., & Nyman, L.-Å. 2006, A&A, 454, L51

Beltrán, M. T., Gueth, F., Guilloteau, S., & Dutrey, A. 2004, A&A, 416, 631

Benson, P. J., Caselli, P., & Myers, P. C. 1998, ApJ, 506, 743

Benson, P. J. & Myers, P. C. 1989, ApJS, 71, 89

Bergin, E. A. & Langer, W. D. 1997, ApJ, 486, 316

Blake, G. A., Sandell, G., van Dishoeck, E. F., Groesbeck, T. D., Mundy, L. G., & Aspin, C. 1995, ApJ, 441, 689

Bock, D., Bolatto, A. D., Hawkins, D. W., Kemball, A. J., Lamb, J. W., Plambeck, R. L., Pound, M. W., Scott, S. L., Woody, D. P., & Wright, M. C. H. 2006, in Society of Photo-Optical Instrumentation Engineers (SPIE) Conference Series, Vol. 6267

Bodenheimer, P. 1995, ARA&A, 33, 199

Boss, A. P. & Yorke, H. W. 1995, ApJ, 439, L55

Brinch, C., Crapsi, A., Jørgensen, J. K., Hogerheijde, M. R., & Hill, T. 2007, A&A, 475, 915

Burkert, A. & Bodenheimer, P. 2000, ApJ, 543, 822

Burnham, K. P. & Anderson, D. R. 2002, Model Selection and Multimodel Inference: A Practical Information-Theoretic Approach, 2nd edn. (New York: Springer-Verlag)

Caselli, P., Benson, P. J., Myers, P. C., & Tafalla, M. 2002, ApJ, 572, 238

Caselli, P., Myers, P. C., & Thaddeus, P. 1995, ApJ, 455, L77

Cassen, P. & Moosman, A. 1981, Icarus, 48, 353

Cernis, K. 1990, Ap&SS, 166, 315

—. 1993, Baltic Astronomy, 2, 214

Chandler, C. J., Barsony, M., & Moore, T. J. T. 1998, MNRAS, 299, 789

Chandler, C. J., Koerner, D. W., Sargent, A. I., & Wood, D. O. S. 1995, ApJ, 449, L139

Chandler, C. J. & Richer, J. S. 2000, ApJ, 530, 851

Chen, H., Myers, P. C., Ladd, E. F., & Wood, D. O. S. 1995, ApJ, 445, 377

Chen, X., Arce, H. G., Zhang, Q., Bourke, T. L., Launhardt, R., Schmalzl, M., & Henning, T. 2010, ApJ, 715, 1344

Chen, X., Launhardt, R., Bourke, T. L., Henning, T., & Barnes, P. J. 2008, ApJ, 683, 862

Chen, X., Launhardt, R., & Henning, T. 2007, ApJ, 669, 1058

Chiang, H.-F., Looney, L. W., Tassis, K., Mundy, L. G., & Mouschovias, T. C. 2008, ApJ, 680, 474

Chiang, H.-F., Looney, L. W., Tobin, J. J., & Hartmann, L. 2010, ApJ, 709, 470

Choi, M. 2001, ApJ, 553, 219

—. 2002, ApJ, 575, 900

—. 2005, ApJ, 630, 976

Choi, M., Panis, J.-F., & Evans, II, N. J. 1999, ApJS, 122, 519

Crutcher, R. M., Wandelt, B., Heiles, C., Falgarone, E., & Troland, T. H. 2010, ApJ, 725, 466

Daniel, F., Cernicharo, J., & Dubernet, M.-L. 2006, ApJ, 648, 461

de Zeeuw, P. T., Hoogerwerf, R., de Bruijne, J. H. J., Brown, A. G. A., & Blaauw, A. 1999, AJ, 117, 354

Desch, S. J. & Mouschovias, T. Ch. 2001, ApJ, 550, 314

Di Francesco, J., Myers, P. C., Wilner, D. J., Ohashi, N., & Mardones, D. 2001, ApJ, 562, 770

Draine, B. T. 2006, ApJ, 636, 1114

Draine, B. T. & Lee, H. M. 1984, ApJ, 285, 89

Dullemond, C. P. & Dominik, C. 2004, A&A, 417, 159

Dunham, M. M., Chen, X., Arce, H. G., Bourke, T. L., Schnee, S., & Enoch, M. L. 2011, ArXiv e-prints

Dunham, M. M., Crapsi, A., Evans, II, N. J., Bourke, T. L., Huard, T. L., Myers, P. C., & Kauffmann, J. 2008, ApJS, 179, 249

Eisner, J. A., Hillenbrand, L. A., Carpenter, J. M., & Wolf, S. 2005, ApJ, 635, 396

Elmegreen, B. G. & Scalo, J. 2004, ARA&A, 42, 211

Emprechtinger, M., Caselli, P., Volgenau, N. H., Stutzki, J., & Wiedner, M. C. 2009, A&A, 493, 89

Enoch, M. L., Corder, S., Duchêne, G., Bock, D. C., Bolatto, A. D., Culverhouse, T. L., Kwon, W., Lamb, J. W., Leitch, E. M., Marrone, D. P., Muchovej, S. J., Pérez, L. M., Scott, S. L., Teuben, P. J., Wright, M. C. H., & Zauderer, B. A. 2011, ApJS, 195, 21

Enoch, M. L., Corder, S., Dunham, M. M., & Duchêne, G. 2009, ApJ, 707, 103

Enoch, M. L., Lee, J.-E., Harvey, P., Dunham, M. M., & Schnee, S. 2010, ApJ, 722, L33

Enoch, M. L., Young, K. E., Glenn, J., Evans, II, N. J., Golwala, S., Sargent, A. I., Harvey, P., Aguirre, J., Goldin, A., Haig, D., Huard, T. L., Lange, A., Laurent, G., Maloney, P., Mauskopf, P., Rossinot, P., & Sayers, J. 2006, ApJ, 638, 293

Evans, N. J., Dunham, M. M., Jørgensen, J. K., Enoch, M. L., Merín, B., van Dishoeck, E. F., Alcalá, J. M., Myers, P. C., Stapelfeldt, K. R., Huard, T. L., Allen, L. E., Harvey, P. M., van Kempen, T., Blake, G. A., Koerner, D. W., Mundy, L. G., Padgett, D. L., & Sargent, A. I. 2009, ApJS, 181, 321

Evans, II, N. J. 1999, ARA&A, 37, 311

Evans, II, N. J., Lee, J.-E., Rawlings, J. M. C., & Choi, M. 2005, ApJ, 626, 919

Evans, II, N. J., Rawlings, J. M. C., Shirley, Y. L., & Mundy, L. G. 2001, ApJ, 557, 193

Fiedler, R. A. & Mouschovias, T. Ch. 1993, ApJ, 415, 680

Ford, E. B. 2005, AJ, 129, 1706

Froebrich, D. 2005, ApJS, 156, 169

Galli, D. & Shu, F. H. 1993, ApJ, 417, 220

Gammie, C. F., Lin, Y.-T., Stone, J. M., & Ostriker, E. C. 2003, ApJ, 592, 203

Gelman, A., Carlin, J. B., S., S. H., & B., R. D. 2004, Bayesian data analysis, 2nd edn., Texts in statistical science (Boca Raton: Chapman & Hall/CRC)

Girart, J. M., Rao, R., & Marrone, D. P. 2006, Science, 313, 812

Goldsmith, P. F. & Langer, W. D. 1999, ApJ, 517, 209

Goldsmith, P. F., Langer, W. D., & Velusamy, T. 1999, ApJ, 519, L173

Gong, H. & Ostriker, E. C. 2009, ApJ, 699, 230

Goodman, A. A., Benson, P. J., Fuller, G. A., & Myers, P. C. 1993, ApJ, 406, 528

Greaves, J. S. & Rice, W. K. M. 2011, MNRAS, 412, L88

Green, S., Montgomery, Jr., J. A., & Thaddeus, P. 1974, ApJ, 193, L89

Gregersen, E. M., Evans, II, N. J., Zhou, S., & Choi, M. 1997, ApJ, 484, 256

Gueth, F., Bachiller, R., & Tafalla, M. 2003, A&A, 401, L5

Gueth, F., Guilloteau, S., & Bachiller, R. 1996, A&A, 307, 891

Gueth, F., Guilloteau, S., Dutrey, A., & Bachiller, R. 1997, A&A, 323, 943

Hartmann, L., Boss, A., Calvet, N., & Whitney, B. 1994, ApJ, 430, L49

Hartmann, L., Calvet, N., & Boss, A. 1996, ApJ, 464, 387

Harvey, D. W. A., Wilner, D. J., Myers, P. C., Tafalla, M., & Mardones, D. 2003, ApJ, 583, 809

Hennebelle, P. & Fromang, S. 2008, A&A, 477, 9

Hildebrand, R. H. 1983, QJRAS, 24, 267

Hunter, C. 1977, ApJ, 218, 834

Isella, A., Carpenter, J. M., & Sargent, A. I. 2010, ApJ, 714, 1746

Jørgensen, J. K., Bourke, T. L., Myers, P. C., Di Francesco, J., van Dishoeck, E. F., Lee, C.-F., Ohashi, N., Schöier, F. L., Takakuwa, S., Wilner, D. J., & Zhang, Q. 2007, ApJ, 659, 479

Jørgensen, J. K., Bourke, T. L., Myers, P. C., Schöier, F. L., van Dishoeck, E. F., & Wilner, D. J. 2005, ApJ, 632, 973

Jørgensen, J. K., Harvey, P. M., Evans, II, N. J., Huard, T. L., Allen, L. E., Porras, A., Blake, G. A., Bourke, T. L., Chapman, N., Cieza, L., Koerner, D. W., Lai, S.-P., Mundy, L. G., Myers, P. C., Padgett, D. L., Rebull, L., Sargent, A. I., Spiesman, W., Stapelfeldt, K. R., van Dishoeck, E. F., Wahhaj, Z., & Young, K. E. 2006, ApJ, 645, 1246

Jørgensen, J. K., Hogerheijde, M. R., van Dishoeck, E. F., Blake, G. A., & Schöier, F. L. 2004a, A&A, 413, 993

Jørgensen, J. K., Schöier, F. L., & van Dishoeck, E. F. 2004b, A&A, 416, 603

Jørgensen, J. K. & van Dishoeck, E. F. 2010, ApJ, 710, L72

Jørgensen, J. K., van Dishoeck, E. F., Visser, R., Bourke, T. L., Wilner, D. J., Lommen, D., Hogerheijde, M. R., & Myers, P. C. 2009, A&A, 507, 861

Kauffmann, J., Bertoldi, F., Evans, II, N. J., & the C2D Collaboration. 2005, Astronomische Nachrichten, 326, 878

Keene, J. & Masson, C. R. 1990, ApJ, 355, 635

Kirk, H., Johnstone, D., & Tafalla, M. 2007, ApJ, 668, 1042

Kirk, J. M., Ward-Thompson, D., Di Francesco, J., Bourke, T. L., Evans, N. J., Merín, B., Allen, L. E., Cieza, L. A., Dunham, M. M., Harvey, P., Huard, T., Jørgensen, J. K., Miller, J. F., Noriega-Crespo, A., Peterson, D., Ray, T. P., & Rebull, L. M. 2009, ApJS, 185, 198

Knee, L. B. G. & Sandell, G. 2000, A&A, 361, 671

Krügel, E. & Siebenmorgen, R. 1994, A&A, 288, 929

Kun, M. 1998, ApJS, 115, 59

Kun, M., Kiss, Z. T., & Balog, Z. 2008, Star Forming Regions in Cepheus (Astronomical Society of the Pacific, Edited by Bo Reipurth), 136

Kunz, M. W. & Mouschovias, T. C. 2009, ApJ, 693, 1895

—. 2010, MNRAS, 408, 322

Kwon, W., Looney, L. W., Crutcher, R. M., & Kirk, J. M. 2006, ApJ, 653, 1358

Kwon, W., Looney, L. W., & Mundy, L. G. 2011, ArXiv e-prints

Kwon, W., Looney, L. W., Mundy, L. G., Chiang, H.-F., & Kemball, A. J. 2009, ApJ, 696, 841

Lada, C. J. 1987, in IAU Symposium, Vol. 115, Star Forming Regions, ed. M. Peimbert & J. Jugaku, 1–17

Lada, C. J., Alves, J., & Lada, E. A. 1996, AJ, 111, 1964

Lada, C. J. & Wilking, B. A. 1984, ApJ, 287, 610

Larson, R. B. 1969, MNRAS, 145, 271

Lay, O. P., Carlstrom, J. E., & Hills, R. E. 1995, ApJ, 452, L73

Lee, C.-F., Ho, P. T. P., & White, S. M. 2005, ApJ, 619, 948

Lee, C. W., Myers, P. C., & Tafalla, M. 2001, ApJS, 136, 703

Lee, J.-E., Bergin, E. A., & Evans, II, N. J. 2004, ApJ, 617, 360

Li, A. & Draine, B. T. 2001, ApJ, 554, 778

Liddle, A. R. 2004, MNRAS, 351, L49

—. 2007, MNRAS, 377, L74

—. 2009, Annual Review of Nuclear and Particle Science, 59, 95

Loinard, L., Rodríguez, L. F., D'Alessio, P., Wilner, D. J., & Ho, P. T. P. 2002, ApJ, 581, L109

Looney, L. W., Mundy, L. G., & Welch, W. J. 2000, ApJ, 529, 477

—. 2003, ApJ, 592, 255

Looney, L. W., Tobin, J. J., & Kwon, W. 2007, ApJ, 670, L131

Loredo, T. J. 1990, in Maximum-Entropy and Bayesian Methods, ed. P. Fougere (Dordrecht: Kluwer Academic Publishers), 81–142

Loredo, T. J. 1992, in Statistical Challenges in Modern Astronomy, ed. E. D. Feigelson & G. J. Babu, 275–306

Mac Low, M.-M. & Klessen, R. S. 2004, Reviews of Modern Physics, 76, 125

Mardones, D., Myers, P. C., Tafalla, M., Wilner, D. J., Bachiller, R., & Garay, G. 1997, ApJ, 489, 719

Maret, S., Bergin, E. A., & Lada, C. J. 2006, Nature, 442, 425

—. 2007, ApJ, 670, L25

Masunaga, H. & Inutsuka, S.-i. 2000a, ApJ, 531, 350

—. 2000b, ApJ, 536, 406

Mathis, J. S., Rumpl, W., & Nordsieck, K. H. 1977, ApJ, 217, 425

Maury, A. J., André, P., Hennebelle, P., Motte, F., Stamatellos, D., Bate, M., Belloche, A., Duchêne, G., & Whitworth, A. 2010, A&A, 512, A40

McKee, C. F. & Ostriker, E. C. 2007, ARA&A, 45, 565

Meehan, L. S. G., Wilking, B. A., Claussen, M. J., Mundy, L. G., & Wootten, A. 1998, AJ, 115, 1599

Miao, Y., Mehringer, D. M., Kuan, Y.-J., & Snyder, L. E. 1995, ApJ, 445, L59

Miyake, K. & Nakagawa, Y. 1993, Icarus, 106, 20

Momose, M., Ohashi, N., Kawabe, R., Nakano, T., & Hayashi, M. 1998, ApJ, 504, 314

Moreno, R. & Guilloteau, S. 2002, An Amplitude Calibration Strategy for ALMA, ALMA Memo 372, ALMA

Mouschovias, T. Ch. 1996, in The Role of Dust in the Formation of Stars, ed. H. U. Käufl & R. Siebenmorgen (Berlin: Springer-Verlag), 382

Mouschovias, T. Ch. & Ciolek, G. E. 1999, in The Origin of Stars and Planetary Systems, ed. C. J. Lada & N. D. Kylafis (Dordrecht: Kluwer Academic Publishers), 305

Mundy, L. G., Looney, L. W., Erickson, W., Grossman, A., Welch, W. J., Forster, J. R., Wright, M. C. H., Plambeck, R. L., Lugten, J., & Thornton, D. D. 1996, ApJ, 464, L169

Myers, P. C., Adams, F. C., Chen, H., & Schaff, E. 1998, ApJ, 492, 703

Myers, P. C., Fuller, G. A., Goodman, A. A., & Benson, P. J. 1991, ApJ, 376, 561

Myers, P. C., Mardones, D., Tafalla, M., Williams, J. P., & Wilner, D. J. 1996, ApJ, 465, L133

Natta, A., Testi, L., Calvet, N., Henning, T., Waters, R., & Wilner, D. 2007, in Protostars and Planets V, ed. B. Reipurth, D. Jewitt, & K. Keil, 767–781

Natta, A., Testi, L., Neri, R., Shepherd, D. S., & Wilner, D. J. 2004, A&A, 416, 179

Nisini, B., Benedettini, M., Codella, C., Giannini, T., Liseau, R., Neufeld, D., Tafalla, M., van Dishoeck, E. F., Bachiller, R., Baudry, A., Benz, A. O., Bergin, E., Bjerkeli, P., Blake, G., Bontemps, S., Braine, J., Bruderer, S., Caselli, P., Cernicharo, J., Daniel, F., Encrenaz, P., di Giorgio, A. M., Dominik, C., Doty, S., Fich, M., Fuente, A., Goicoechea, J. R., de Graauw, T., Helmich, F., Herczeg, G., Herpin, F., Hogerheijde, M., Jacq, T., Johnstone, D., Jørgensen, J., Kaufman, M., Kristensen, L., Larsson, B., Lis, D., Marseille, M., McCoey, C., Melnick, G., Olberg, M., Parise, B., Pearson, J., Plume, R., Risacher, C., Santiago, J., Saraceno, P., Shipman, R., van Kempen, T. A., Visser, R., Viti, S., Wampfler, S., Wyrowski, F., van der Tak, F., Yıldız, U. A., Delforge, B., Desbat, J., Hatch, W. A., Péron, I., Schieder, R., Stern, J. A., Teyssier, D., & Whyborn, N. 2010, A&A, 518, L120

Öberg, K. I., Qi, C., Fogel, J. K. J., Bergin, E. A., Andrews, S. M., Espaillat, C., Wilner, D. J., Pascucci, I., & Kastner, J. H. 2011, ApJ, 734, 98

Öberg, K. I., van Broekhuizen, F., Fraser, H. J., Bisschop, S. E., van Dishoeck, E. F., & Schlemmer, S. 2005, ApJ, 621, L33

Offner, S. S. R. & Krumholz, M. R. 2009, ApJ, 693, 914

Ohashi, N., Hayashi, M., Ho, P. T. P., & Momose, M. 1997a, ApJ, 475, 211

Ohashi, N., Hayashi, M., Ho, P. T. P., Momose, M., Tamura, M., Hirano, N., & Sargent, A. I. 1997b, ApJ, 488, 317

O'Linger, J. C., Cole, D. M., Ressler, M. E., & Wolf-Chase, G. 2006, AJ, 131, 2601

Ossenkopf, V. & Henning, T. 1994, A&A, 291, 943

Penston, M. V. 1969, MNRAS, 144, 425

Pérez, L. M., Lamb, J. W., Woody, D. P., Carpenter, J. M., Zauderer, B. A., Isella, A., Bock, D. C., Bolatto, A. D., Carlstrom, J., Culverhouse, T. L., Joy, M., Kwon, W., Leitch, E. M., Marrone, D. P., Muchovej, S. J., Plambeck, R. L., Scott, S. L., Teuben, P. J., & Wright, M. C. H. 2010, ApJ, 724, 493

Pickett, H. M., Poynter, I. R. L., Cohen, E. A., Delitsky, M. L., Pearson, J. C., & Muller, H. S. P. 1998, Journal of Quantitative Spectroscopy and Radiative Transfer, 60, 883

Pineda, J. E., Arce, H. G., Schnee, S., Goodman, A. A., Bourke, T., Foster, J. B., Robitaille, T., Tanner, J., Kauffmann, J., Tafalla, M., Caselli, P., & Anglada, G. 2011, ArXiv e-prints

Pudritz, R. E., Ouyed, R., Fendt, C., & Brandenburg, A. 2007, in Protostars and Planets V, ed. B. Reipurth, D. Jewitt, & K. Keil, 277–294

Rauch, K. P. 2011, Revised CARMA Correlator FPGA Configurations, CARMA Memorandum 46, CARMA

Reipurth, B. & Aspin, C. 2010, in Evolution of Cosmic Objects through their Physical Activity, ed. H. A. Harutyunian, A. M. Mickaelian, & Y. Terzian, 19–38

Ricci, L., Testi, L., Natta, A., & Brooks, K. J. 2010a, A&A, 521, A66

Ricci, L., Testi, L., Natta, A., Neri, R., Cabrit, S., & Herczeg, G. J. 2010b, A&A, 512, A15

Robitaille, T. P., Whitney, B. A., Indebetouw, R., & Wood, K. 2007, ApJS, 169, 328

Robitaille, T. P., Whitney, B. A., Indebetouw, R., Wood, K., & Denzmore, P. 2006, ApJS, 167, 256

Rodmann, J., Henning, T., Chandler, C. J., Mundy, L. G., & Wilner, D. J. 2006, A&A, 446, 211

Saigo, K., Tomisaka, K., & Matsumoto, T. 2008, ApJ, 674, 997

Sandell, G. & Knee, L. B. G. 2001, ApJ, 546, L49

Sault, R. J., Teuben, P. J., & Wright, M. C. H. 1995, in Astronomical Society of the Pacific Conference Series, Vol. 77, Astronomical Data Analysis Software and Systems IV, ed. R. A. Shaw, H. E. Payne, & J. J. E. Hayes, 433

Schnee, S., Enoch, M., Noriega-Crespo, A., Sayers, J., Terebey, S., Caselli, P., Foster, J., Goodman, A., Kauffmann, J., Padgett, D., Rebull, L., Sargent, A., & Shetty, R. 2010, ApJ, 708, 127

Schwarz, G. 1978, ANNALS OF STATISTICS, 6, 461

Seale, J. P. & Looney, L. W. 2008, ApJ, 675, 427

Shang, H., Li, Z.-Y., & Hirano, N. 2007, in Protostars and Planets V, ed. B. Reipurth, D. Jewitt, & K. Keil, 261–276

Shirley, Y. L., Evans, II, N. J., Rawlings, J. M. C., & Gregersen, E. M. 2000, ApJS, 131, 249

Shirley, Y. L., Huard, T. L., Pontoppidan, K. M., Wilner, D. J., Stutz, A. M., Bieging, J. H., & Evans, II, N. J. 2011a, ApJ, 728, 143

Shirley, Y. L., Mason, B. S., Mangum, J. G., Bolin, D. E., Devlin, M. J., Dicker, S. R., & Korngut, P. M. 2011b, AJ, 141, 39

Shirley, Y. L., Nordhaus, M. K., Grcevich, J. M., Evans, II, N. J., Rawlings, J. M. C., & Tatematsu, K. 2005, ApJ, 632, 982

Shu, F. H. 1977, ApJ, 214, 488

Spergel, D. N., Bean, R., Doré, O., Nolta, M. R., Bennett, C. L., Dunkley, J., Hinshaw, G., Jarosik, N., Komatsu, E., Page, L., Peiris, H. V., Verde, L., Halpern, M., Hill, R. S., Kogut, A., Limon, M., Meyer, S. S., Odegard, N., Tucker, G. S., Weiland, J. L., Wollack, E., & Wright, E. L. 2007, ApJS, 170, 377

Stahler, S. W. & Palla, F. 2005, The Formation of Stars (Weinheim: Wiley-VCH)

Straizys, V., Cernis, K., Kazlauskas, A., & Meistas, E. 1992, Baltic Astronomy, 1, 149

Tafalla, M., Myers, P. C., Caselli, P., Walmsley, C. M., & Comito, C. 2002, ApJ, 569, 815

Tassis, K. 2007, MNRAS, 379, L50

Tassis, K. & Mouschovias, T. Ch. 2005a, ApJ, 618, 769

—. 2005b, ApJ, 618, 783

—. 2007a, ApJ, 660, 370

—. 2007b, ApJ, 660, 388

—. 2007c, ApJ, 660, 402

Terebey, S., Chandler, C. J., & Andre, P. 1993, ApJ, 414, 759

Terebey, S., Shu, F. H., & Cassen, P. 1984, ApJ, 286, 529

Thaddeus, P. & Turner, B. E. 1975, ApJ, 201, L25

Tobin, J. J., Hartmann, L., Chiang, H.-F., Looney, L. W., Bergin, E. A., Chandler, C. J., Masque, J. M., Maret, S., & Heitsch, F. 2011, ArXiv e-prints

Tobin, J. J., Hartmann, L., & Loinard, L. 2010a, ApJ, 722, L12

Tobin, J. J., Hartmann, L., Looney, L. W., & Chiang, H.-F. 2010b, ApJ, 712, 1010

Tobin, J. J., Looney, L. W., Mundy, L. G., Kwon, W., & Hamidouche, M. 2007, ApJ, 659, 1404

Tsamis, Y. G., Rawlings, J. M. C., Yates, J. A., & Viti, S. 2008, MNRAS, 388, 898

Turner, B. E. 1974, ApJ, 193, L83

Ulrich, R. K. 1976, ApJ, 210, 377

van der Tak, F. F. S., van Dishoeck, E. F., Evans, II, N. J., Bakker, E. J., & Blake, G. A. 1999, ApJ, 522, 991

Velusamy, T., Langer, W. D., & Goldsmith, P. F. 2002, ApJ, 565, L43

Vicente, S. M. & Alves, J. 2005, A&A, 441, 195

Vorobyov, E. I. & Basu, S. 2005a, MNRAS, 360, 675

—. 2005b, ApJ, 633, L137

Ward-Thompson, D. & Buckley, H. D. 2001, MNRAS, 327, 955

Ward-Thompson, D., Kirk, J. M., Greaves, J. S., & André, P. 2011, MNRAS, 415, 2812

Watson, D. M., Bohac, C. J., Hull, C., Forrest, W. J., Furlan, E., Najita, J., Calvet, N., D'Alessio, P., Hartmann, L., Sargent, B., Green, J. D., Kim, K. H., & Houck, J. R. 2007, Nature, 448, 1026

Weingartner, J. C. & Draine, B. T. 2001, ApJ, 548, 296

Whitworth, A. & Summers, D. 1985, MNRAS, 214, 1

Wilking, B. A., Meyer, M. R., Greene, T. P., Mikhail, A., & Carlson, G. 2004, AJ, 127, 1131

Williams, J. P. & Cieza, L. A. 2011, ArXiv e-prints

Wilner, D. J., Myers, P. C., Mardones, D., & Tafalla, M. 2000, ApJ, 544, L69

Wilner, D. J. & Welch, W. J. 1994, ApJ, 427, 898

Wiseman, J., Wootten, A., Zinnecker, H., & McCaughrean, M. 2001, ApJ, 550, L87

Wolf-Chase, G. A., Barsony, M., & O'Linger, J. 2000, AJ, 120, 1467

Wolfire, M. G. & Cassinelli, J. P. 1986, ApJ, 310, 207

Womack, M., Ziurys, L. M., & Wyckoff, S. 1992, ApJ, 393, 188

Zhou, S. 1992, ApJ, 394, 204

Zhou, S., Evans, II, N. J., Koempe, C., & Walmsley, C. M. 1993, ApJ, 404, 232

Zhu, Z., Hartmann, L., Gammie, C., & McKinney, J. C. 2009, ApJ, 701, 620